Design of Metallic Nanostructures for Wavelength and Angle Selective Light Management

by

Brian J. Roberts

A dissertation submitted in partial fulfillment
of the requirements for the degree of
Doctor of Philosophy
(Electrical Engineering)
in the University of Michigan
2015

Doctoral Committee:

Associate Professor Pei-Cheng Ku, Chair
Professor Jaime D. Phillips
Associate Professor Max Shtein
Associate Professor Zhaohui Zhong

ACKNOWLEDGEMENTS

The author would like to thank the following people and organizations that made this work possible:

- Ph.D. thesis committee members Professor P.C. Ku, Professor Jaime Phillips, Professor Max Shtein, and Professor Zhaohui Zhong.
- Current and former members of Professor Ku's Nanophotonics and Nanofabrication Group, especially Dr. Nanditha Dissanayake, Qi Chen, and Michael Boyd who contributed directly to this project.
- The facilities and staff of the Lurie Nanofabrication Facility at the University of Michigan.
- The U.S. Department of Energy Center for Solar and Thermal Energy Conversion (CSTEC) at the University of Michigan and the National Science Foundation / Air Force Office of Scientific Research Emerging Frontiers in Research and Innovation (EFRI) program for funding support.

TABLE OF CONTENTS

LIST OF FIGURES

LIST OF TABLES

LIST OF APPENDICES

LIST OF ACRONYMS, ABBREVIATIONS, AND SYMBOLS

AFM - atomic force microscopy

AM1.5 - air mass 1.5 solar reference spectrum

DBR - distributed Bragg reflector

eV - electron volt

EQE - external quantum efficiency

FDTD - finite-difference time-domain

ICP - inductively coupled plasma

IR - infrared

ITO - indium tin oxide

LSP - localized surface plasmon

MEEP - MIT Electromagnetic Equation Propagation software

MEMS - micro electro-mechanical systems

PDMS - polydimethylsiloxane

PET - polyethylene terephthalate

P3HT:PCBM - poly-3-helythiophene : phenyl-C61-butyric acid methyl ester

PECVD - plasma enhanced chemical vapor deposition

PML - perfectly matched layer

PV - photovoltaic

RF - radio frequency

RGB - red / green / blue

RIE - reactive ion etching

sccm - standard cubic centimeters per minute

SEM - scanning electron microscope

TE - transverse electric

TM - transverse magnetic

UV - ultraviolet

a - radius or semi-axis

A - aspect ratio

C_{abs} - absorption cross section

C_{ext} - extinction cross section

C_{sca} - scattering cross section

e - ellipticity or free electron

$\vec{E}$ - electric field

f - oscillator strength or a function

$\vec{H}$ - magnetic field

I - current or optical intensity

J - current density

k - wavevector magnitude

L - geometrical polarization correction

n - refractive index

$\hat{n}$ - unit normal vector

P - power

Q - joule heating power density

R - ideal gas constant

$\vec{S}$ - Poynting vector

T - temperature

V - volume or voltage

x - size parameter or cartesian axis 1

y - cartesian axis 2

z - cartesian axis 3

α - polarizability or absorption coefficient

Γ - damping coefficient

ε - relative dielectric constant

ε' - real part of ε

ε'' - imaginary part of ε

θ - angle

λ - wavelength

μ^o - chemical potential

ω - radial frequency

ω_p - plasma frequency

CHAPTER I

Introduction

The modern technological landscape features numerous recent advances in optical and optoelectronic devices, from light emitting diodes to display screens to solar panels. Simultaneously, advances in nanotechnology have enabled shrinking such devices and exploring new physics at the nanoscale. The field of nano-optics, broadly defined as the interactions of light and matter at scales smaller than the optical wavelength, offers the potential to realize new and disruptive technologies for improved optoelectronics.

In this work we will explore and discuss the possibilities and potential for nano-optical systems to realize selective management of light based on its wavelength and incident angle, proposing new ideas for realizing 'smart' photovoltaics and window layers.

Motivation

The primary motivation for this work is the research area of thin film photovoltaics. For solar energy systems to compete with fossil fuels on a broad scale, costs must be reduced while energy conversion efficiencies are improved. Thin film photovoltaics (PVs), including such materials as organic polymers and amorphous silicon, can provide significantly reduced manufacturing and material costs[1-8]. However, such thin film systems have intrinsically poor charge transport properties as compared to crystalline semiconductors, limiting the absorbing layer thicknesses to a few hundred nanometers or less. Limited absorber thickness results in

optically thin cells which are not capable of harvesting all the incident sunlight, limiting the power conversion efficiency[1-10]. Next generation thin film PVs must pair the advantages of low cost with aggressive light management for increasing optical absorption. The requirement for light management within the subwavelength thickness of the absorbing region motivates the investigation of subwavelength nanostructures.

Metal structures are of particular interest for light management. In a conventional PV architecture, metal back contacts are used to reflect light back into a PV junction. In the subwavelength regime, metal nanostructures demonstrate additional optical effects due to the localized surface plasmon (LSP) resonance, arising from a resonant coupling between the oscillation of the optical frequency electric field and motion of the electron cloud within the metal[11-14], analogous to the motion of electrons in an antenna driven by an applied radio frequency field. Plasmonic particles have been exploited in many studies for improving absorption in thin film PVs[15-27], as they demonstrate resonant enhancement of near field optical intensity, and resonant enhancement of optical absorption and scattering cross sections[11-15]. In this work, we have sought to evaluate and clarify the effectiveness of plasmonic metal nanoparticles in improving photovoltaics, and to determine new ways in which metal (and non-metallic) nanostructures can be harnessed for advanced functionality in thin film PV systems.

Additionally, we recognize that the incomplete absorption of thin film PVs is not necessarily a disadvantage: semitransparent PV systems are of interest for widespread integration with building windows [28-35]. Or, thin layers absorbing only a fraction of the spectrum are of interest for multi-junction tandem cells, in which different layers target different portions of the spectrum[36-38]. The tunable resonant nature of LSP interactions offers the potential for improving

absorption in these systems as well, and for realizing new functionality such as angular selectivity[39-42].

Upon establishing methods for angle selective control of light in photovoltaic systems, we also consider the application of these ideas to enabling other thin film optical systems such as window layers with tunable visible transmission[43-47]. Finally, non-metallic nanostructures that are able to realize angle selective control of light are also of interest.

Localized Surface Plasmon Resonance

We begin with background information on one of the canonical problems in nano-optics, calculation of the localized surface plasmon resonance of a metal nanoparticle, as much of the following material benefits from an intuitive grasp of the physics at work.

Consider a sphere of radius a with dielectric constant $\varepsilon = \varepsilon' + i\varepsilon''$ illuminated by an incident plane wave. For a nanosphere sufficiently smaller than the wavelength of light ($a <<$ wavelength λ), the outside electric field is approximately constant, and the resulting electric field can be calculated analytically by electrostatics[48]. The solution is a constant field inside the sphere and a superposition of the incident field plus a dipole outside, as plotted in Figure 1.1(a). The corresponding electromagnetic energy density / optical intensity (proportional to the square of the electric field) is plotted in Figure 1.1(b).

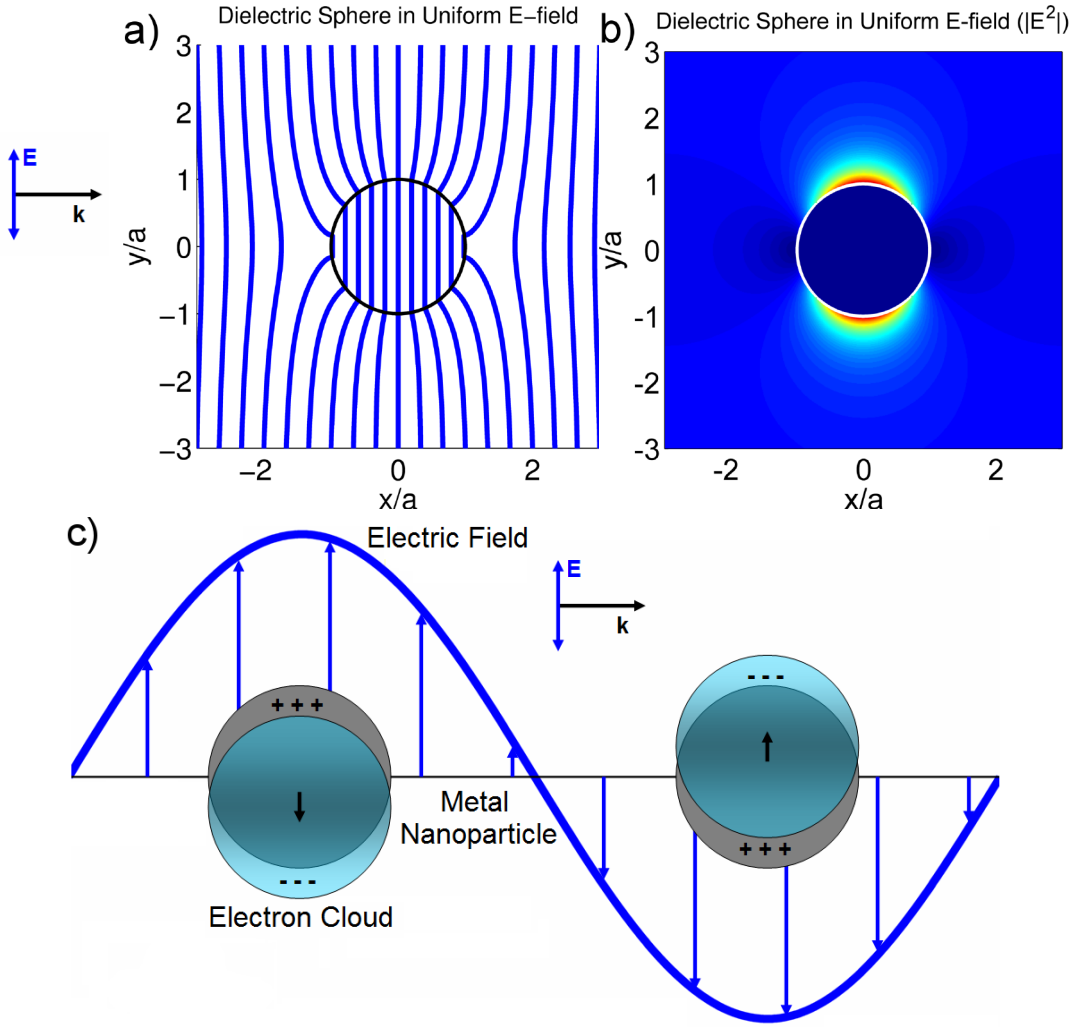

Figure 1.1 - (a) Electric field profile for a sphere of radius a in a uniform external field in the x direction. (b) Near field optical intensity, proportional to $\left|\vec{E}^2\right|$. (c) Motion of charges within metal nanoparticles driven by applied electromagnetic wave.

The magnitude of the dipole term is characterized by the sphere's polarizability α accoring to[11, 12]:

$$\alpha = 4\pi a^3 \frac{\varepsilon - \varepsilon_m}{\varepsilon + 2\varepsilon_m} \qquad 1.1$$

where ε_m is the dielectric constant of the surrounding material. Physically, this dipole polarizability corresponds to the incident field driving a separation of positive and negative charges within the particle with total dipole moment proportional to the number of mobile

charges / the nanoparticle volume and including terms relating the dielectric constants of the two media to satisfy electromagnetic boundary conditions. Transitioning from the electrostatic approximation back to a time-varying field, the polarization becomes an oscillation of charges within the particle (Figure 1.1(c)), and the dipole perturbation outside the nanoparticle corresponds to a re-radiated optical field.

When the dielectric constant ε has a negative real part, as is the case for a metal at optical frequencies[49-51], the polarizability α becomes resonant. This is the localized surface plasmon (LSP) resonance of the metal nanoparticle. At the resonance condition $\mathrm{Re}[\varepsilon(\omega)] = -2\varepsilon_m$ (where ε is now assumed to vary with radial electromagnetic frequency ω), interaction of the incident field and the particle is at its strongest, resulting in enhancement of the electromagnetic fields both inside the particle (resulting in increased optical absorption by the metal) and outside (resulting in increased optical intensity near the particle surface and increased light scattering)[11-15].

The resonant absorption and scattering of metal nanospheres can be summarized by defining frequency dependant absorption and scattering cross sections C_{abs} and C_{sca}[11]:

$$C_{abs} = k\,\mathrm{Im}(\alpha) = 4\pi k a^3\,\mathrm{Im}\left(\frac{\varepsilon - \varepsilon_m}{\varepsilon + 2\varepsilon_m}\right) \qquad 1.2$$

$$C_{sca} = \frac{k^4}{6\pi}|\alpha|^2 = \frac{8\pi}{3}k^4 a^6\left|\frac{\varepsilon - \varepsilon_m}{\varepsilon + 2\varepsilon_m}\right|^2 \qquad 1.3$$

where k is the electromagnetic wavevector magnitude $k = 2\pi/\lambda$. These cross sections have units of area (m^2), and can be thought of intuitively as the effective size the particle presents to the incident wave - on resonance, metal particles will absorb and scatter light as if they are significantly larger than their physical cross section. As the two expressions scale differently

with particle size a, we note that small particles will tend to favor absorption (scales with a^3) while larger particles will tend to favor scattering (scales with a^6).

It is also useful to define the nanoparticle extinction cross section C_{ext}:

$$C_{ext} = C_{abs} + C_{sca} \tag{1.4}$$

as the effective cross section of the metal nanoparticle in disrupting the incident wave[11].

Analytical Calculation and Tuning of Plasmon Resonances

Much of the engineering of the optical properties of metal nanoparticles comes down to tuning the LSP resonance to frequencies of interest. As seen in the equations above, the LSP resonant condition for a metal nanosphere depends primarily on its dielectric constant ε and that of the surrounding region ε_m, determined by the choice of metal and surrounding material. As a basic demonstration of important properties of LSP resonances, calculations are carried out here using three common choices of plasmonic metals: silver, gold, and aluminum[52, 53].

A variety of sources for the optical constants of metals are available in the literature[49-51]. In this work (and for ease of numerical simulation in subsequent chapters), we choose to model the metals of interest using tabulated fittings of ε by the Lorentz-Drude model[51]. The dielectric constant is given by a sum of terms for intraband free-electron motion in the metal (Drude model) plus a series of oscillator terms describing interband transitions (similar to the Lorentz model[54, 55] for transitions in insulators)[51]:

$$\varepsilon = 1 - \frac{f_0 {\omega_p}^2}{\omega(\omega + i\Gamma_0)} + \sum_{j=1}^{n} \frac{f_j {\omega_p}^2}{({\omega_j}^2 - \omega^2) - i\omega\Gamma_j} \tag{1.5}$$

where ω_p is the plasma frequency in the metal, ω_j are interband transition frequencies, f values are oscillator strengths and Γ values are damping coefficients. Note the sign on ε" (imaginary

part) can be flipped depending on choice of conventions. Values for the three metals of interest are reproduced below in Table 1.1 with frequencies reported in eV[51].

	Ag	Au	Al		Ag	Au	Al
ω_p	9.01	9.03	14.98	f_3	.011	.071	.166
f_0	.845	.760	.523	Γ_3	.065	.870	1.351
Γ_0	.048	.053	.047	ω_3	8.185	2.969	.601
f_1	.065	.024	.227	f_4	.840	.601	.030
Γ_1	3.886	.241	.333	Γ_4	.916	2.494	3.382
ω_1	.816	.415	.162	ω_4	9.083	4.304	3.473
f_2	.124	.010	.050	f_5	5.646	4.305	-
Γ_2	.452	.345	.312	Γ_5	2.419	2.214	-
ω_2	4.481	.830	1.544	ω_5	20.29	13.32	-

Table 1.1 - Lorentz-Drude model parameters for silver, gold, and aluminum

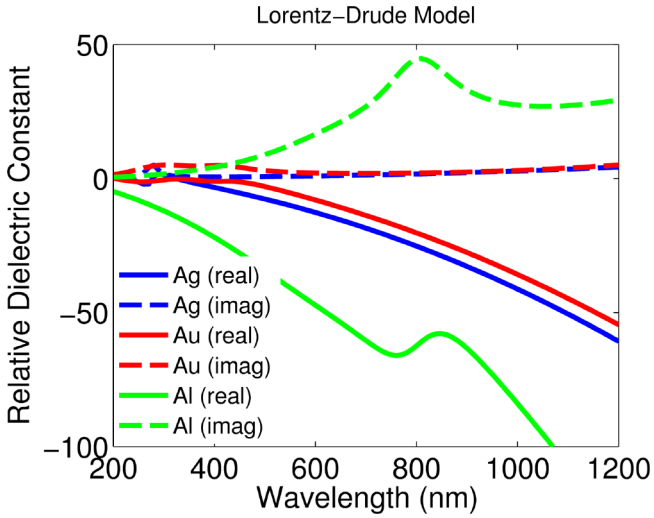

Figure 1.2 - Real and imaginary dielectric constant values for silver, gold, and aluminum.

The resulting real and imaginary ε values for these metals at the visible and near-visible wavelengths are plotted in Figure 1.2. As expected, all three metals have negative real dielectric constant in the visible region, allowing LSP resonance. Calculated values of cross sections C_{abs} and C_{sca} for each of the three metals are shown below for surrounding material of refractive index n = 1, 2, and 3.

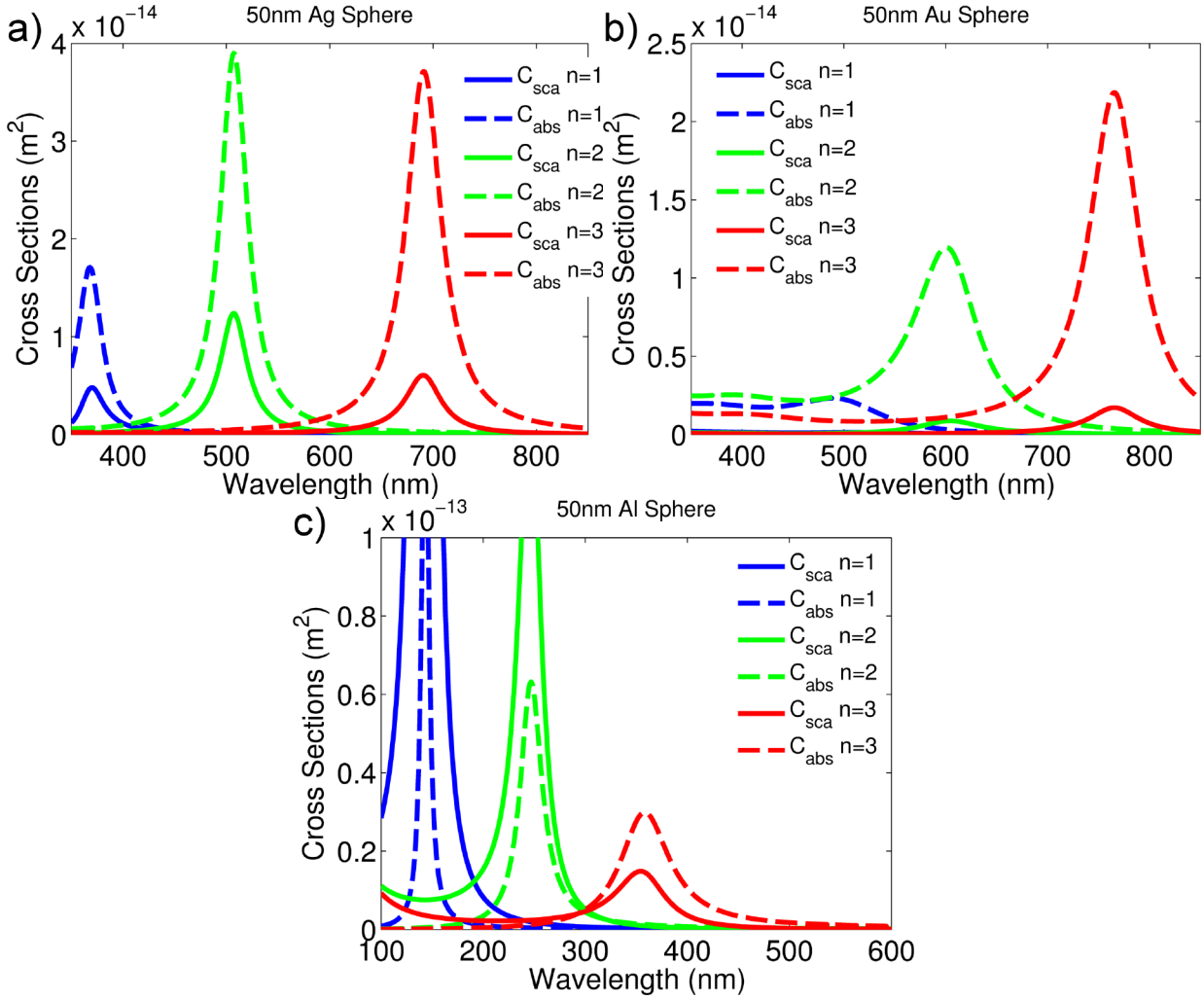

Figure 1.3 - Absorption (dashed) and scattering (solid) cross sections for 50 nm diameter (a) silver, (b) gold, and (c) aluminum spheres surrounded by material of refractive index n = 1 (blue), 2 (green), and 3 (red). Note the wavelength scaling change for aluminum.

Each metal has a different LSP resonance frequency, with aluminum at the shortest wavelength (in the UV range, due to its significantly higher plasma frequency) and gold at the longest (visible to near IR). Each resonance can also be redshifted by increasing the refractive index / dielectric constant of the surrounding medium, allowing tuning. Additionally, it can be seen that gold most favors absorption over scattering, while aluminum favors scattering, particularly for lower index surroundings. Each of the resonant peaks above demonstrate

extinction cross sections significantly larger than the nanoparticle geometrical cross section π(25 nm)^2 = 1.96×10^{-15} m^2.

Particle size also be used to modify LSP resonance properties[11]. Equation 1.1 is strictly only valid for the quasi-static case of $a << \lambda$, as explained above. As nanoparticle size increases, the incident wave across the sphere is no longer well described by a constant - dephasing across the particle tends to affect the polarizability. Mie theory[12, 56, 57] describes higher order electrodynamic corrections to the polarizability of a sphere. Without going into too much detail here, it is nonetheless informative to use a second order polarizability expression to build on the results above[11]:

$$\alpha = \frac{1-\left(\frac{1}{10}\right)(\varepsilon+\varepsilon_m)x^2}{\left(\frac{1}{3}+\frac{\varepsilon}{\varepsilon-\varepsilon_m}\right)-\frac{1}{30}(\varepsilon+10\varepsilon_m)x^2-i\frac{4\pi^2\varepsilon_m{}^{3/2}V}{3\lambda^3}} \tag{1.6}$$

where x is the 'size parameter' $x = \pi a / \lambda$ and V is the sphere's volume.

Absorption and scattering cross sections for 25, 50, and 100 nm diameter silver nanospheres with surrounding index n = 1.5 are calculated and plotted below using the second order expression of Equation 1.6.

As nanoparticle size increases, dephasing corrections result in a redshift and broadening of the LSP resonance. Total magnitude of the extinction coefficient also changes with size, proportional to the increase in geometrical size. From these results, we expect the quasi-static approximation of Equation 1.1 to remain valid for particle in the 10's of nm range (sizes < 50 nm), beyond which additional redshifts and corrections should be modeled by numerical simulation.

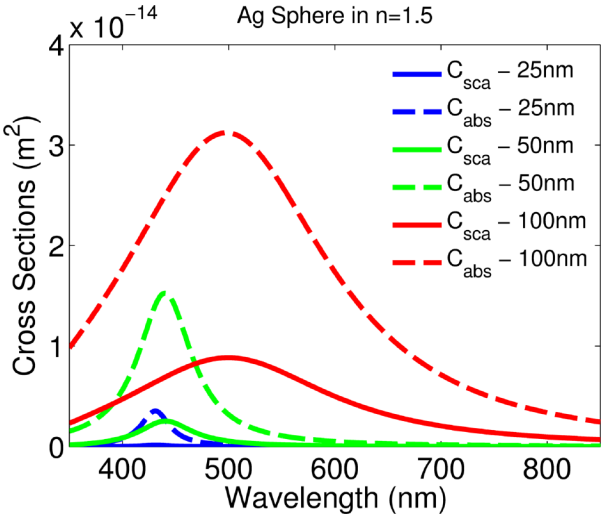

Figure 1.4 - Absorption (dashed) and scattering (solid) cross sections for silver nanospheres of 25 (blue), 50 (green) and 100 nm (red) diameter surrounded by index $n = 1.5$.

Finally, LSP resonances can be tuned by nanoparticle shape[11], though closed form analytical solutions for α only exist for certain geometries. We will defer discussion of this aspect of plasmonics until Chapter 4.

CHAPTER II

Metal Nanoparticles and Photovoltaic Materials: Understanding Absorption

While the analytical expressions for absorption and scattering discussed in Chapter 1 are useful in some circumstances, numerical simulations are required to account for complex geometries, interactions between neighboring particles, and the presence of absorbing films[15, 17, 18]. While a number of programs and methods exist for solving Maxwell's electromagnetic equations numerically, it is worth considering how this data is analyzed to extract important performance metrics and understand the system under consideration.

One of two main numerical analysis strategies is typically undertaken for analyzing the optical properties of a PV cell with plasmonic nanostructures. The first is to use finite element methods or other single frequency simulations to solve for the steady-state optical mode in a PV cell[18, 20-22]. This method has the disadvantage of only treating one wavelength of input light at a time, requiring many simulations to determine broad spectrum properties (though other advantages of the finite element approach will be discussed and used later in this thesis). Additionally, it can be conceptually difficult to justify the calculation of optical absorption: from a plot of the light that is present, one must determine the properties of light that is absent. The second simulation strategy is to compare the amount of power reflected from and transmitted through a nanoparticle-containing region by integrating the Poynting vector over some region far from the metal[17, 23, 24]. Such simulations can generate broad spectrum results by Fourier transform methods, though the results lack the granularity to clearly distinguish between

different optical processes at work. For example, such a simulation cannot distinguish between metal particle absorption and PV film absorption if the two materials are closely intertwined[17].

In this section, we present a refined numerical analysis method based on the finite-difference time-domain (FDTD) method[58]. Our method directly determines broad spectrum absorption properties from a single simulation, considers all of the optical processes that occur within a PV cell from first principles, and can be applied to analyze arbitrary nanostructure geometries and materials[59]. Additionally, we demonstrate that the near and far field properties of metal particles that determine absorption enhancement can be decoupled, helping us gain physical insight into the optical physics at work.

Numerical Analysis Methods

To quantify the absorption within an arbitrarily shaped region, this analysis focuses on its surface. The amount of optical power that is absorbed and converted to photocurrent can be found by comparing the optical power entering and exiting the surfaces of the PV region throughout the course of the simulation. The power entering (and then not exiting) the closed surface of an absorbing metal nanostructure provides a measurement of the optical energy lost to metallic dissipation. Some previous simulation methods[22] determine absorption by a differential approach, calculating the divergence of the steady state Poynting vector $\vec{E} \times \vec{H}$ at each point in the bulk of the simulation region. Or, studies evaluate the degree of light trapping by summing the steady state optical intensity at each point[18, 23, 24]. Our focus on surfaces represents an alternative integral approach. Using only surface points significantly decreases analysis time, and allows a straightforward method for determining broad spectrum behavior from a single simulation by a Fourier transform.

Simulations are carried out in 3-dimensions using an open source FDTD package called MEEP[60]. In the simplest case, we assume that metal structures are placed periodically in the cell, and simulate a single rectangular period of the active region like the one shown in Figure 2.1(a). Boundary conditions are periodic in the *x* and *y* directions, and absorbing 'perfectly matched layers' (PML)[60] provide boundaries on the *z* direction. Optical properties of simulated materials in the region are set using a complex dielectric constant $\varepsilon' + i\varepsilon''$. For metals, the frequency dependent dielectric constant is accurately modeled using the series of tabulated Lorentz-Drude oscillator terms detailed in Chapter 1[51]. Absorbing thin films can be similarly modeled, as will be discussed in Appendix C. The region is illuminated at normal incidence from one end by an optical pulse with a Gaussian profile in frequency and time, and a spectral width sufficient to cover the entire wavelength range of interest (the visible spectrum, for example). The FDTD package then solves Maxwell's equations on a discrete grid within the region, simulating the propagation of the pulse in time. A sample MEEP file for carrying out an electromagnetic simulation is found in Appendix A.

The power spectrum through any plane is given by integral of the Poynting vector through the surface, as[59]:

$$P(\omega) = \iint_{surface} \hat{n}(x,y,z) \cdot \left\{ \vec{E}_\omega^{\,*}(x,y,z,\omega) \times \vec{H}_\omega(x,y,z,\omega) \right\} d^2x \qquad 2.1$$

where $\hat{n}$ is the normal vector to the surface, and $\vec{E}_\omega$ and $\vec{H}_\omega$ are the Fourier transformed electric and magnetic field vectors at each point. For flat planes, such as the top and bottom of the thin absorbing region of Figure 2.1(a), the calculation is straightforward, and corresponds to spectral methods used in other studies [18, 23, 24]. Determining the optical flux through an arbitrarily shaped surface, such as the skin of a metallic nanoparticle, is more complex, as one must find $\hat{n}$ at all points on the particle's surface.

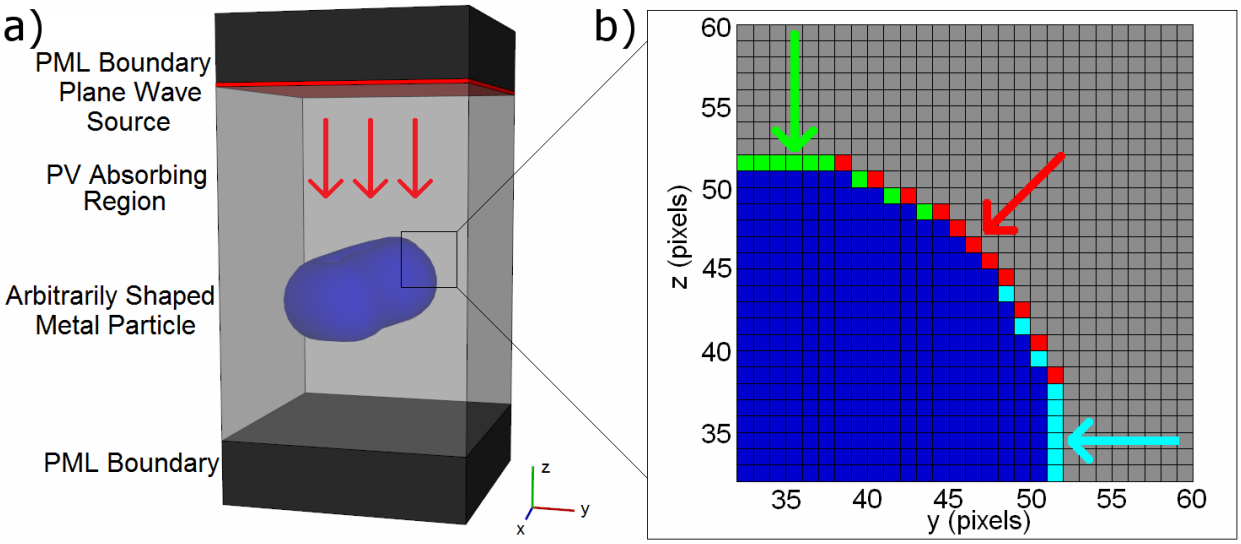

Figure 2.1 - (a) Sample simulation region, including a PV absorber with embedded metal particle. Boundary conditions are periodic in x and y with 'perfectly matched layers' (PML) in the z direction. (b) Representation of boundary types and corresponding normal vectors along the edge of the arbitrarily shaped particle.

Any FDTD simulation in Cartesian coordinates necessarily approximates geometry with cubic pixels – this discretization ensures that a metal particle rendered with sufficient resolution (greater than 1 pixel thickness at all points) has exactly 26 possible categories of surface boundaries, corresponding to face points, edge points, and corner points of a $3\times3\times3$ cube. Using the volumetric dielectric constant data from the FDTD simulation, a novel algorithm identifies the locations of each of the 26 different kinds of metal surface boundary points. An appropriate normal vector $\hat{n}$ is defined for each as a unit normal pointed from the skin of the metal into the bulk. A cross sectional representation of the different metal surface boundary types and the corresponding normal vectors is shown in Figure 2.1(b)[59].

The electric and magnetic field components in the region surrounding the metal structure are output for analysis as 4-D arrays (in x, y, z, and time). Field values on the surface points of a region of interest are transformed to 4-D (x, y, z, frequency) arrays using fast Fourier transform, yielding $\vec{E}_\omega$ and $\vec{H}_\omega$ at each point. The integration of Equation 2.1 is carried out as a discrete sum

over all surface points using the normal vectors assigned for each. The resulting spectrum quantifies the optical power entering the metal particle throughout the course of the simulation. Spectra through other flat planes of interest, such as the top and bottom of an absorbing film, are found by analogous methods using 3-D (x, y, time) data sets from the simulation. By appropriately comparing the energy entering and leaving a region of interest, we directly find the region's absorption spectrum without needing to solve for a steady state optical mode. Dividing each spectrum by that of the input Gaussian pulse, the results are normalized for clear interpretation. MATLAB code for carrying out this analysis is reproduced in Appendix B.

The analysis method described above is used to analyze a thin film absorber with embedded metal nanoparticles. The results presented here serve to demonstrate the advantages of the numerical approach as well as providing an overview of the optical processes that occur within the region. These results help to motivate the experimental work of subsequent chapters.

Broadband Results

First, we focus on an idealized thin film absorber with index of refraction $n = 1.8$ and absorption coefficient $\alpha = 5 \times 10^4$ / cm. These parameters are similar to the absorption band of an organic polymer PV system, which has a well-known tradeoff between absorption thickness and carrier transport[7-10], motivating the addition of plasmonic particles[17, 19, 25]. Spherical silver nanoparticles of 50 nm diameter are embedded in the absorber in a 100 nm spaced periodic square lattice to evaluate plasmonic enhancement. The simulated region, a single period of this arrangement, is shown in cross section in Figure 2.2(a).

Optical properties of the geometry are presented as spectra of the power absorbed in each region, normalized by the input power, as shown in Figure 2.2(b). We note two peaks in the

absorption spectrum of the metal particle (red curve) – the first at 270 nm is an intrinsic material absorption peak associated with the Lorentz-Drude model used for silver[51], the second at about 480 nm is associated with the LSP resonance of the silver nanoparticles, and can be tuned by changing the particle size / shape, or the surrounding material as discussed in Chapter 1. There is a corresponding enhancement in the absorption by the surrounding polymer-like PV material (black curve) as compared to the flat reference polymer absorption with no metal present (green curve). The total absorption in the region is also shown, to highlight the ability of the analysis to split the absorption into PV and metal components.

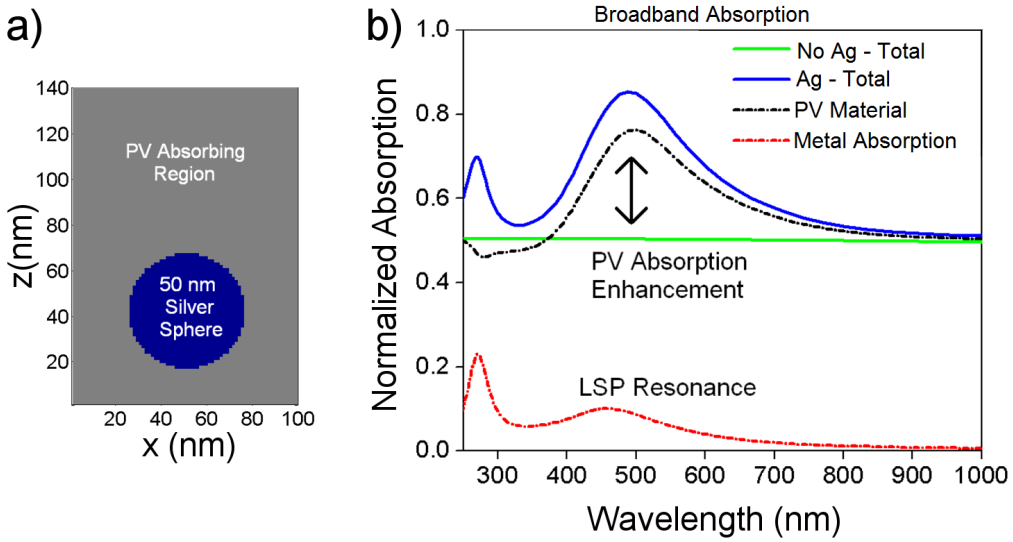

Figure 2.2 - (a) PV active region cross section with embedded 50 nm sphere. (b) Broad spectrum absorption properties, with and without the metal particle present. LSP resonance increases metal absorption at ~450 nm (red), with corresponding improvement in total (blue) and PV (black) absorption.

Note that data are presented with approximately constant film absorption across all wavelengths. This is an artificial parameter, though it allows us to easily see the full range of absorption effects in the visible and near-visible spectrum and study the optical physics at work. This analysis can be applied to studying specific PV material systems by modeling the frequency dependent dielectric behavior of the materials in question, as described in Appendix C.

Optical Absorption by Region

Before abandoning the simplified starting geometry of Figure 2.2, we note that the results can also help us gain physical insight into the optical processes contributing to absorption enhancement. To demonstrate, we break the simulation down into a number of arbitrarily shaped regions.

Very close to the metal particle, absorption enhancement is dominated by LSP enhancement of the near field optical intensity. More light is focused in the near field region, so more light is absorbed. Near field absorption is quantified by measuring the absorbed power within 5 nm thick spherical shells of PV material that surround the metal particle, as diagrammed in Figure 2.3(a). We note that the near field absorption enhancement falls off very quickly with distance (over a distance of ~15 nm). In thin film PVs that are significantly over this thickness (on the order of 100 nm, for example), only a small fraction of the absorbing volume should be expected to benefit from near field effects.

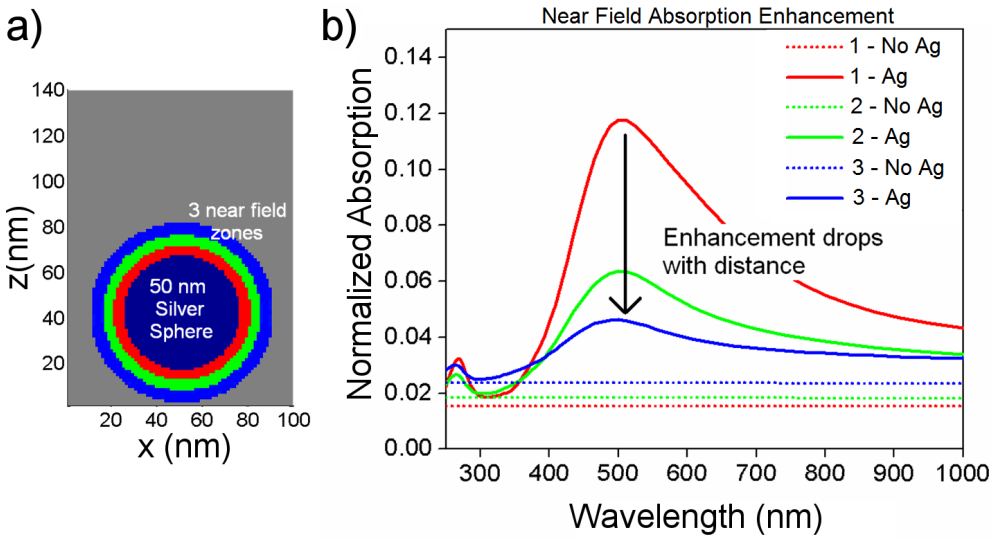

Figure 2.3 - (a) 5 nm concentric shells surrounding the silver nanoparticle. (b) Absorption spectra of the thin concentric shells of PV material with and without the metal particle present.

In addition to the near field regions, we consider three planar zones in the absorbing polymer, centered 20, 45, and 70 nm above the silver particle layer, as shown in Figure 2.4(a). The absorption spectra of these regions are shown in Figure 2.4(b), for cases both with and without the metal present. Fabry-Perot type reflection and interference effects[21,26] are evident, with peaks and troughs in absorption depending on the distance between the absorber and the metal particle. In this far field region, absorption enhancement is determined primarily by the interference between the incoming and backscattered light (though note that 'far' field here assumes the region is within the coherence length of the source).

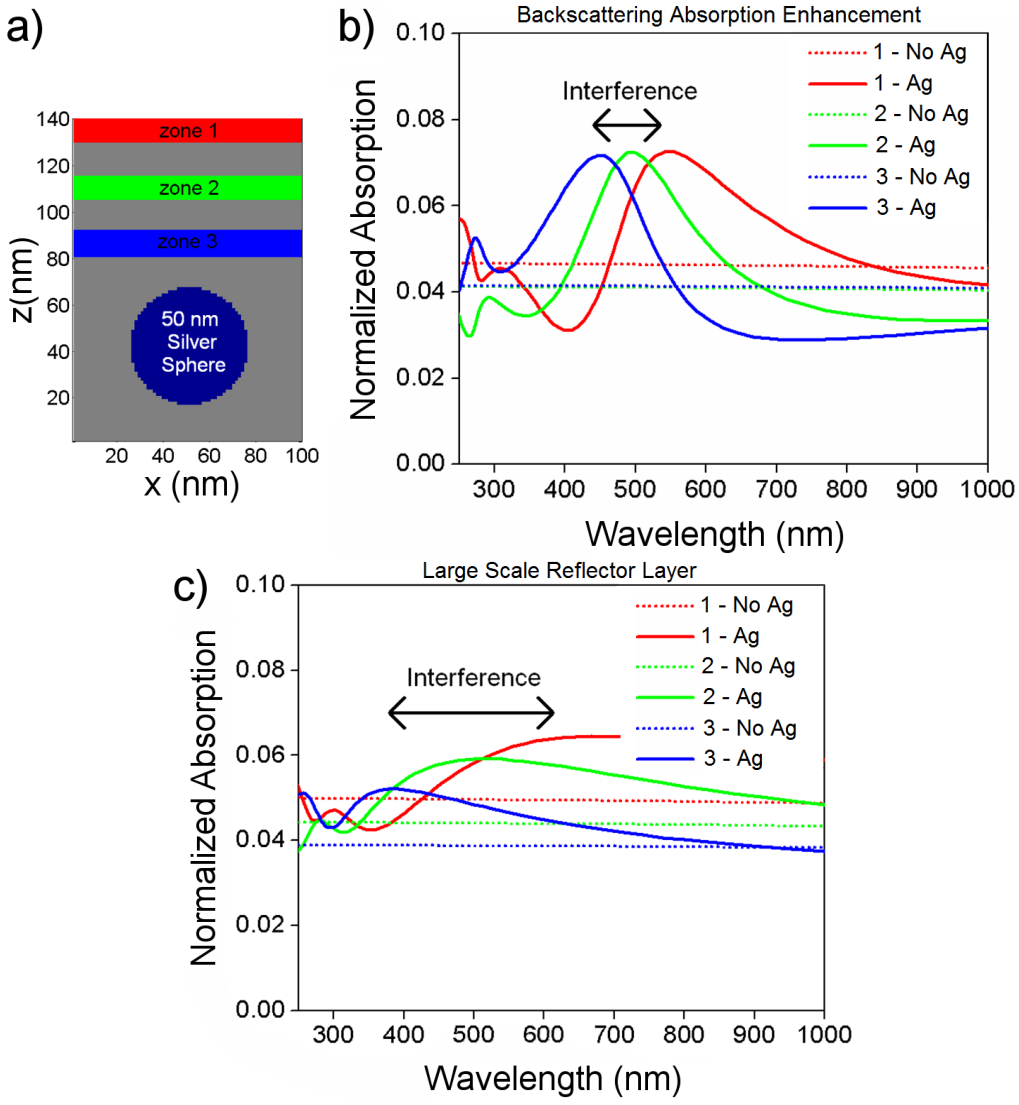

Figure 2.4 - (a) 10 nm thick zones of interest above the metal particle layer. (b) Absorption spectra of the regions of (a), with notable interference effects. (c) Absorption spectra similar to (b), with a purely reflective, large sized planar silver reflector used in place of the nanoparticle array.

Of particular interest, we calculate the interference pattern when a 50 nm thick planar silver reflecting surface of size >> λ is used in place of the sub-wavelength metal particle, the results of which are plotted in Figure 2.4(c). The large planar reflector is specified to fill the same fraction of the cell's cross section as the array of metal particles. Comparing Figures 2.4(b) and 2.4(c), the interference pattern caused by the plasmonic metal particles is stronger and more wavelength selective (confined near to the LSP resonance) than a pure reflection from the same amount of metal. This effect is in line with the idea of resonantly improved scattering cross sections described in Chapter 1. Near the LSP resonance, a particle scatters as if is larger than its physical dimensions. Off resonance, light will have a minimal interaction with the particle, and will be passed through the particle layer. This important result will be expanded upon in the next chapter, allowing plasmonic particles to be employed as wavelength selective back reflectors for PVs[16, 61].

Lastly, we compare the relative contributions to the total PV absorption enhancement due to near and far field components, plotted in Figure 2.5. The two contributions are equal at the peak, underlining the importance of simultaneously considering the near and far field mechanisms. Additionally, unlike some previous simulation studies, we demonstrate a direct comparison of absorption over a broad spectrum between several volumetric regions.

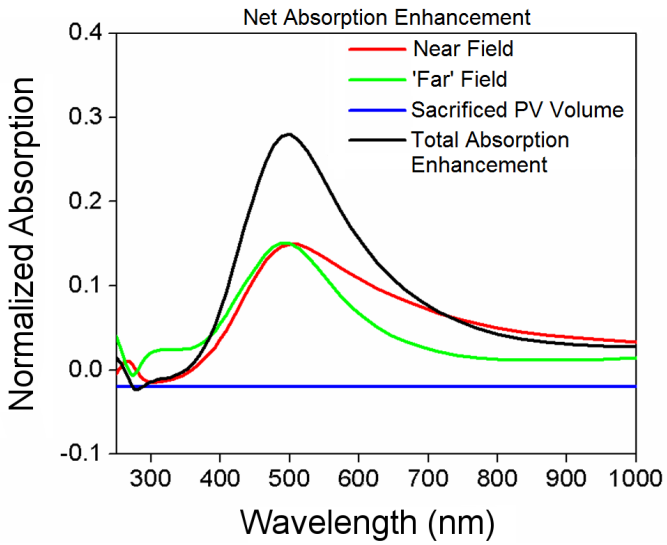

Figure 2.5 - Contributions to the total absorption enhancement from near and far field effects. Note that the metal particle takes up a fraction of the PV material volume when it is present, shown here as a negative enhancement.

An additional demonstration of the simulation methodology for analyzing arbitrary geometries and materials is found in Appendix C.

CHAPTER III

Harnessing Scattering Properties: Metal Nanoparticles as a Wavelength Selective Backscattering Layer

In Chapter 2, a simplified numerical analysis was carried out to clarify the optical phenomena responsible for absorption enhancement in thin film PVs with plasmonic metal nanoparticles. In the region of absorbing material above a nanoparticle layer, strong interference effects were evident. Absorption in the region was increased due to constructive interference between the incoming light and that that is backscattered. Importantly, the interference effects were found to be stronger per amount of metal and more wavelength selective than a purely reflective metal surface of size >> λ.

This work motivated the experimental investigation of a particle layer as a back reflector for semitransparent PV. Unlike previous demonstrations[17-19] of plasmon-enhanced PV, the particles are placed outside the electrical pathway of the cell, avoiding the potential for non-radiative carrier losses at the particle surface when it is placed within the semiconductor junction. Additionally, we aim to show that the tunable LSP resonance of the nanoparticle layer can be employed as a wavelength selective backscattering layer for semitransparent PVs, potentially providing greater flexibility and spectral tunability than a large scale metal backreflector, with application to light management in spectrally selective multijunction PVs[16,61].

Device Fabrication

As a proof of concept, we placed a silver nanoparticle monolayer underneath an inverted organic PV device as shown in Figure 3.1(a), physically separating the plasmonic layer from the active region. The whole device was fabricated bottom up, starting from creation of an ordered pattern of Ag nanoparticles on glass substrates (1 mm thick) using nanosphere lithography[62-65]. Polystyrene particles (200 nm in diameter), functionalized with carboxylic acid ligands, were spin-coated at 3500 revolutions per minute for 40 seconds to form a hexagonally close packed monolayer covering approximately 1 cm^2 area (inset, Figure 3.1(b)). The polystyrene sphere layer was then used as a mask to evaporate 20 nm of silver. The subsequent lift off of Ag by ultrasonication formed an ordered array of 45 nm wide and 20 nm high particles separated by 200 nm as shown in Figure 3.1(b). Some planar silver regions are seen on the sample surface as well where hexagonal close packing of the polystyrene spheres is non-ideal[62].

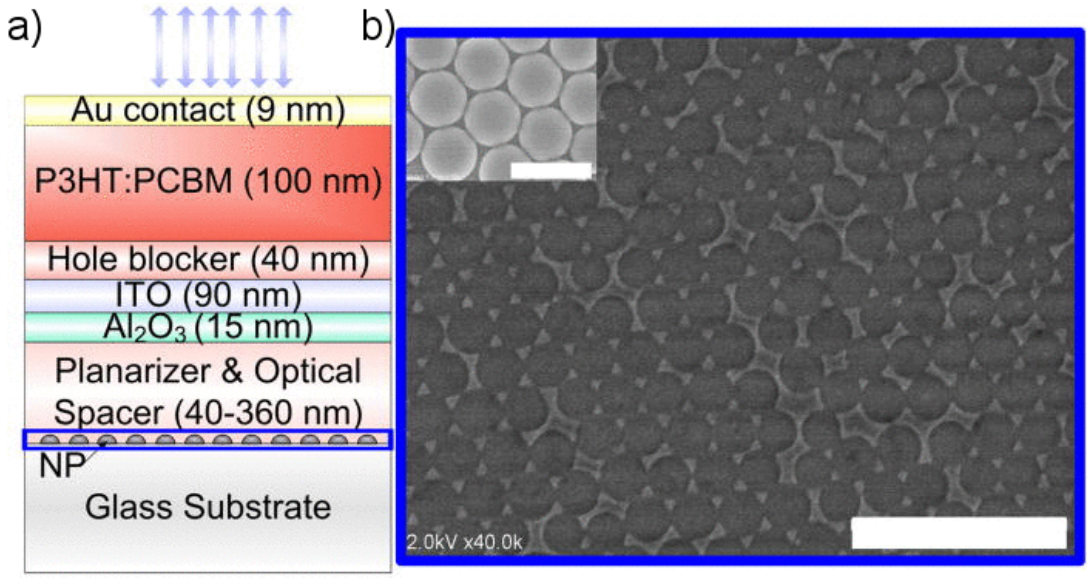

Fig 3.1 - (a) Schematic of the inverted organic polymer PV fabricated with Ag nanoparticles (label NP) placed outside the photoactive region. Device is illuminated from the Au semitransparent contact. (b) Silver nanoparticle layer imaged by SEM. Inset: monolayer of 200 nm diameter polystyrene particles used for nanosphere lithography (scale bar 300 nm).

After patterning the plasmonic silver particle layer, nanoparticles were encapsulated in a ZnO layer of 80 to 360 nm. This material acts as a planarization layer, as well as an optical spacer. Tuning the distance between the scattering nanoparticle layer and thin film PV allows tuning the available optical modes and interference effects as discussed in Chapter 2. An Al_2O_3 layer (15 nm thick) was deposited on top of the ZnO by atomic layer deposition as an insulator between the plasmonic layer and the top PV. Following this an Indium Tin Oxide (ITO) (40 ohm / square measured resistivity) layer was deposited (90 nm thick) as the bottom transparent contact and was coated by a hole-blocking layer of ZnO (40 nm thick)[66]. The organic photovoltaic active layer was formed by a spin coated (700 revolutions per minute for 20 s) 12 mg / ml solution of poly-3-helythiophene and phenyl-C61-butyric acid methyl ester (P3HT:PCBM) (1:0.8) in dichlorobenzene. Finally, 9 nm thick gold was deposited by e-beam evaporation on the organic layer as the semitransparent top electrode.

Device Performance

This inverted PV is illuminated through the thin Au top layer and the photocarriers generated within the active layer are collected as electrons from ITO, via a hole blocking layer, and holes from the high work function Au electrode. Figure 3.2 shows the current density vs. voltage plot of the inverted PV with metal particles (empty squares) and a reference inverted PV without the Ag (black squares), under AM1.5 illumination. The inverted Ag nanoparticle PV shows higher short circuit current density (J_{sc}) (1.9 mA / cm^2) than the reference (1.03 mA / cm^2). This nearly two-fold increase in photocurrent is attributed to enhanced exciton generation by resonant backscatter of the incident light from the metal particles to the PV active layer. These results corroborate the previous theoretical predication of significant 'long range' (> ~20

nm) plasmonic backscattering from a particle layer. In addition to the improved photocurrent, the PV including Ag particles also shows a slightly higher open circuit voltage (V_{oc}) (0.37 V) compared to reference PV (0.33 V). Improvement in V_{oc} is attributed to the increased photocurrent (I_p) of the silver nanoparticle inverted PV, following the Shockley relation[67]:

$$V_{oc} \propto \ln\left(I_p / I_s + 1\right) \tag{3.1}$$

where I_s (~1 μA) is the reverse saturation current. We justify the above by taking the V_{oc} ratio between the Ag nanoparticle based and reference inverted PVs, $V_{oc}^{AG} / V_{oc}^{REF} = 0.37 / 0.33$, which is identical to the ratio between the respective photocurrent expressions:

$$\ln\left(I_P^{MNP} / I_s + 1\right) / \ln\left(I_P^{REF} / I_s + 1\right) = \ln(191) / \ln(104). \tag{3.2}$$

Also, the overall power conversion efficiency in the Ag nanoparticle inverted PV (0.27%) increased by a factor of 2.4 in comparison to the reference PV (0.11%). Therefore, this plasmonic device architecture is seen to improve J_{sc} and the power conversion efficiency of the inverted PV by backscattering the incident light to the absorber layer from outside the active region.

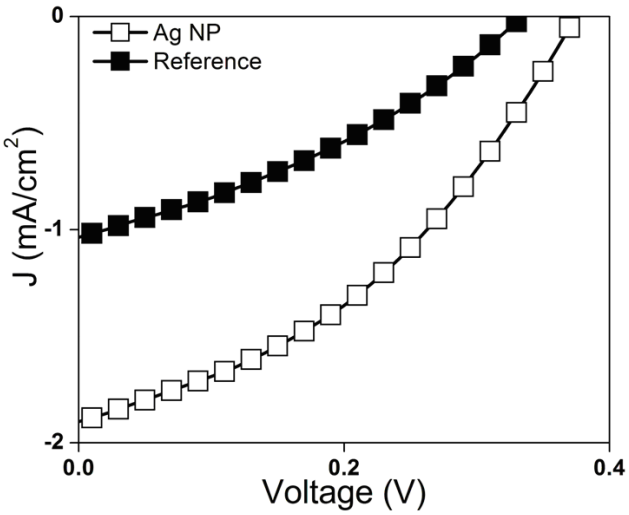

Fig 3.2 - Current density / voltage (*J-V*) characteristics under AM1.5 illumination of the inverted PV with Ag metal nanoparticles (white squares) with 80 nm optical spacer and a reference inverted PV (black squares).

Interference Effects and Modulation

We study the performance of our inverted plasmonic PV by modulating the backscattering using the optical spacer layer, to verify our expectation that absorption enhancement depends on the interference effects between the incoming and backscattered light. The interference is determined by the distance between the absorber and the scattering particle layer. Figure 3.3 shows the J_{sc} of the devices measured under AM1.5 with the optical spacer thickness varied from 80 to 360 nm. A periodic change in J_{sc} is observed with the optical spacer thickness.

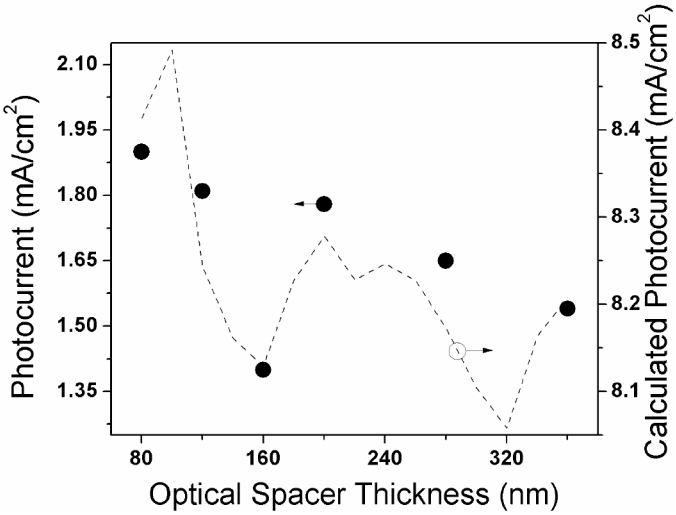

Fig 3.3 - Experimental (black circles) and calculated (black dashed line) photocurrent with varying optical spacer thicknesses under AM1.5 illumination.

To elucidate the physics underlying the modulation of J_{sc} by the optical spacer, an EQE (external quantum efficiency) measurement was carried out. Figure 3.4 shows the EQE of three devices with optical spacer thickness 80 nm (black circles), 120 nm (red circles) and 200 nm (blue circles) with distinct peaks, indicated by the dotted lines, at 570, 495 and 530 nm wavelengths respectively. Since photocurrent is a multiplication of EQE with AM1.5 intensity, the shifts in EQE peaks can cause changes in photocurrent with the optical spacer thickness as observed. We attribute above EQE peaks to resonant optical modes within the cavity, formed by

tuning of the backscattering from the Ag particle layer via an optical spacer. Importantly, as shown in the inset of inset Figure 3.4, irrespective of the spacer thickness the Ag nanoparticle inverted PVs (black, red and blue circles) show higher EQE compared to a reference inverted PV without metal (black line) justifying the higher photocurrent observed for the Ag nanoparticle inverted PV in Figure 3.2(a).

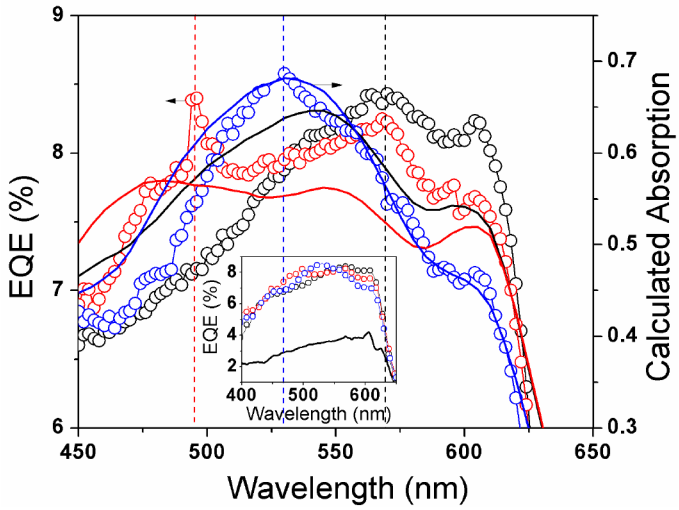

Figure 3.4 - EQE of the Ag nanoparticle based PV with optical spacer thicknesses of 80 nm (black circles), 120 nm (red circles) and 200 nm (blue circles). Absorption in the PV absorber was calculated using a weighted average between transfer matrix and finite difference time domain methods. The dashed lines indicate the EQE peak positions. Inset shows the EQE of the reference inverted PV without metal (black line) together with the EQE of the Ag nanoparticle PVs.

To verify our understanding of the experimental results, full field simulations were performed on the inverted PV geometry using the methodology of Chapter 2. The optical constants used in for P3HT:PCBM, Au, ITO, ZnO, Al_2O_3 and Ag were obtained from literature[68]. FDTD calculated active layer absorption peaks, with varied optical spacer thicknesses, were found to closely follow the EQE curves. However, the magnitude of these absorptions did not corroborate the EQE results within the off-resonance wavelength range. We attribute this to the non-uniformity of the deposited particles (SEM, Figure 3.1(b)), including the presence of silver islands where nanosphere lithography patterning is non-ideal. The simulation,

treating idealized nanoparticles only, was unable to account for the nonuniformity and corresponding spectral broadening and off-resonance reflections of the actual Ag layer.

As an alternative to FDTD, the absorption within P3HT:PCBM was modeled using the transfer matrix method[68-71], treating the metal nanoparticle layer as a single layer with effective optical properties matched to transmission measurements. This approach captured some of the resonant scattering, as well as the ensemble reflection effect of the nanoparticles, generating a modest fit to the measured EQE peaks.

A weighted average of the P3HT:PCBM absorptions calculated from both transfer matrix and FDTD was used to capture the ensemble reflection silver islands and resonant backscattering from LSP resonance, respectively (Figure 3.4). It is seen that the absorption peaks for 80 nm (black line), 120 nm (red line) and 200 nm (blue line) optical spacer thicknesses match approximately to the corresponding EQE peaks at the dotted lines. This clearly indicates that optical modulation of the backscattering is the direct cause of the change in the EQE. Furthermore, by considering unity internal quantum efficiency, we calculate the J_{sc} using the calculated P3HT:PCBM optical absorption for varied optical spacer thickness (black dashed line in Figure 3.3). It is evident that the photocurrent generated from the plasmonic PV is periodic with respect to the optical spacer thickness agreeing closely with the experimental results.

Application to Semitransparent Photovoltaic Systems

In Figure 3.5, the optical transmission of the Ag particle coated substrate (dashed red line), shows a dip at 525 nm wavelength, corresponding to the plasmon resonance of the Ag nanoparticles. In contrast, the off-resonance light passes through at approximately 80% intensity, which is considerably greater than a comparable 20 nm thick film of planar Ag (black line).

Therefore, the Ag nanoparticles have the potential to function as a wavelength selective backscattering layer, providing solar energy capture (as demonstrated above) while sustaining an excellent off-resonance optical transmission for semitransparent PVs. Furthermore, wavelength selectivity could allow one to stack multiple metal particle back reflectors tuned to different resonance wavelengths to be used with a tandem cell structure as illustrated in the inset of Figure 3.5. The enhanced backscattering can be independently tuned for each absorber and corresponding metal particle layer via an optical spacer, as above, allowing enhanced photocurrent and facilitating current matching among different junctions.[36-38]

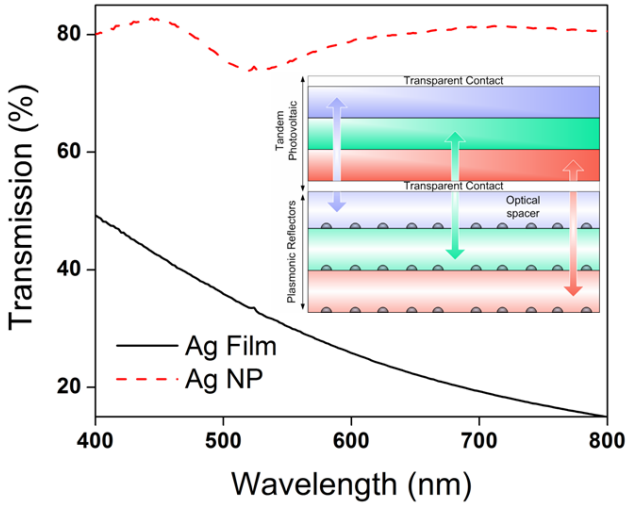

Figure 3.5 - Optical transmission of a monolayer of Ag nanoparticles (red line) and a 20 nm thick Ag film (black line) on glass slides. Inset shows a schematic of a proposed plasmonic nanoparticle engineered multi-junction inverted PV with multiple plasmonic backscattering layers. The optical spacer thickness is varied to maximize light harvesting for different wavelength bands via the optical cavity effect.

A number of other optical structures could also be used to realize wavelength selective backreflectors for PV (e.g. distributed Bragg reflectors[72, 73], photonic crystals[73]), though the strong interaction between light and metal for the plasmonic case allows significant modulation of light with a single sub-λ particle monolayer, rather than requiring a multilayer dielectric stack of size > λ. Additionally, the LSP resonance consists of a single tunable peak, whereas dielectric

structures managing light through interference alone can demonstrate high order peaks and resonance shifts with incident angle of light[72].

CHAPTER IV

Anisotropic Metal Nanostructures: Wavelength and Angle Selective Scattering

The previous chapters have made the case for enhancing absorption in semitransparent PVs by harnessing the long range backscattering off an array of plasmonic metal nanoparticles. The resonant nature of scattering allows such a light management scheme to be wavelength selective. In this chapter, we seek to expand this idea to both wavelength and angle selectivity by further engineering LSP resonances. This strategy can be used as a tool to realize a more advanced type of semitransparent PV cell: an angular selective photovoltaic window[39-42].

Semitransparent PVs have received recent attention as a solution for building integrated photovoltaics[28-35]. Integrating a semitransparent PV onto a building window can harness a large portion of incident sunlight that is otherwise reflected or converted to heat, exceeding the total light available to rooftop PV in commercial scale structures[28]. However, a conventional semitransparent PV suffers from an inherent tradeoff between the amount of light that is transmitted vs. the amount that is absorbed to be converted into photocurrent. Some transparent solar cells, harvesting only in the UV and IR regions[30, 31], forgo approximately half the total energy of the solar spectrum carried by visible wavelengths. For cells which collect visible wavelengths[33-35], either the window quality or the absorption and corresponding power conversion efficiency remain seriously limited.

We propose that the absorption vs. transmission tradeoff can be lifted if one separates the angles over which transparency and light harvesting are required. An angle selective semitransparent PV, designed for window quality transparency to normally incident light and improved harvesting of angled light (including direct sunlight) is diagrammed in Figure 4.1, along with a plot of the time-averaged angular availability of direct insolation[74].

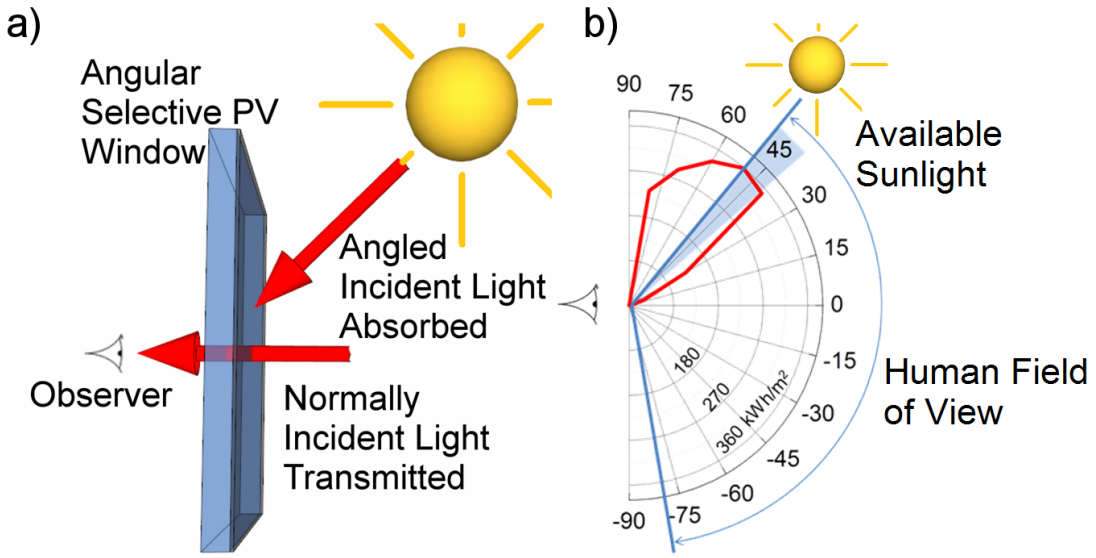

Figure 4.1 (a) Angle selective photovoltaic window, designed for transparency to normally incident light and harvesting of angled light, including direct sunlight. (b) Yearly available direct sun power on the sidewalls of an office building in Los Angeles, CA plotted vs. elevation angle.

Anisotropic Metal Nanoparticles: Principles

To realize the device described above with plasmonic metal nanoparticles, the resonant LSP response must demonstrate angular discrimination. At normal incidence, visible light should be off resonance for high transmission. Angled light should be on resonance for strong interaction with the metal particle layer and resonant backscattering effects as demonstrated in Chapter 3. Metal particles that have anisotropic shape (unequal width and height) present different profiles to normal vs. angled light, and can be employed to realize this effect[39, 40].

The scattering resonance of an anisotropically shaped metal nanoparticle depends on the polarization direction of the light with which it is illuminated[11]. The polarization is in turn determined by the angle of incoming light. Revisiting the calculation of metal nanoparticle polarizability α from Chapter 1, we note that closed form analytical solutions exist for the case of anisotropic ellipsoidal particles. For light polarized along the *i*th principle nanoparticle axis[11, 75]:

$$\alpha_i = 4\pi a_1 a_2 a_3 \frac{\varepsilon - \varepsilon_m}{3\varepsilon_m + 3L_i(\varepsilon - \varepsilon_m)} \tag{4.1}$$

where a_i is the length of the semi-axis along the *i*th dimension, and L_i are geometrical parameters given by:

$$L_i = \frac{a_1 a_2 a_3}{2} \int_0^\infty \frac{dq}{\left(a_i^2 + q\right) f(q)} \tag{4.2}$$

with:

$$f(q) = \sum_{i=1}^{3} \sqrt{q + a_i^2} \tag{4.3}$$

satisfying $\sum L_i = 1$. For a sphere, each L term equals 1/3, and Equation 4.1 reduces to Equation 1.1.

For a vertically (z axis) aligned prolate spheroid with aspect ratio A, the expressions above can be simplified by defining the eccentricity e as[75]:

$$e = \sqrt{1 - \left(\frac{1}{A}\right)^2} \tag{4.4}$$

for which

$$L_z = \frac{1 - e^2}{2e^3} \ln\left(\frac{1 + e}{1 - e} - 2e\right) \tag{4.5}$$

and

$$L_x = L_y = (1 - L_z)/2 \qquad 4.6$$

in accordance with $\sum L_i = 1$ and $a_x = a_y$.

Calculating polarizability and the corresponding absorption and scattering cross sections (Equations 1.2, 1.3) of silver nanoparticles, we note a clear redshift of the LSP resonance for light polarized along the long (z) nanoparticle axis.

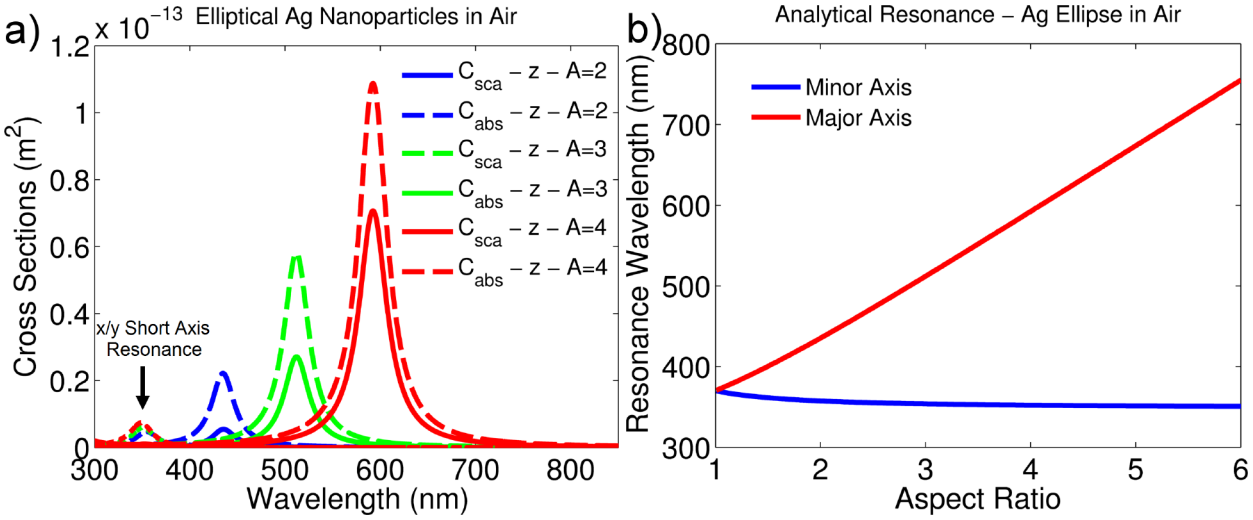

Figure 4.2 (a) Analytically calculated absorption and scattering cross sections for silver ellipses in air with aspect ratios 2 (blue), 3 (green), and 4 (red). Light is polarized along the short (15 nm) x / y axes (far left peaks) or along the major axis (dashed lines / solid lines). (b) Analytical LSP resonance frequencies vs. aspect ratio.

Increasing nanoparticle aspect ratios allows tuning of the longwave LSP resonance across the full width of the visible spectrum. The short axis resonance does not shift with aspect ratio, remaining in the blue / UV range. To realize angle selective management of visible light, we propose placing an array of vertical metal nanorods behind a thin film semitransparent PV layer as diagrammed in Figure 4.3[39, 40]. Normally incident light is polarized along the short nanoparticle axis, for which visible wavelengths are off resonance. This light is transmitted through the nanoparticle layer with minimal attenuation, suffering only a single pass through the thin PV absorbing layer. Transverse magnetic (TM) polarized angled light has a polarization

component along the long nanoparticle axis, exciting the visible λ LSP resonance. This light is backscattered to the thin film PV layer, improving absorption of angled light. Similar to the experimental demonstration of Chapter 3, we note that the metal nanoparticle layer is placed outside the PV junction, preserving the electrical properties of the solar cell and allowing independent optimization of the PV and light management layers.

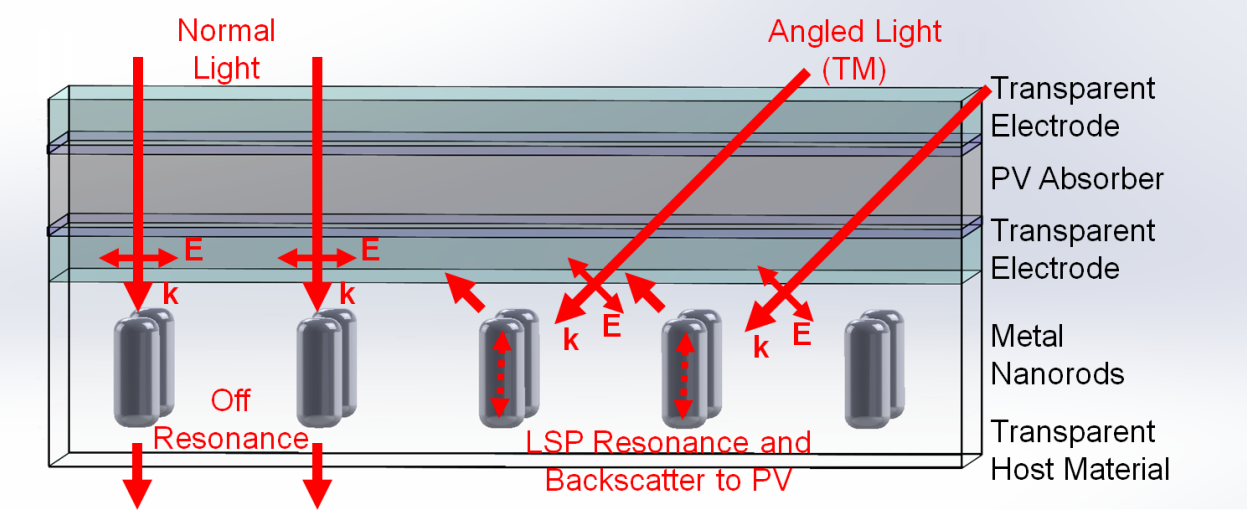

Figure 4.3 - Proposed geometry for angle selective semitransparent photovoltaic with anisotropic metal nanoparticle backscattering layer.

Modeling Metal Nanoparticles Under Angled Illumination

Before considering the full system of Figure 4.3, it is instructive to consider numerical simulations of anisotropic metal nanorods under angled illumination. Finite element simulation of silver ellipses under angled illumination are carried out in COMSOL Multiphysics[76] using the geometry of Figure 4.4(a) and a sweep of 25 wavelength values from 350 to 850 nm. Note that the half sphere simulation region takes advantage of symmetry across the $y = 0$ plane. Optical properties of metal in the simulation are realized with the same model described in Chapter 1. Similar results can be realized using the FDTD method as described in Chapter 2, though the scattered field solution formulation in COMSOL makes it particularly easy to

separate the input and scattered field components, facilitating direct calculation of absorption cross section via[77]:

$$C_{abs} = \iiint_{metal} Q_{heat} d^3x / I_0 \tag{4.7}$$

where Q_{heat} is the electromagnetic joule heating of the material (in W / m^3) and I_0 is the input optical intensity (in W / m^2). The scattering cross section is calculated as[77]:

$$C_{sca} = \iint_{surface} \hat{n} \cdot \vec{S}_{scattered} d^2x / I_0 \tag{4.8}$$

where the surface under consideration is a box surrounding the nanoparticle with outward pointing normal $\hat{n}$ and $\vec{S}_{scattered}$ is the Poynting vector of the scattered field. This is analogous to Equation 2.1, though for the case of outward going optical power (and only handling one frequency at a time).

For silver ellipses of 30 × 60 nm (aspect ratio A = 2) surrounded by air, analytical cross sections are calculated using Equation 4.1, 1.2, and 1.3. To account for illumination angle θ, cross sections are weighted by the trigonometric fraction of light along the major (z) vs minor (x / y) axes according to:

$$C(\theta) = C_z \sin(\theta) + C_x \cos(\theta) \tag{4.7}$$

Analytical and numerically calculated cross sections are plotted in Figure 4.4 for illumination angles 0^o, 30^o, 60^o, and 90^o. LSP resonances line up tolerably well, though we note that redshift of the longwave resonance is slightly increased (435 to 454 nm), and total resonance strengths are reduced due to finite nanoparticle sizes as discussed in Chapter 1. Angled properties show clearly split short and longwave resonances, the magnitudes of which vary with trigonometric angle as expected.

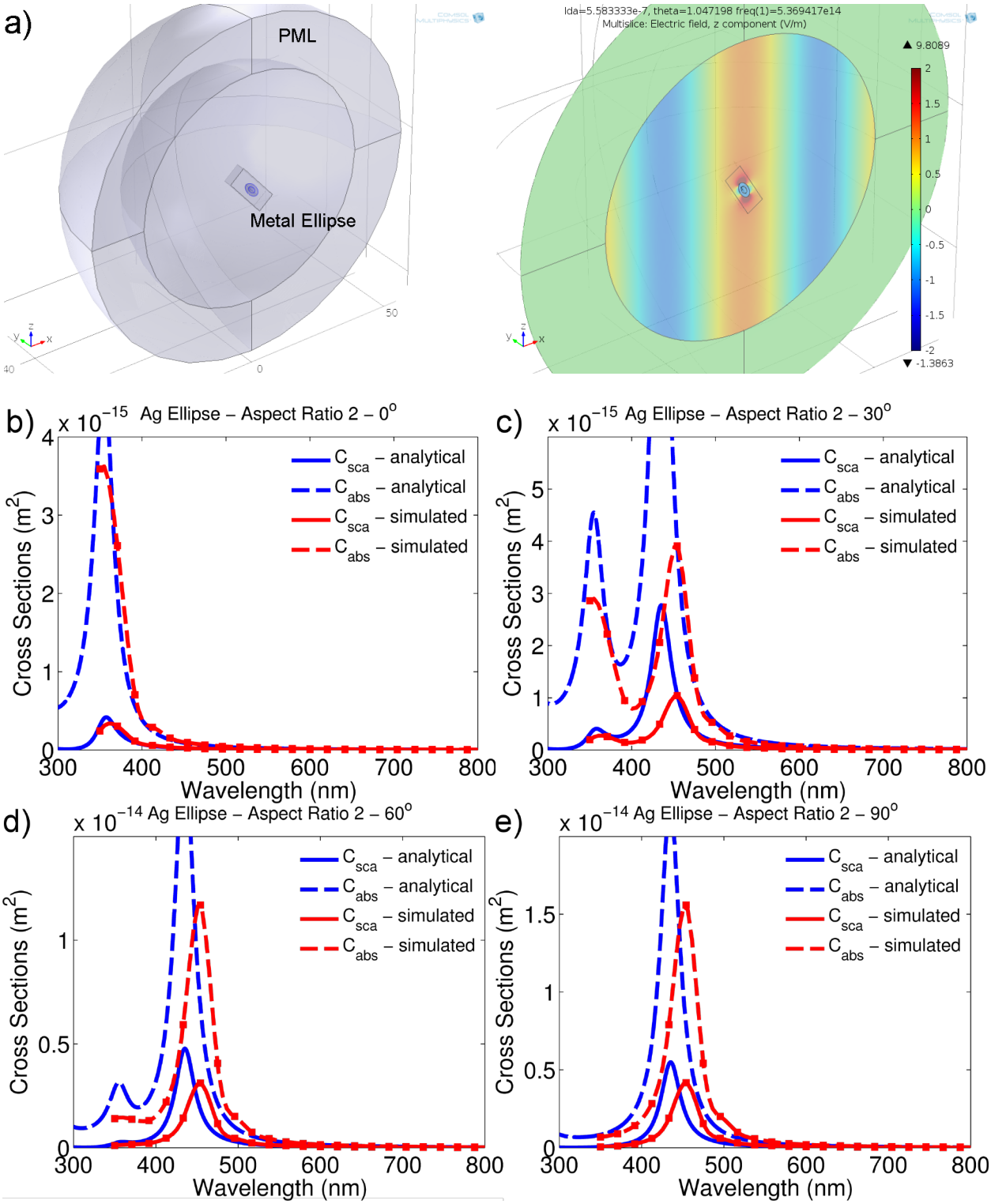

Figure 4.4 - (a) COMSOL simulation region and calculated fields for a metal ellipse angled with respect to incident light. (b-e) Absorption (dashed) and scattering (solid) cross sections for analytical (blue) and numerical (red) calculations at 0°, 30°, 60°, and 90° incidence, considering a 30 × 60 nm silver ellipse in air.

Analogous calculations for silver nanoparticles of aspect ratio 3 are plotted in Figure 4.5. As particle size increases and the assumption of size << λ begins to break down, the longwave LSP resonance redshifts further (512 to 547 nm) and decreases in magnitude as compared to the analytical expression, though there remains a strong mismatch in extinction on and off resonance.

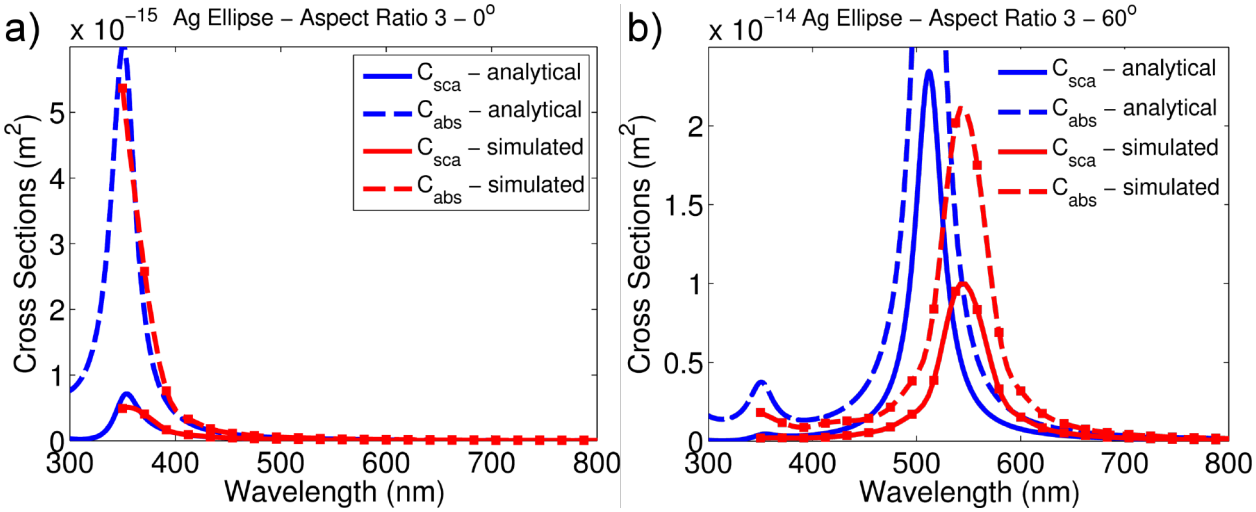

Figure 4.5 - Absorption (dashed) and scattering (solid) cross sections for analytical (blue) and numerical (red) calculations at (a) 0° and (b) 60° incidence considering a 30 × 90 nm silver ellipse in air.

Elliptical particle shape was chosen to take advantage of the existence of analytical polarizability expressions, though other anisotropic particle shapes are expected to demonstrate split LSP resonances as well. We additionally consider cylindrical silver nanorods in air by COMSOL simulation and compare the calculated absorption and scattering cross sections to the analytical ellipse expressions.

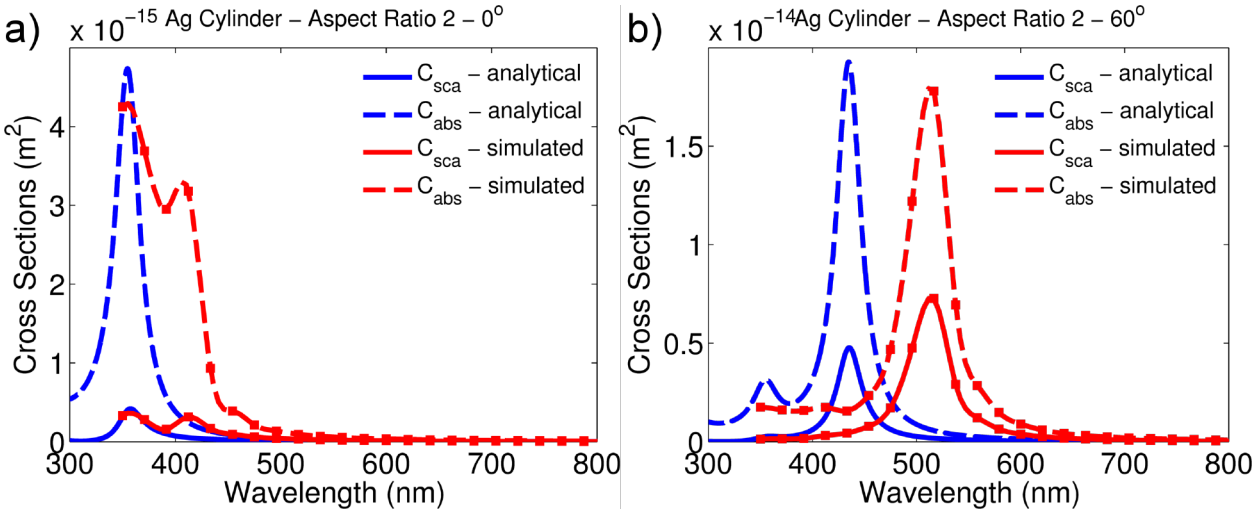

Figure 4.6 - Absorption (dashed) and scattering (solid) cross sections for analytical (blue) ellipse expressions and numerical (red) cylinder calculations at (a) 0° and (b) 60° incidence considering a 30 × 60 nm silver particle in air.

For the cylindrical nanoparticle of aspect ratio 2, the short wave resonance shows a double peak (355 and 406 nm), and the longwave resonance shows a significant redshift (435 to 512 nm), as compared to the analytical elliptical expressions, attributed to the change in shape. While the redshift is larger, the resonances remain well separated, so an array of cylindrical nanorods should also be appropriate for an angle selective scattering layer. Analogous plots for silver cylinders of aspect ratio 3 (30 × 90 nm) are shown in Figure 4.7, for which the longwave resonance shifts from 512 nm (analytical, elliptical case) to 621 nm (numerical, cylindrical case) due to both the change in shape and the increase in size toward λ. The total LSP resonance splitting in the cylindrical case can be tuned with aspect ratio the same as the elliptical case above. It is also worth noting that the total extinction magnitudes for cylinders (absorption and scattering) are reasonably well approximated by the analytical ellipse equations, excepting the extra redshifts.

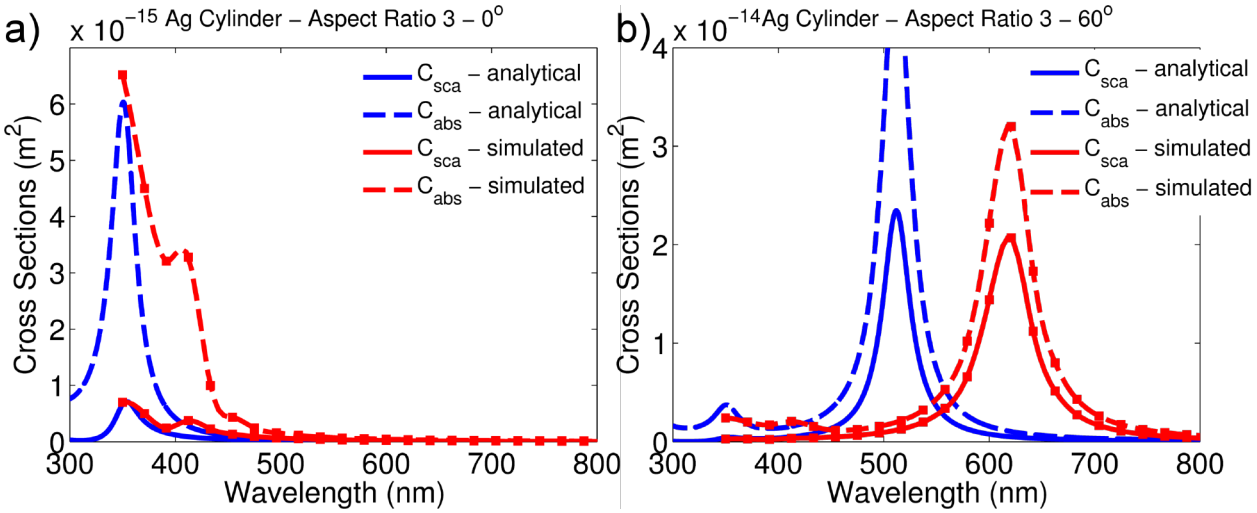

Figure 4.7 - Absorption (dashed) and scattering (solid) cross sections for analytical (blue) ellipse expressions and numerical (red) cylinder calculations at (a) 0° and (b) 60° incidence considering a 30 × 90 nm silver particle in air.

Metal Nanorod Angle Selective PV

The results above verify that an array of vertical silver nanoparticles of moderate aspect ratio (2.3) will demonstrate split LSP resonances with incident angle and polarization of light. For such an array to be used with a semitransparent PV layer, we suggest two additional design criteria. First, the short wave resonance should be as far to the blue / UV end of the spectrum as possible, so as not to interfere with transmission and color balance of transmitted light. Second, for ease of integration with other thin films, the nanoparticles may be encapsulated in transparent dielectric material (e.g. MgF with refractive index $n \sim 1.3$ or SiO_2 glass with index $n \sim 1.5$[50]).

The short wave resonance of silver in air is already close to the blue edge of the visible spectrum (~400 nm) and redshifts with the increasing refractive index of the encapsulation layer. Therefore, we consider the switch to aluminum nanoparticles, for which the primary LSP resonance is significantly further out into the UV range. Analytical calculations assuming elliptical particle shape result in the resonance vs. aspect ratio plot of Figure 4.8. Additional redshifts to the long axis / angled light resonance are realized by increasing nanoparticle size (50

× 150 nm) and switching to cylindrical shape. We also note that aluminum nanorods in this size regime favor scattering over absorption, limiting total optical losses.

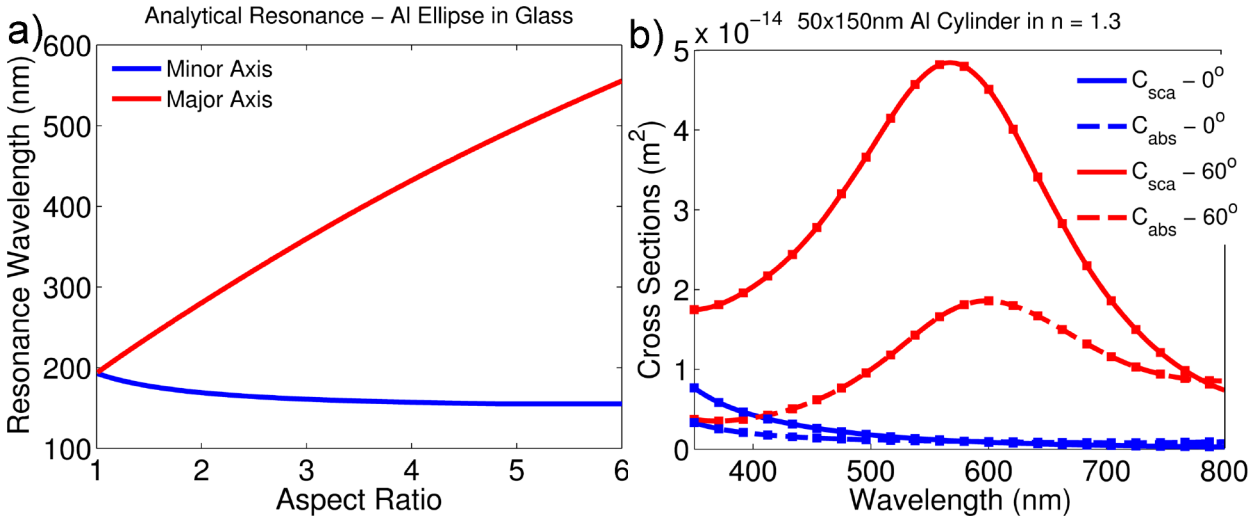

Figure 4.8 - (a) Analytical calculation of LSP resonance wavelengths for aluminum nanoparticles in n = 1.5 (elliptical assumptions). (b) Simulated absorption and scattering cross sections for a 50 × 150 nm aluminum cylinder in n = 1.3.

The optical properties of an array of such vertical metal nanorods are numerically simulated using a modified COMSOL Multiphysics model of a single nanorod / periodic cell with the geometry of Figure 4.9[40]. A background field consisting of an angled plane wave is defined, and the scattered field formulation is used to determine the complete steady state optical mode at each frequency of interest. Free space incident angle is adjusted within the n = 1.3 layer in accordance with Snell's law[55]. Floquet periodic boundaries[78] are defined in the x (angled light) direction to facilitate phase corrections of angled light leaving one side of the simulation region and re-entering the other side. Such a correction requires precise knowledge of the frequency and propagation constant of the source and cannot be implemented for a broadband time domain simulation like the one described in Chapter 2, hence the switch to a single frequency model (though approximate FDTD results can be realized by angling the geometry of interest with respect to the source plane and simulating multiple periods[39]).

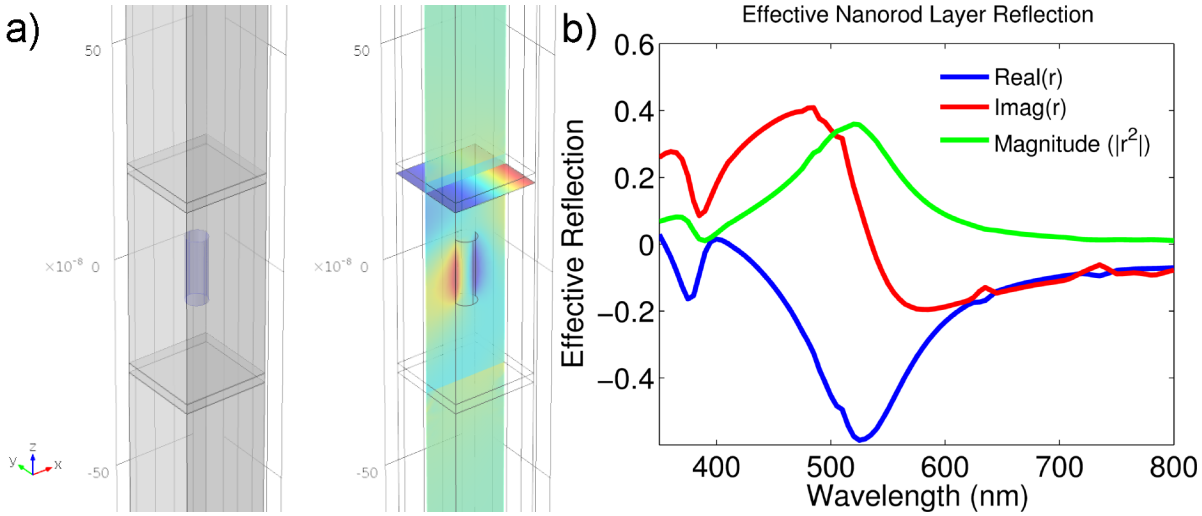

Figure 4.9 - (a) COMSOL multiphysics model of vertical aluminum nanorods. (b) Effective ensemble reflection coefficient for aluminum nanorod layer at 50 degree angled incidence.

Perfectly matched layers are defined above and below the nanoparticle layer to absorb light leaving the region. We note that the simulation is sensitive to the choice of boundary conditions - enforcing 'perfect' periodicity in the structure by using boundary conditions which only allow light scattered to known diffraction modes, the anisotropy of each individual scatterer tends to be masked by the diffractive properties of the infinite lattice as a whole, depending only on nanoparticle spacing (similar to reference [21]). Using PMLs relaxes the condition of perfect infinite periodicity (and a perfectly coherent source) to a pseudo-periodic case which allows the anisotropic extinction of each individual rod to dominate. We also note pseudo-periodicity relaxes the fabrication requirements for such nanorod arrays (discussed at length in Chapter 6).

Electric and magnetic field profiles in the planes above and below the nanoparticles are extracted from COMSOL and matched to the profiles of plane waves entering and exiting the region to extract the net amplitude and phase of light reflected by the ensemble nanoparticle layer, as a function of wavelength and incident angle[40]. The corresponding complex reflection and transmission coefficients for the layer are integrated with a planar transfer matrix formalism[68-71] to account for the optical modes and interference in a planar stack of

photovoltaic layers placed above the nanoparticle layer. By modeling plasmonic physics numerically and planar layers analytically, we seek to accurately account for the nanoscale physics of the plasmonic metal particles without requiring a full field simulation of the entire PV geometry for every choice of solar cell stack.

Optical absorption and transmission properties for a 50 × 150 nm aluminum nanoparticle array with 200 nm spacing placed behind a P3HT:PCBM organic photovoltaic stack are calculated and shown in Figure 4.10(a). A 40 nm thick P3HT absorption layer is assumed, with 30 nm ITO transparent electrodes and a single quarter wave (96 nm) antireflection coating on the front surface of refractive index n = 1.3 (e.g. MgF). At normal incidence (dashed curves), transmission through the system (blue) is maintained at greater than 50%. Under angled illumination (50°), absorption in the PV layer (red) increases (40 - 60%), with a corresponding drop in transmission and some light lost to absorption within the metal nanorods themselves (black).

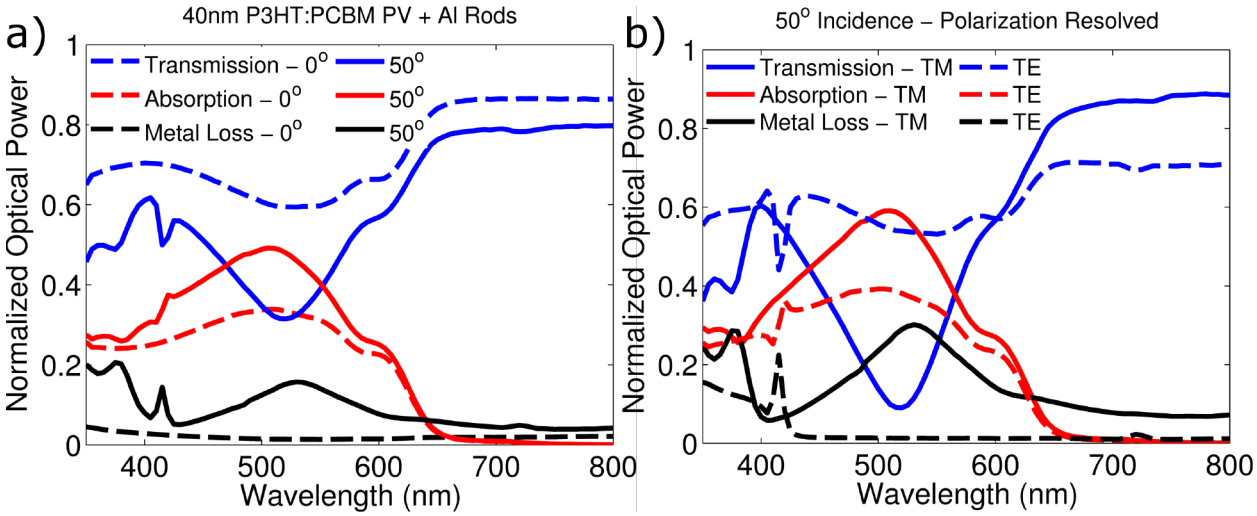

Figure 4.10 - (a) Optical properties for metal nanorod layer placed behind semitransparent organic PV, at normal (dashed) and 50° (solid) incidence, including transmission (blue), photovoltaic layer absorption (red), and metal nanorod absorption (black). (b) Optical properties at 50° angled incidence resolved into TE (dashed) and TM (solid) components.

Resolving the 50º angled light spectra by polarization (Figure 4.10(b)), we see that the main modulation of transmission, PV absorption, and metal losses occurs in the TM component, as expected, corresponding to light polarized along the long axis of the metal nanorods. Transverse electric (TE) light, polarized along a short nanorod axis regardless of incident angle, never excites a visible λ LSP resonance, and is thus not selectively managed with angle. It is possible to design plasmonic structures to scatter both polarizations of angled light (standing nanodisks rather than nanorods, for example), though such structures would not be as highly transparent to normally incident light. Additionally, the Fresnel equations dictate that angled light near Brewster's angle will have a more significant TM component after transmission from the air into the dielectric layers on the front surface of the PV cell, making targeting of TM light more advantageous at high angle.

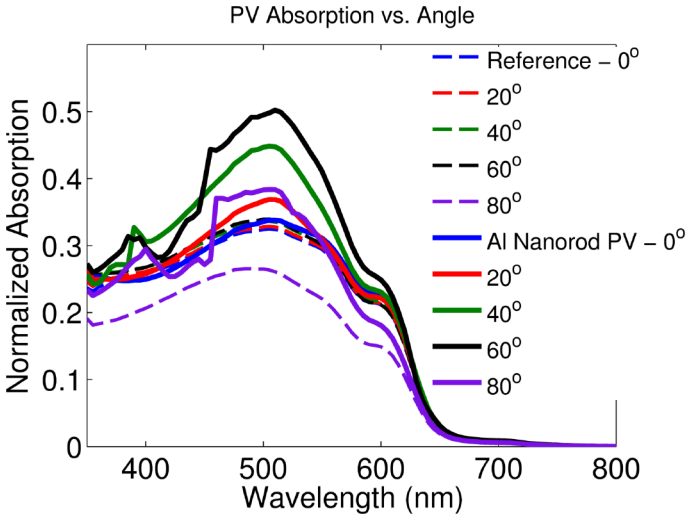

Figure 4.11 - PV absorption vs incident angle with (solid lines) and without (dashed lines) Al nanorod layer. Absorption increases with angle for the nanorod case.

Absorption spectra of the organic PV layer are plotted for various incidence angles in Figure 4.11. For a reference device (dashed curves) absorption is approximately constant with angle on 0 - 60º, and drops significantly at 80º (purple) due to reflection at the front air /

dielectric interface. The nanorod device (solid curves) shows increasing absorption with angle on 0 - 60°, and significantly improved absorption at 80° as compared to the reference.

As a measurement of the overall merit of the angle selective structure, the normal direction transmission vs. the integrated absorption of direct sunlight (weighted by the angular availability of Figure 4.1(b) and the AM1.5 solar spectrum) is compared in Figure 4.12. For a P3HT:PCBM organic PV alone (blue curve) transmission vs. absorption can be modulated with absorbing layer thickness, but maintains a transmission vs. photocurrent tradeoff. Adding metal nanorods (red circles) improves absorption (shifts right) while maintaining transmission in the normal direction. Contours showing the percentage by which absorption (and photocurrent) are improved are shown as well.

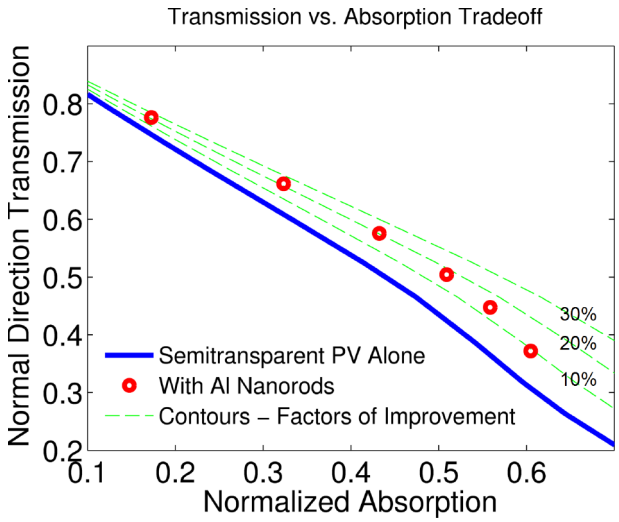

Figure 4.12 - Tradeoff between PV transmission (visible wavelengths, normal direction) and absorption (AM1.5 spectrum, weighted by incident angle) for a reference device (blue) with various organic PV absorbing layer thicknesses and with Al nanorods (red). Contours in green show factors of improvement in overall absorption at given levels of transmission.

Metal nanorods are useful to the device across the full range of absorber thicknesses / target transmission levels, though they show more improvement in the highly transmissive case where the first pass absorption of light is low and there is the greatest amount of light interacting with the nanoparticle backscattering layer. A maximum absorption improvement of 22% is found

for the angle selective PV window while maintaining a transparency of 60 - 70% to normally incident light.

Overall performance of this structure is limited by single polarization nature of the approach and by resonant absorption by the metal nanorods themselves. Metal losses are an intrinsic part of plasmonics, though we attempt to limit them by selecting nanorods which favor scattering, and note that visible metal losses are low for normally incident TM light and all off resonance TE light. Inherent plasmonic metal losses are only significant when the nanoparticles are also enabling angle selective absorption features.

Other structures such as distributed Bragg reflectors (DBRs) or photonic crystals could also be considered to provide angle selective management of backscattering (discussed further in Chapter 7), though the two approaches show different reflectivity behaviors with increasing angle: the high reflectivity peak of a DBR will continuously shift across the spectrum with changes in angle[72], whereas the plasmonic backscattering stays at a well defined frequency and simply increases trigonometrically with angle. Thus an array of plasmonic nanorods with resonance matched to the absorbing band of an accompanying PV will always backscatter the most useful components of angled light. Additionally, the strong interaction of light with metal requires fewer layers to realize significant spectral modulation (indeed, it is difficult to realize an angle selective PV with dielectric layers only as described in reference [40]). Finally, we note that simpler, purely geometrical approaches to window integrated PV have been proposed and tested, including 'Venetian blind' solar cells mounted horizontally between glass panes (or adjustably rotated)[29, 79, 80]. Such a system can be designed to realize superior absorption of angled light while maintaining transparency in the normal direction as dictated by the thickness and spacing of the blinds, though the nanoscale nature of the plasmonic approach described here

(and the alternate approach described in Chapter 7) has additional aesthetic value - the window will appear homogeneous to the naked eye rather than including a visible structure. This idea is expanded on in Chapter 5.

CHAPTER V

Beyond Photovoltaics: Application to General Wavelength and Angle Selective Optical Systems

Building on the results of Chapter 4, we now move our focus away from thin film photovoltaics and consider other applications of anisotropic metal nanorods in optical systems. Via LSP resonance parameters, an array of metal nanorods can be employed as a wavelength, angle, and polarization selective surface. Using these properties, we propose a novel multiscale architecture for realizing an adjustable 0 to ~100% transmissive filter for visible light. Such a filter is of active commercial interest for applications from optical bench hardware to adjustable privacy 'smart' windows[43-47].

Variable Transmission System: Multiscale Architecture

In the case of window mounted angle selective semitransparent PVs, angular properties are essentially considered passively - nanorods occupy a specific orientation, and their scattering is determined by the range of angles occupied by direct sunlight throughout the day. For an active adjustable system, we must be able to tune the nanorod angle with respect to the incident light of interest. Thus we propose placing nanorods on a corrugated, actuating transparent substrate as diagrammed in Figure 5.1. Pulling on the ends of the corrugated structure (perpendicular to the fold axis) causes it to lie flat. Metal nanorods oriented perpendicular to the surface will stand vertically in this configuration, allowing high visible transmission, in

accordance with the results of Chapter 4. Relaxing strain and allowing the structure to return to a crinkled state, nanorods on the surface rotate and present an angled profile to normally incident light, which will increasingly interact with the long nanorod axis and secondary, redshifted LSP resonance, modifying the layer's transmission spectrum.

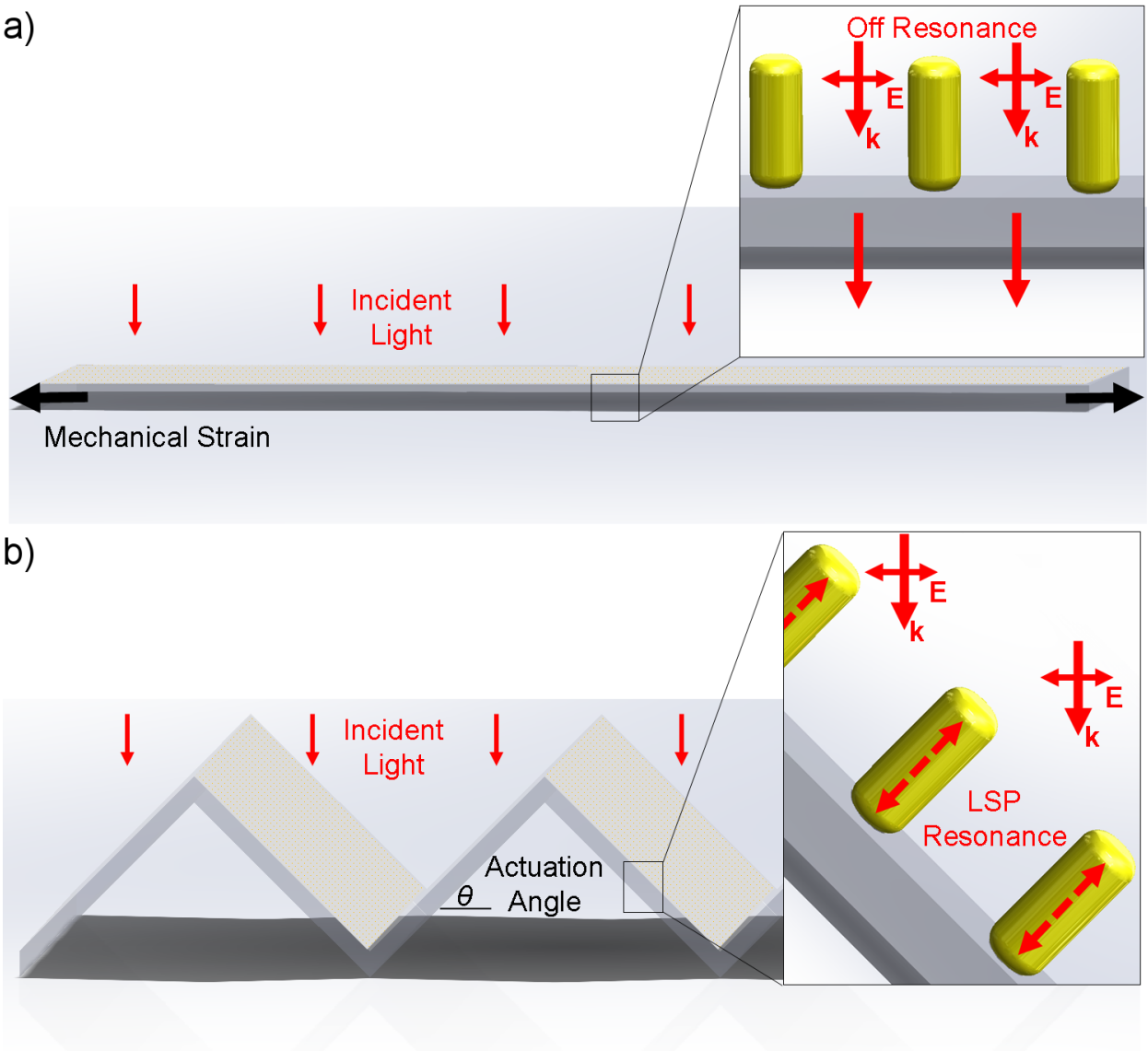

Figure 5.1 - Cross sectional view of proposed actuating structure with vertical metal nanorod coating. (a) Mechanical strain is applied to flatten the structure, corresponding to a highly transmissive state. (b) Relaxing strain and corrugating the structure allows increased interaction of light with long axis LSP resonance, modifying transmission spectrum.

As shown in Figure 5.1, the nanorod coating and the proposed corrugated structure can be realized at different scales. While nanorods must be at the sub-λ scale (10's of nm) to access plasmonic physics, the corrugated structure can be at the micron - 10's of microns scale and still remain small enough to be invisible (or appear homogeneous) to the naked eye. While the fabrication and characterization of the actuating origami structure is not a primary focus of this thesis, we note that recent progress has been made in this area[81-84], including the patterning of analogous corrugated polydimethylsiloxane (PDMS) structures[85-87] and paralyne[82, 88] structures, including the fabrication of actuating corrugated paralyne membranes using textured silicon substrates and liftoff techniques as seen in Figure 5.2[88]. Nanoparticles are assumed to be placed randomly on the surface, though the relative abundance of each nanorod type and the total effective nanorod density / spacing are assumed to be controllable. Colloidal metal nanoparticles prepared in solution[87, 89-90] and allowed to deposit on the surface could satisfy these constraints - vertical orientation remains a challenge, though could potentially be realized by a seeded growth process[91].

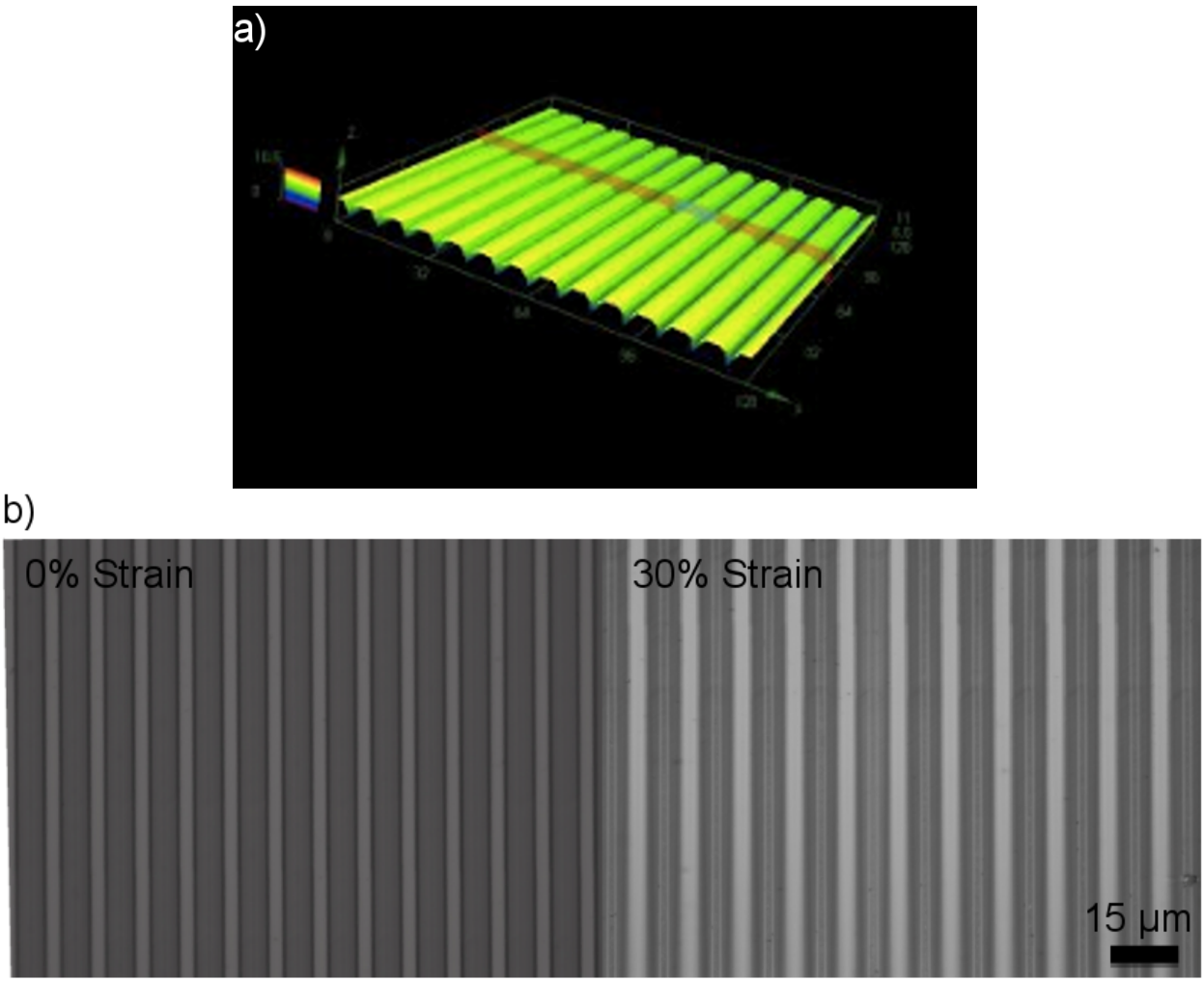

Figure 5.2 - (a) Atomic force microscopy (AFM) measurement of the surface profile of a corrugated paralyne membrane released from a textured Si template[88]. (b) SEM images showing actuation of structure with applied strain.

Variable Transmission System: Optical Model

For adjustable smart window applications, we seek to modulate the full width of the visible spectrum (380 to 780 nm) from 0 to ~100% transmission. As LSP resonances are somewhat narrowband, we populate the actuating surface with a variety of materials and aspect ratios of nanorods, each of which targets a separate region of the spectrum. Additionally, inhomogeneous broadening is added to the model by independently varying the nanoparticle

radii and heights over gaussian distributions with 5 nm standard deviation, both to better approximate real systems[87, 89-90] and to better cover the full visible range.

Four sets of metal nanorod parameters are selected: silver particles of radii 15 (+/- 5) nm and aspect ratios of 2 and 3.5, and gold particles of radii 15 (+/-5) nm and aspect ratios of 3 and 5. LSP resonance properties are calculated using the elliptical particle polarizability model described in Chapter 4[11, 75], assuming nanoparticles are surrounded by air. The two silver particle populations have long axis resonances at 411 and 485 nm respectively, while the gold rods manage the red end of the spectrum with LSP resonances at 586 and 693 nm. Short axis resonances for the silver particles are at 357 nm, kept outside the visible range to preserve high transmission of normal light. Gold rods show short axis extinction on the $\lambda < 500$ nm range, though gold enables management of the red end of the visible spectrum with even moderate nanoparticle aspect ratios - we accept the small visible optical losses at normal incidence for this reason. The corresponding extinction cross sections assuming a 40^{o} actuation / illumination angle for each nanoparticle type (including inhomogeneous broadening) and TM polarization are plotted in Figure 5.3. The relative influence of the short vs. longwave LSP resonances are weighted by the trigonometric fraction of the incident angled light that excites electron motion along the corresponding short vs. long axes (Equation 4.7).

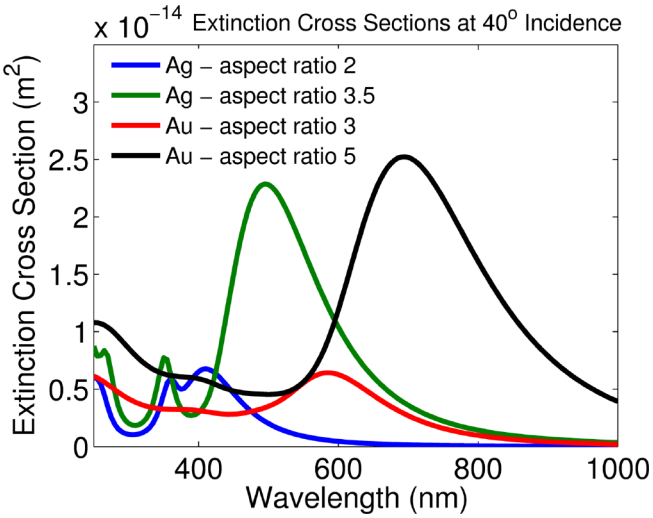

Figure 5.3 - LSP resonant extinction coefficients for selected metal nanorods across the visible spectrum assuming 40° angled illumination.

Extinction coefficients vary across the visible spectrum according to choice of metal and aspect ratio, while extinction coefficient peak magnitudes also vary with total particle size. To realize balanced modulation of the full spectrum, the fractional abundance of each type of rod is adjusted. Each of the peak heights of Figure 5.3 is scaled using the fraction of nanorods consisting of that type to analytically equalize the peak values, corresponding to 38.20% silver rods of aspect ratio 2, 11.32% silver rods of aspect ratio 3.5, 40.23% gold rods of aspect ratio 3, and 10.25% gold rods of aspect ratio 5, as plotted in Figure 5.4.

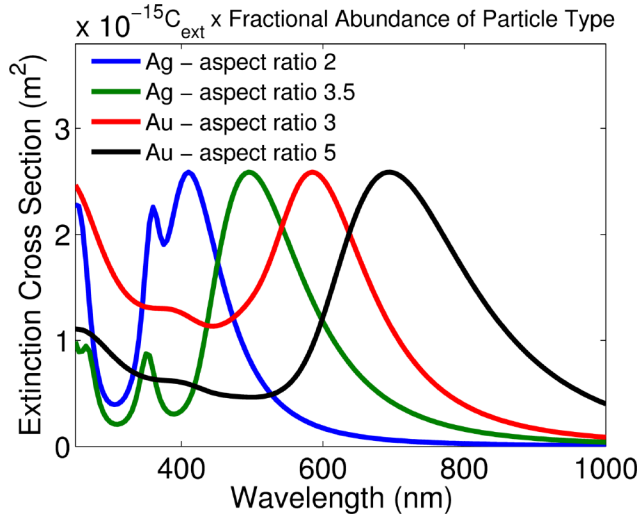

Figure 5.4 - LSP resonant extinction coefficients weighted by fractional abundance of each type of nanorod (38.20%, 11.32%, 40.23%, and 10.25%).

Elliptical nanorod shape is assumed above for ease of calculation using analytical expressions, though the same optical design process can be applied to metal rods of other shapes (e.g. cylinders) by numerically simulating extinction properties as described in Chapter 4. Extinction by cylindrical metal rods (Ag - 30 × 40 nm, Ag - 30 × 55 nm, Au - 30 × 55 nm, Au - 30 × 90 nm) are simulated at 40° incidence, resulting in the extinction cross sections of Figure 5.5(a). Extinction is balanced analytically using fractional abundances of 30.14%, 15.70%, 44.51%, and 9.65% respectively (Figure 5.5(b)). The aspect ratios chosen for the cylindrical case are smaller than those for the elliptical case due to additional redshifts associated with the change in shape (see Chapter 4), and no inhomogenous broadening is included to reduce the number of numerical simulations, though such broadening would increase extinction overlap and improve uniform extinction of the full visible range. Having verified that the idea behind our optical design can be realized with general anisotropic metal nanoparticle, we return to the analytical elliptical case to complete the analysis.

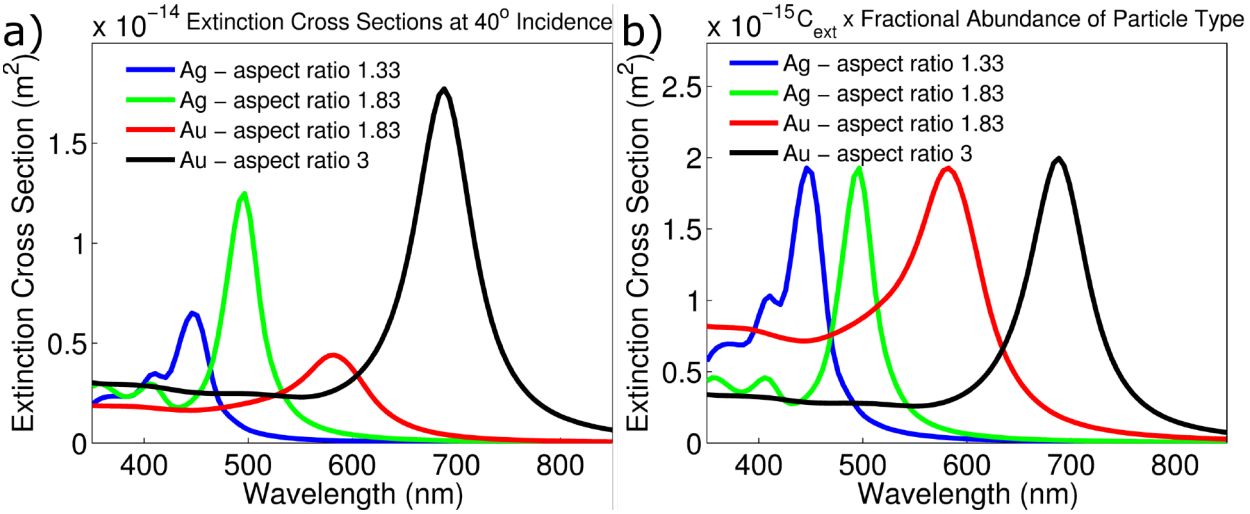

Figure 5.5 - (a) LSP resonant extinction cross sections for selected cylindrical nanorods across the visible spectrum at 40° incidence. (b) Analytically balanced extinction weighted by fractional abundance of each cylinder type (30.14%, 15.70%, 44.51%, and 9.65%).

At the balanced condition, found above, normalized transmission through the nanoparticle layer is calculated as:

$$\text{Transmission} = 1 - \frac{C_{ext}(\lambda)}{dx \cdot dx \cos(\theta)} \qquad 5.1$$

where dx is the average nanoparticle spacing and $dx\cos(\theta)$ is the effective nanoparticle spacing in the actuated direction, consistent with the definition of the extinction cross section[11] and experimental work in which extinction is measured via specular transmission[61, 64, 65]. Adjusting dx to realize full extinction of the visible spectrum at a 60º actuation angle (a value of 110 nm), the transmission spectra of Figure 5.6 are calculated.

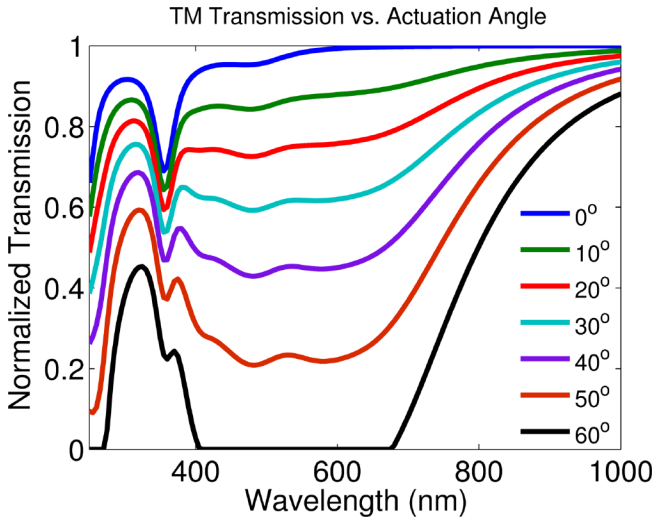

Figure 5.6 - Calculated transmission of TM polarized light through the nanoparticle layer at various actuation angles, assuming an average nanorod spacing of dx = 110 nm.

As seen in Figure 5.6, TM polarized visible light from 400 to 680 nm is modulated with actuation angle from 0 to 95+% transmission. Balancing the extinction peaks via the fractional weighting of each particle type at 40 degrees simultaneously balances the modulation of the full visible spectrum with angle, achieving approximately flat transmission spectra at the wavelengths of interest for all angles. Thus color viewed through the actuated structure will not be significantly distorted throughout the modulation range. Again, we note that the same optical

design process can be carried out using the resonant LSP extinction coefficients for other available metal nanorod materials and shapes, including moving to different spectral bands (near UV, IR, etc), so long as a sufficient number of aspect ratios / materials are available to cover the full wavelength range of interest.

To improve extinction at the red end of the spectrum, and account for some of the large spectral overlap between particle types in the 600 - 700 nm range, the fractional abundance of each particle type are slightly modified to the values shown in Table 6.1, realizing the weighted extinction coefficients and actuated transmission spectra found in Figure 5.7, now capable of modulating the visible spectrum from 400 - 725 nm.

Nanorod Material	Silver	Silver	Gold	Gold
Radius	15 +/- 5 nm	15 +/- 5 nm	15 +/- 5 nm	15 +/- 5 nm
Height	60 +/- 5 nm	105 +/- 5 nm	90 +/- 5 nm	150 +/- 5 nm
Nominal Aspect Ratio	2.0	3.5	3.0	5.0
LSP Resonant Peak	411 nm	495 nm	586 nm	693 nm
Fractional Abundance	.38	.12	.36	.14
Average Spacing (all rods)	110 nm			

Table 5.1 - Metal nanorod parameters for visible spectrum modulation, using elliptical nanoparticle calculations.

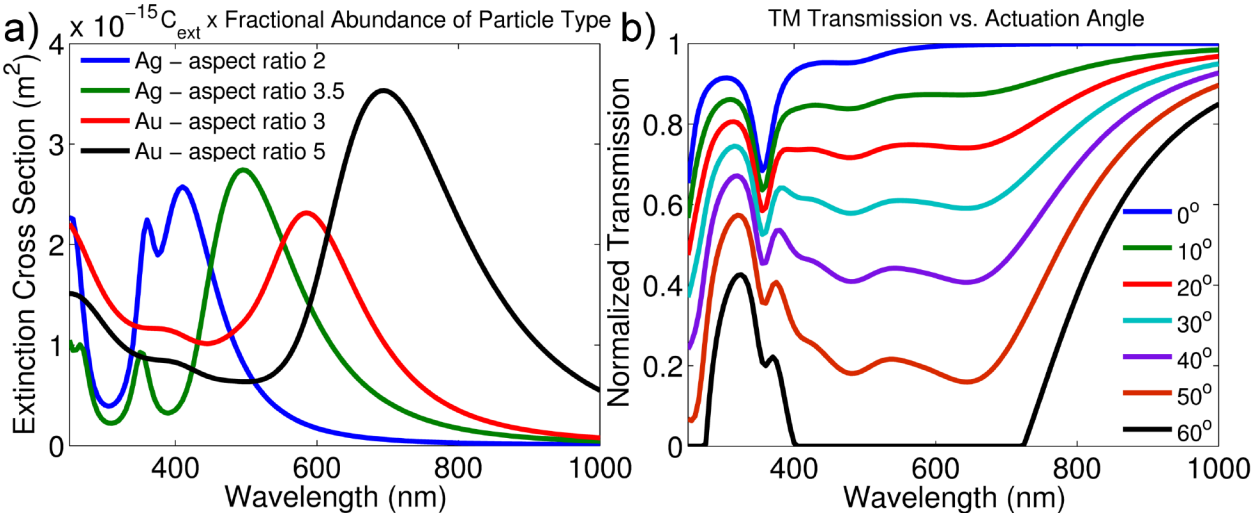

Figure 5.7 - (a) Extinction coefficients at 40° incidence weighted by adjusted fractional abundance of each type of nanorod (Table 5.1). (b) Calculated transmission spectra of TM light vs. actuation angle.

Management of Unpolarized Light

The main disadvantage of the structure described so far is that a single corrugated layer only realizes modulation of a single polarization of incident light, that which is TM polarized with respect to the angled plane of the nanoparticle layer (inset, Figure 5.1(b)). TE polarized light interacts with a short nanorod axis regardless of angle, favoring high transmission of visible wavelengths as shown in Figure 5.8 - only small modulations are seen with angle, in accordance with the change in effective nanoparticle spacing with angle (Equation 5.1).

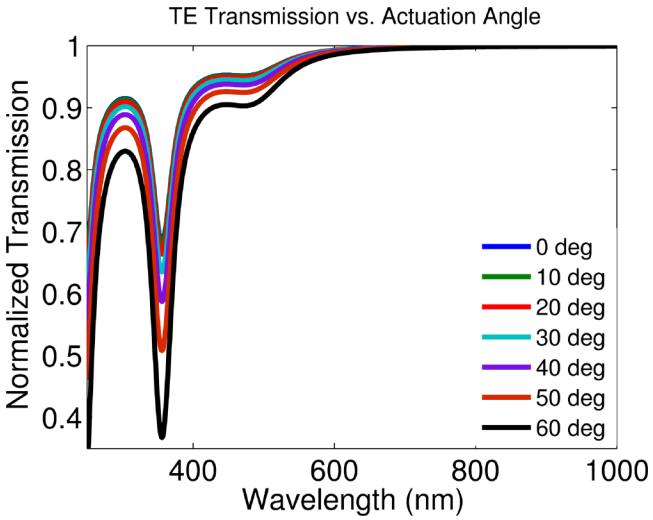

Figure 5.8 - Calculated transmission spectra for TE polarized light through a single actuating layer vs. angle.

Complete modulation of incident light requires a second, identical actuating layer placed behind the first (or, for example, on the opposite side of a glass pane / substrate) with corrugation axis rotated by 90 degrees, as diagrammed in Figure 5.9(a). The corresponding transmission spectrum (for unpolarized light) is shown in Figure 5.9(b). The second layer introduces greater transmission loss at normal incidence (blue curve) than the TM case above, particularly in the 400 - 500 nm range associated with extinction by the gold nanorods, though specular transmission remains above 90% on $\lambda > 420$ nm.

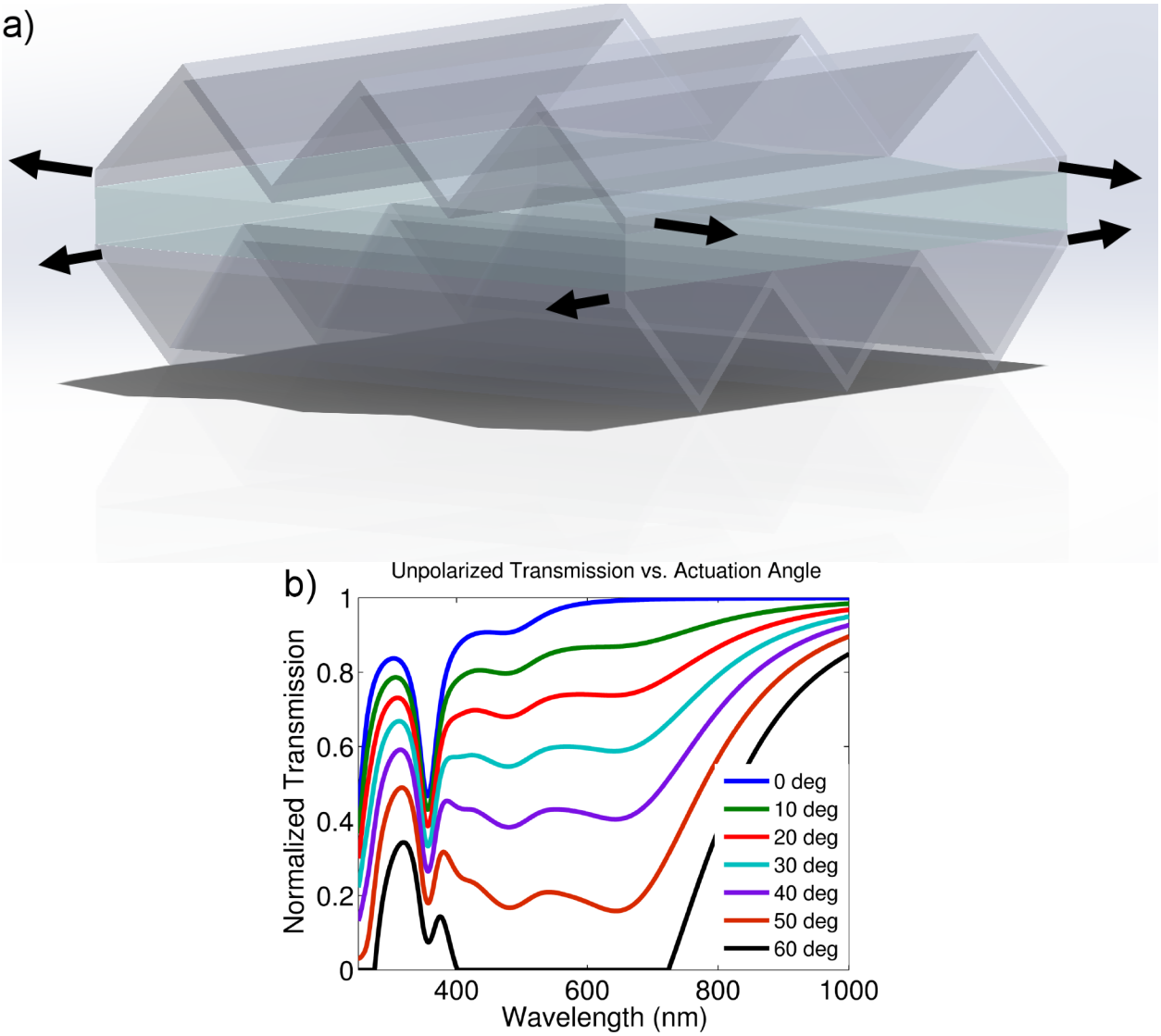

Figure 5.9 - (a) Orthogonally oriented actuating structures placed on either side of a window layer for management of both polarizations of incident light. (b) Transmission spectra as a function of actuation angle for double layer structure and unpolarized light.

As a demonstration of the variability of the proposed structure, red / green / blue (RGB) digital images are processed and re-colored according to how they would appear through the transmission spectra of Figure 5.9[93]. A digital photograph of North Campus at the University of Michigan and an image of the colors making up the visible spectrum are shown in Figure 5.10, assuming transmission through the optical structure at various actuation angles. Images and colors are preserved in the highly transmissive 0º state, with progressive darkening at increasing

angles. Color reproduction is essentially neutral (as the transmission spectra are flat) across all images.

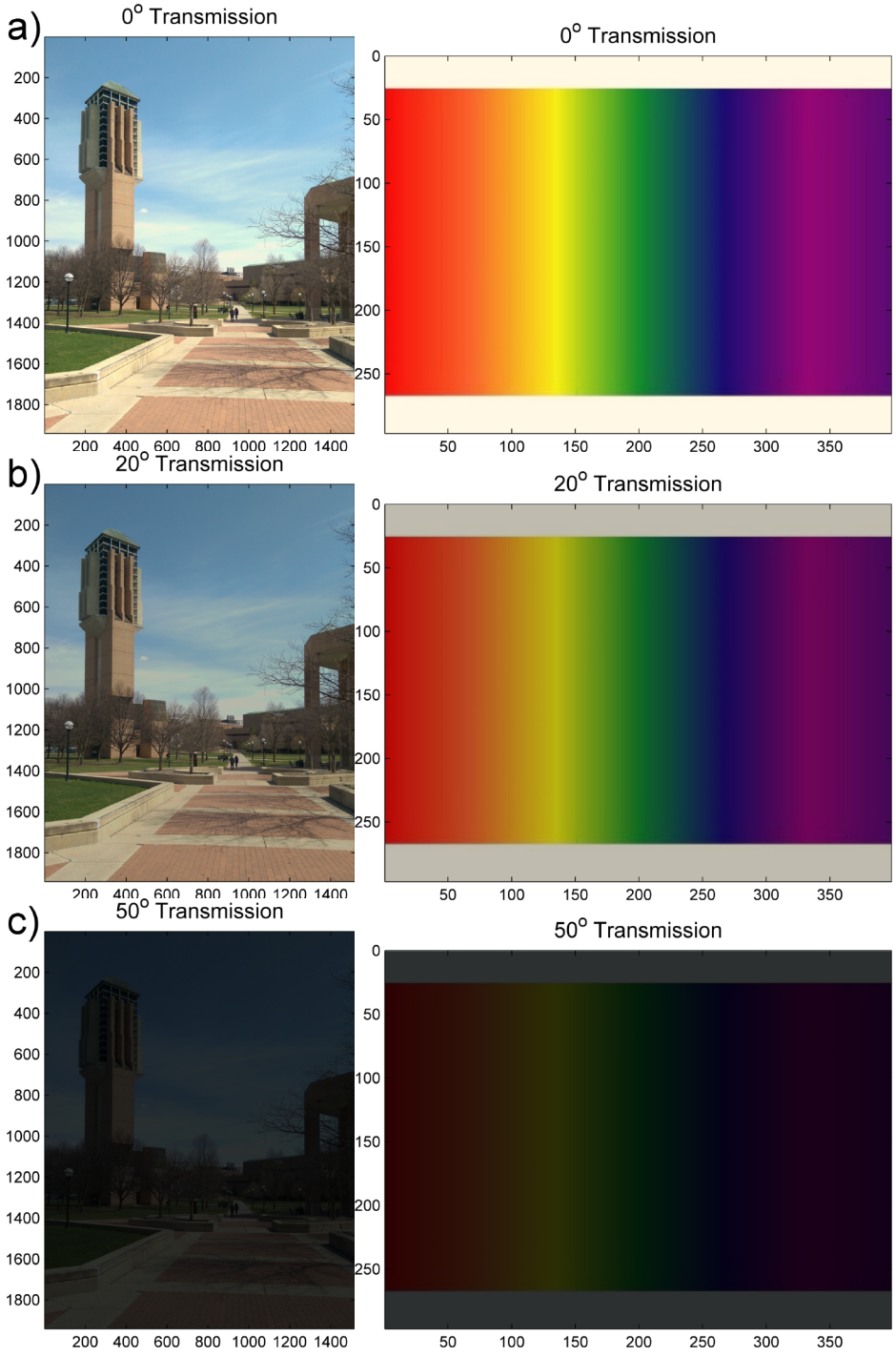

Figure 5.10 - (a) RGB images transformed via the transmission spectra of Figure 5.7 at (a) 0 degree (b) 20 degree and (c) 50 degree actuation. Note results for 60 degree actuation (not shown) are uniformly black.

The degree of image darkening across the range of actuation angles 0 - 60^o is calculated using the same method (assuming incident white light) and plotted in Figure 5.8. The resulting gray shades similarly demonstrate the color-neutral properties of the variable transmission system, with the exception of a slight yellow coloration at small angles of incidence due to absorption of ~10% of blue light by the gold rods. Qualitatively, we note that transmission appears to modulate faster with angle on $\theta > 40^o$ once the structure is near cut-off.

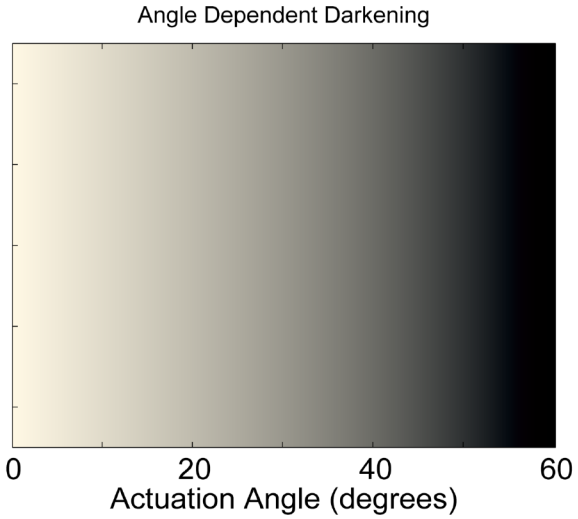

Figure 5.11 - Degree of transmitted image darkening vs. structure actuation angle, calculated assuming white input light.

Finally, for smart glass applications, we note that a window set to the transparent state should transmit images even if not viewed from perfectly normal incidence. The components of light making up an image to be transmitted occupy a range of angles, and thus will interact with the vertical nanorods at an angle, even when the actuating structure is at 0^o. A final set of images is calculated where the distance from the image center is correlated with an incident angle as diagrammed in Figure 5.12(a), resulting in the angular distribution or Figure 5.12(b) and the angle dependant darkening shown in Figures 5.12(c) and 5.12(d). Image transmission is preserved well up to approximately 20^o, though some darkening can be seen.

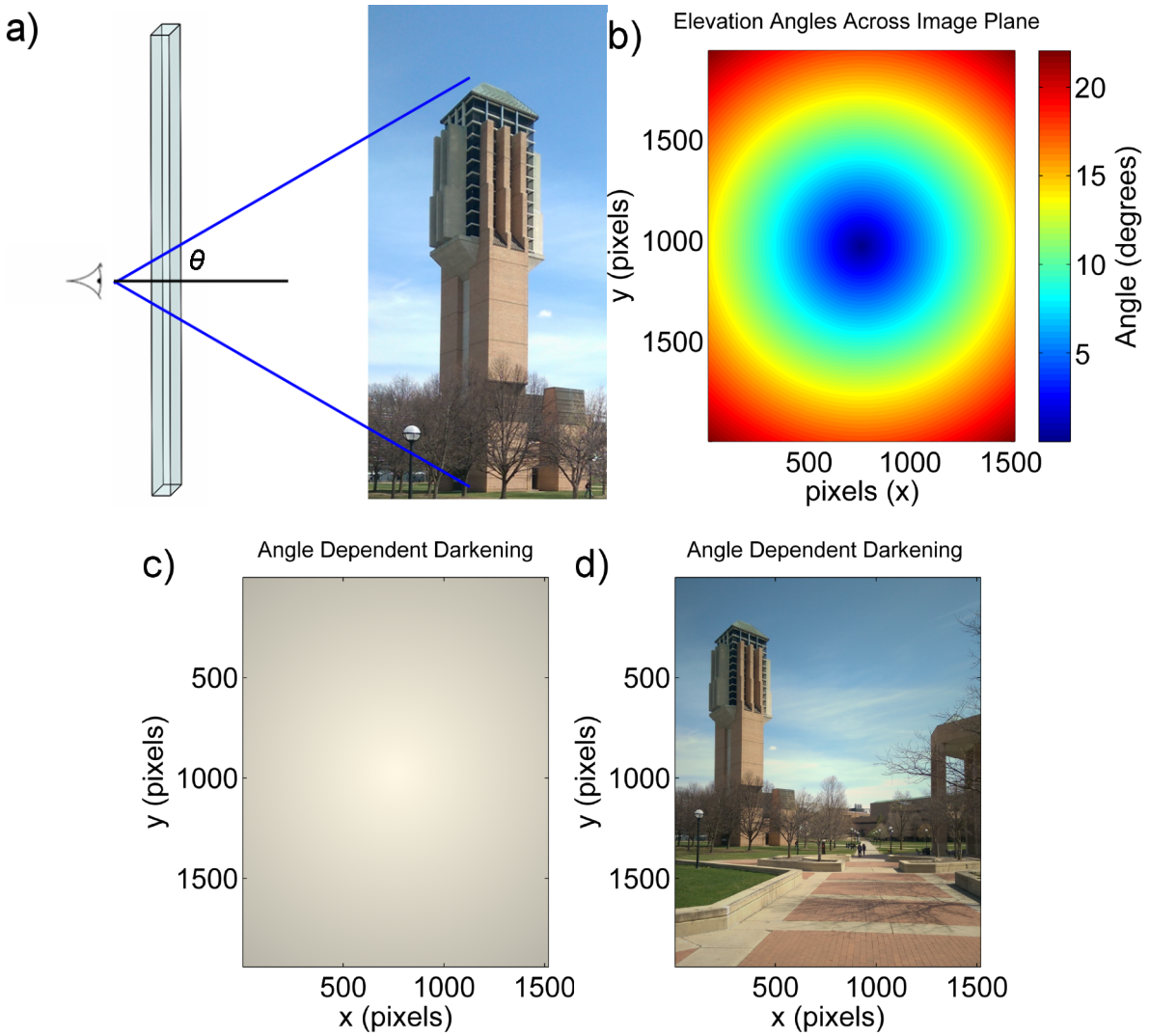

Figure 5.12 - (a) Incident angle of image components. (b) Elevation angle as a function of position for images (c) and (d). (c) Angle dependent darkening as a function of position across the image. (d) Image with angle dependent darkening.

Variable Transmission System: Advantages and Challenges

The proposed microstructure and corresponding optical model demonstrate a number of advantages of this approach as compared to other proposed technologies for variably transparent systems (electrochromics, liquid crystal technology, actuating MEMS micro-blinds, etc)[43-47, 92]. Visible transmission can be adjusted across the full range of 0 - 90+%, rather than exhibiting binary on vs. off states, and with proper balancing of nanorod materials and aspect ratios, the full visible spectrum can be modulated. The system can be redesigned for modulation of other

spectral regions as well via alternate metal nanorod selections. With proper mechanical design, the actuating system will draw no power at steady state - motors / other actuators will only need to be powered when the system actuation angle is actively being adjusted, unlike electrochromic or liquid crystal systems which require a constant quiescent voltage. No large area transparent electrode (e.g. ITO) is required for the structure (unless integrating a transparent conductive layer is required to realize nanorod patterning as detailed in Chapter 6). We also note that unlike the photovoltaics application of Chapter 4, the intrinsic absorption of metal nanorods is an advantage to this application rather than a source of losses.

Some challenges remain in realizing the structure described in this chapter. Our optical analysis to this point has considered only the influence of resonant plasmonic extinction on disrupting the transmission of visible light through the layers. Light which is not specularly transmitted is absorbed by metal particles (as C_{abs} is the dominant component of C_{ext} for these nanoparticle materials and sizes) or may be backscattered from the layer in accordance with Chapter 4 and other experimental work[61, 94]. Thus forward scattering (contributing to haze in the transmitted signal and reduction of the achievable cutoff / dark condition) is expected to remain low, though this has not yet been rigorously investigated. As an estimate of the significance of this effect, the transmission spectrum of Figure 5.9(b) is re-calculated assuming nanoparticle extinction from absorption cross sections only (a worst-case scenario that assumes all scattered light is in the forward direction), plotted in Figure 5.13. Visible transmission modulation is still achieved from at least 15 - 90% (6 - 95+% at longer wavelengths), as absorption is favored over scattering for silver and gold particles in this size regime. While we expect LSP resonance properties to be dominant in the proposed structure, additional corrections for light scattering off the corrugated structure may be needed as well. Additionally, our calculation of nanorod

extinction has considered only the anisotropic properties of the scattering particles alone - resonant coupling between adjacent rods may result in additional shifts in LSP resonance[11, 95] which must be accounted for to realize a balanced device. Finally, balanced modulation of the full visible spectrum as demonstrated here depends on fine control and balance of the population of metal nanorod materials and aspect ratios, a significant future fabrication challenge, though we note that arrays of different particle types could also be prepared in separate layers and stacked vertically rather than requiring multiple nanorod materials and sizes to be placed on the same plane.

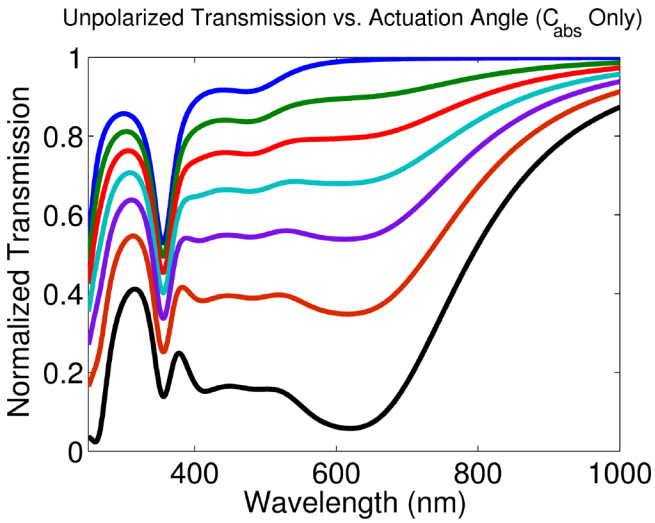

Figure 5.13 - Transmission of unpolarized light through the double layer structure considering plasmonic absorption only.

Other optical structures which demonstrate angle selective interaction with light (DBRs, photonic crystals) could also be placed on the actuating structure described above to modulate the transmission spectra, though such dielectric structures show a continuous shifting of their reflection vs. transmission properties with angle[72] rather than maintaining the well-defined LSP resonances of the metal approach, which would lead to significant color distortions with angle. Plasmonic absorption will also significantly decrease the amount of stray light in the system as compared to a dielectric structure with no intrinsic losses.

CHAPTER VI

Metal Nanorods: Fabrication Strategies and Challenges

Having established the potential for metal nanorods to realize angle selective light management via electromagnetic theory, we now turn to strategies for nanofabricating these structures. For the applications of interest, our fabrication strategy needs to meet a number of requirements. Nanofabrication methods should be inexpensive, scalable to large areas, capable of realizing moderate to high aspect ratios, and enable small feature sizes (size $<< \lambda$ for plasmonics). These requirements are a challenge for traditional nanofabrication techniques: photolithography systems cannot produce extremely small (~10s of nm) features without significant expense, e-beam lithography patterning cannot create large area patterns, and aspect ratio requirements tend to be a challenge across all areas of planar nanotechnology. For these reasons, we investigate patterning with anodized aluminum oxide.

Anodized Aluminum Oxide

Anodized aluminum oxide (AAO) nanopatterning refers to the electrochemical oxidation of the surface of aluminum into self-assembled nanoporous aluminum oxide (Al_2O_3) structures[96-115]. Nanopores in the layer are aligned in parallel and can be grown to extremely high aspect ratios (aspect ratios of 10 - 200 are common). Nanopore sizes and spacing can be controlled via growth conditions in the 10's - 100's of nm range[96-100] (appropriate for sub-λ plasmonics), and highly periodic structures with hexagonal lattice patterns can be grown under

optimized conditions[96, 87, 101-103]. Pseudo-periodic AAO lattices in two size regimes and a cross sectional view of AAO on an Al film are shown in Figure 6.1 (highly periodic AAO grown in our lab is shown below in Figure 6.6). Finally, we note that Al_2O_3 is a visibly transparent material with low refractive index (n ~ 1.65) which will not introduce optical losses and limit the redshift of plasmonic properties of accompanying metal nanoparticles.

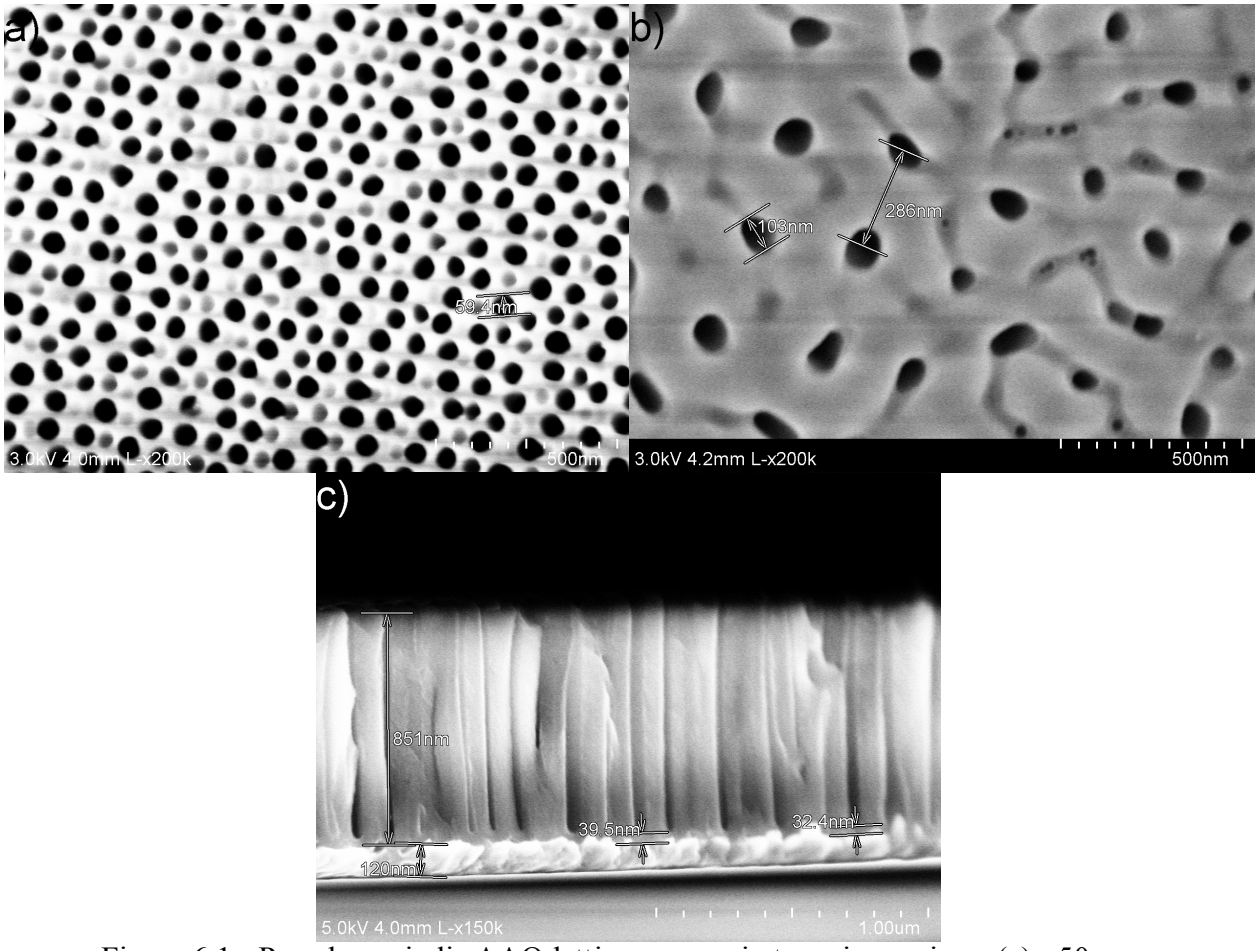

Figure 6.1 - Pseudo-periodic AAO lattices grown in two size regimes (a) ~50 nm pores, ~100 nm pore spacing (b) ~100 nm pores, ~300 nm pore spacing. (c) Cross secional view of AAO nanopores on a thin Al layer, including the presence of barriers at the bottom of the pores.

As an electrochemical process, AAO growth can be carried out in any wet chemistry lab setting with the resources for safely handling acids and oxidizers. The AAO growth apparatus itself consists of a 250 mL Pyrex beaker containing an acid electrolyte and a magnetic stir bar, a

closed-loop chilled water circulation vessel and water chiller that provides electrolyte temperature control, one or more DC power supplies capable of constant voltage (potentiostatic) or constant current (galvanostatic) operation, and sufficient lab bench hardware to position an aluminum sample to be anodized and a graphite counter electrode in parallel, lower them into the electrolyte, and connect them to the DC supply with the Al sample as the anode. A computer monitored voltmeter or ammeter are optionally added to the system to record anodizing I / V as a function of time. A system diagram and photograph of the anodizing vessel are shown in Figure 6.2.

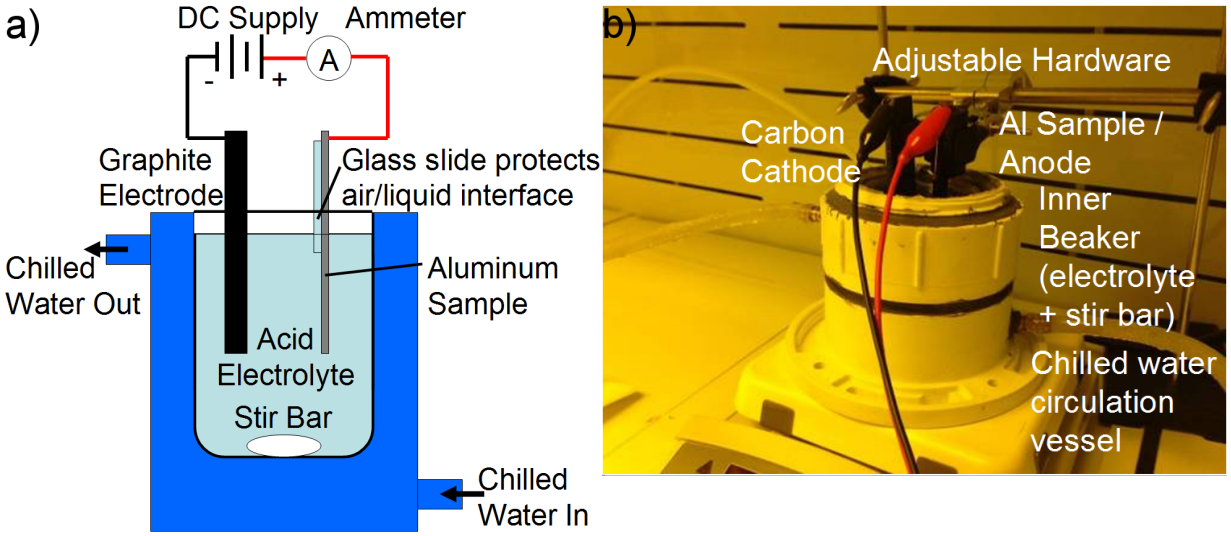

Figure 6.2 - (a) Diagram of anodizing apparatus. (b) Photograph of anodization vessel.

Anodized Aluminum Oxide - Growth Mechanism

To exploit this nanopatterning technique for our application, it is worth developing an understanding of the mechanism by which AAO lattices form and the limits and challenges involved in this process.

The most commonly accepted explanation for nanopore self-assembly is the field enhanced oxide dissolution model[96, 97], as diagrammed below in Figure 6.3, which spatially

describes the procedure of the chemical conversion of Al to Al_2O_3. The net chemical reaction describing this process is[97]:

$$2Al + 3H_2O \Rightarrow Al_2O_3 + 3H_2 \quad (6.1)$$

At the onset of anodization, a thin, uniform oxide barrier forms on the surface of the Al sample (Figure 6.3(a)) via dissolution of Al into Al^{3+} ions:

$$Al \Rightarrow Al^{3+} + 3e^- \quad (6.2)$$

and formation of aluminum oxide at the metal surface via:

$$2Al + 3O_2^- \Rightarrow Al2O3 + 6e^- \quad (6.3)$$

Al^{3+} ions that diffuse up through the oxide layer can also contribute to Al_2O_3 formation at the top surface via:

$$2Al^{3+} + 3H_2O \Rightarrow Al_2O_3 + 6H^+ \quad (6.4)$$

As the layer gets thicker and begins to become nonuniform, the electric field profile across the insulating oxide layer becomes nonuniform as well - the E-field focuses on the thinner oxide regions (Figure 6.3(b)). Enhancement of the E-field, along with a low pH acid electrolyte tends to favor dissolution of the barrier oxide and liberation of Al^{3+} ions to the electolyte rather than allowing the reaction of Equation 6.4[97]. Thus the thin regions get thinner, allowing increased ion transport across the barrier and further conversion of Al to Al_2O_3 at the metal surface - in this way, pores nucleate and being to dig into the underlying Al surface (Figure 6.3(c)). Eventually, a steady state growth is reached when ion transport across the oxide barrier layers and field enhanced oxide dissolution are balanced (Figure 6.3(d))[97]. The porous structure continues to grow downward into the underlying aluminum toward indefinite Al_2O_3 structure height and aspect ratio.

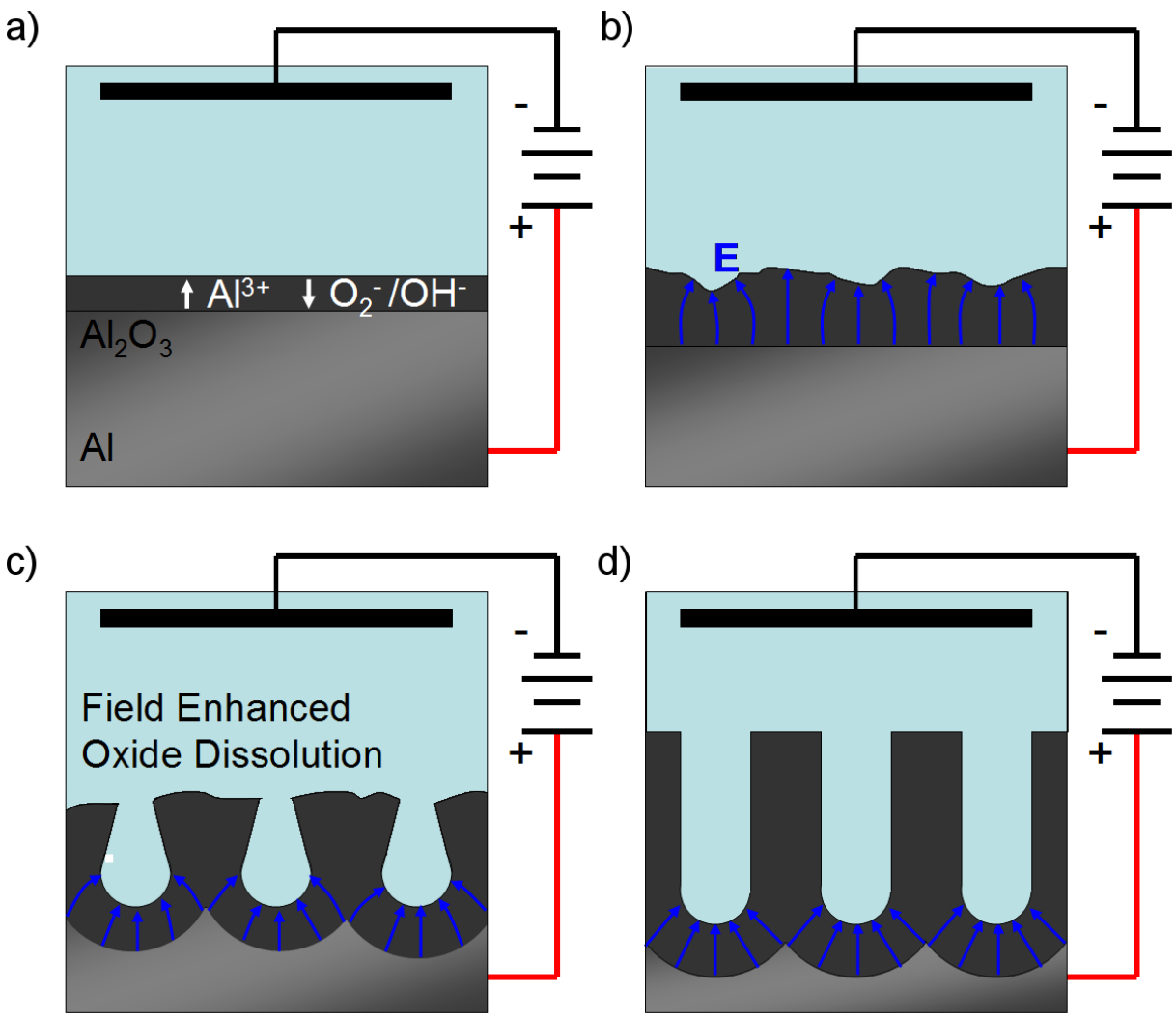

Figure 6.3 - (a) Barrrier oxide formation and ion transport processes. (b) Nonuniform oxide thickness causes E-field focusing. (c) Field enhanced oxide dissolution thins the oxide in certain regions, nucleating nanopores. (d) Steady state AAO growth.

For completeness, the final chemical sub-reaction in the electrochemical cell is the evolution of hydrogen gas at the cathode:

$$2H^+ + 2e^- \Rightarrow H_2 \qquad 6.5$$

plus the equilibrium between H_2O, OH^- and H^+ found in any aqueous system:

$$H_2O \Leftrightarrow H^+ + OH^- \qquad 6.6$$

There is a significant body of literature further exploring this electrochemical process[97], the discussion of which is beyond the scope of this thesis. From a practical standpoint, though,

we note a few key features of this process. First, any nanoporous AAO growth includes oxide barriers at the bottom of the nanopores, which will need to be removed if an idealized high aspect ratio through-hole nanopore structure is needed[103-106]. Second, geometrical feature sizes in AAO growth depend on the magnitude and focusing on the electric field - changing the anodization voltage allows tuning the AAO lattice size[96-100, 110-1114] (as shown in Figure 6.1). The most common voltage regimes for anodization and the resulting interpore lattice spacings are shown in Figure 6.4[96] - AAO lattice spacing increases with voltage at a rate of approximately 2.5 nm per volt. Finally, the size of the nanopores themselves depends on the field enhanced oxide dissolution rate, a function of pH[96-100]. Not considered in the discussion of electrochemistry above is the balancing of physical stress and volume expansion associated with conversion of Al to Al_2O_3[107] - this aspect of the growth mechanism explains why a hexagonal lattice is favored in the ideal case, and determines the choice of growth electrolytes in the various anodization regimes of Figure 6.4 - pore size (again, a function of pH) and lattice spacing (a function of applied voltage) should be balanced for the best self-assembly[107].

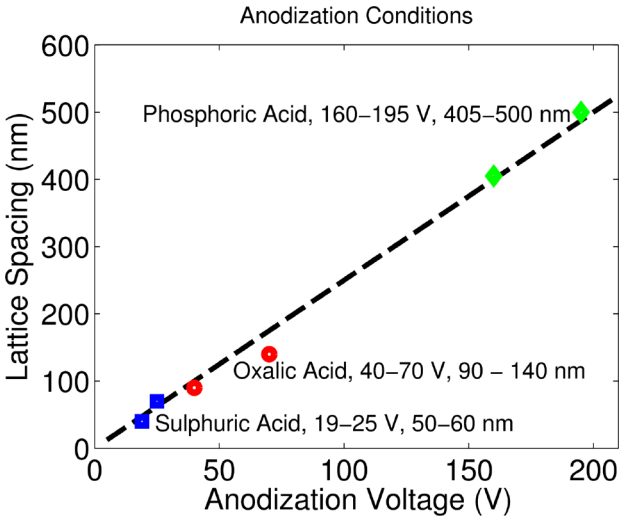

Figure 6.4 - Typical anodization voltages and electrolyte selections from literature vs. lattice spacing of AAO films[96].

Finally, we note without further discussion that active research continues into AAO growth with more uncommon electrolytes and growth conditions to expand the range of sizes at which self-assembled porous AAO templates can be grown[97, 110-114].

Anodized Aluminum Oxide - Growth Steps and Challenges

The most interesting and impressive feature of self-assembled AAO patterning is the ability to fabricate ordered hexagonal lattices. Ordered structures can be realized practically using a two step growth process first reported by Masuda and Fukuda in 1995[101], detailed here (and diagrammed in Figure 6.5), including the exact process we used to duplicate these results, shown in SEM images in Figure 6.6.

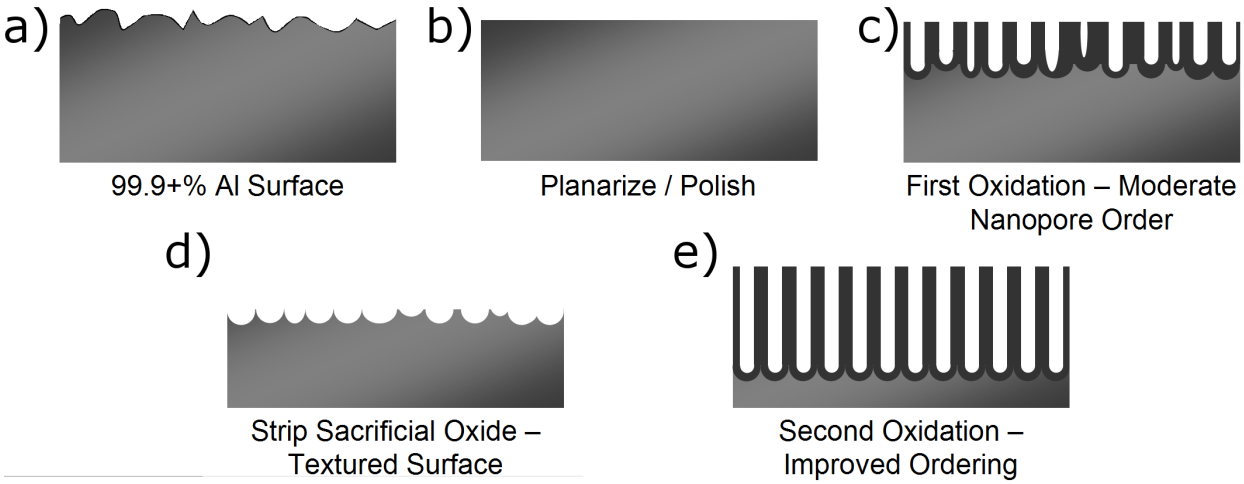

Figure 6.5 - Diagram of two step anodization process for highly ordered AAO

A 99.9+% aluminum foil sample (Alfa Aesar) of .25 to 1 mm thickness is used as the AAO growth medium. To prepare a high quality surface for anodizing, the sample is annealed in air at 400° C for one hour, then the native oxide layer is removed in 1:1 concentrated (85%) phosphoric acid / DI water at 60° C for 1 minute, leaving only a bulk aluminum surface (Figure 6.5(a) / 6.6(a)). The surface is then electropolished in a mixture of 1:4 perchloric acid / ethanol at 20 V for 3 minutes at 7° C[108, 109] using the same apparatus described for anodizing above - this

process attacks small aluminum features on the surface, resulting in a mirror finish and nm quality smoothness (Figure 6.5(b) / 6.6(b)). The sample is then anodized in 3 wt% oxalic acid at a constant voltage of 40 V for 90 minutes at a temperature of 5 - 10^{o} C. During this first anodization, pseudo-periodic porous AAO is grown (Figure 6.5(c) / 6.6(c)).

To improve the periodic ordering of the AAO layer, the first oxide layer is stripped off in 1:1 phosphoric / DI water at 60^{o} C, leaving a textured surface (Figure 6.5(d) / 6.6(d)). The texturing on the surface helps to improve the nucleation of the nanopores during the next step, a second anodization under the same conditions for 20 minutes (which can be varied to realize the desired AAO pattern thickness). The resulting structure shows significantly improved uniformity and hexagonal ordering (Figure 6.5(e) / 6.6(e)) with 30 nm pore sizes and 100 nm pore spacing.

Analogous processes have been reported to realize ordered AAO templates in other size regimes by changing the choice of anodizing electrolyte and voltage in accordance with Figure 6.4[97, 110-114].

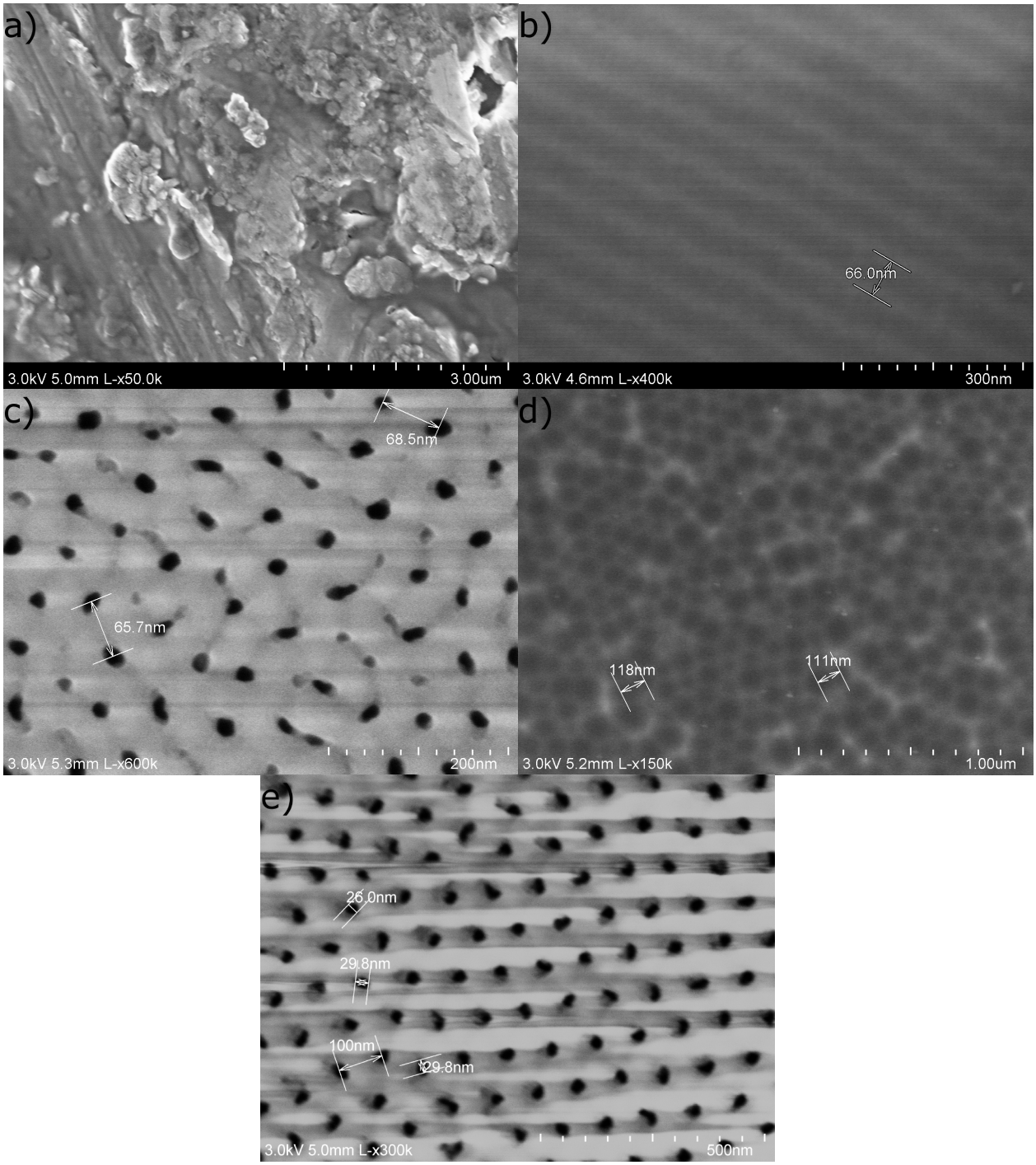

Figure 6.6 - SEM images showing growth steps for highly ordered AAO. (a) Annealed Al foil. (b) Electropolished surface. (c) Pseudo-ordered AAO after first anodization. (d) Textured aluminum surface after removal of sacrificial AAO layer. (e) Highly periodic AAO grown by second anodization.

A number of practical challenges came to light while realizing the results above. First, one must be careful of material interfaces at the anode - junctions between dissimilar conductive

materials leave the aluminum layer susceptible to galvanic corrosion[116] in the presence of the electrolyte, which proceeds particularly quickly under an applied anodizing voltage. Figure 6.7(a) shows corrosion at the interface between an Al sample and the stainless steel clip used to hold it in place and connect to the DC power supply - keeping the clip far from the electrolyte avoids this problem (Figure 6.7(b)).

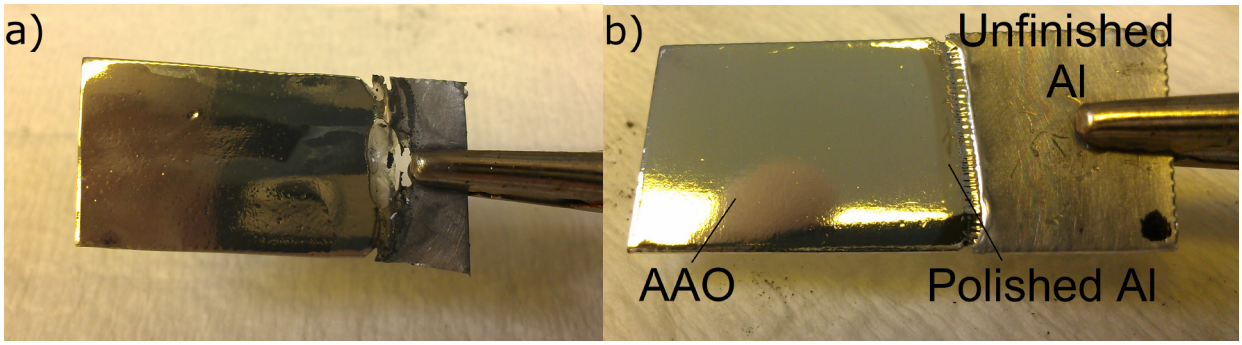

Figure 6.7 - (a) Corrosion of aluminum sample when Al / stainless steel clip interface is exposed to electrolyte and voltage. (b) Improved sample without corrosion, showing AAO film (hazy region) on polished Al (shiny region).

Beyond electrical contact to the sample, though, corrosion issues also limit the materials that can be integrated with Al / AAO patterning, as will be detailed in the next section.

Another practical issue is found when attempting anodization in the high voltage / large lattice size regime with phosphoric acid as an electrolyte. The same focusing of the electric field on small surface imperfections that is responsible for pore nucleation can, in the high voltage case, cause dielectric breakdown of the oxide film on the surface, resulting in rapidly increasing current, sparking at the anode, local heating, and burning of the sample[110-114], as shown in Figure 6.8.

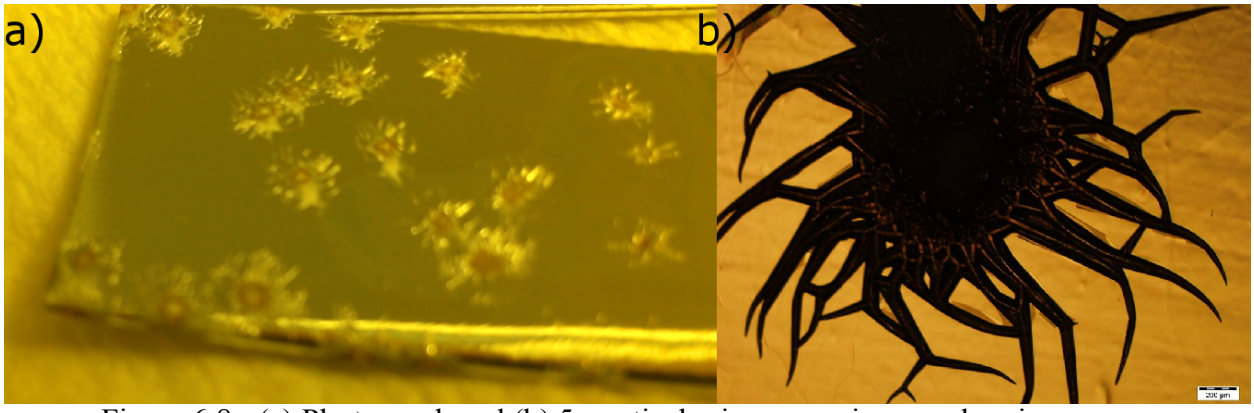

Figure 6.8 - (a) Photograph and (b) 5× optical microscope images showing breakdown / burning spots on aluminum sample under high voltage anodization conditions.

Limiting of burning has been reported by significantly decreasing the electrolyte temperature[112-114], adding ethanol to the electrolyte (both to allow chilling the liquid below 0° C and to provide local cooling to the sample via ethanol evaporation), and adding other chemicals to slow down the reaction process[110, 111]. In this work, however, we found that the only reliable way to avoid burning at high voltages was to improve the smoothness of the initial aluminum surface by using e-beam evaporated aluminum on polished glass rather than aluminum foil samples. This process is detailed in the next section.

Both corrosion and breakdown / burning processes can be monitored during the anodization process by observing the anodization current as a function of time - rapid increase in current indicates a failure of the anodization process and the onset of unwanted electrochemical reactions. A successful anodization can also be monitored via the current / time curve (or voltage / time curve in the case of a constant current process), examples of which will be shown in the next sections.

AAO Patterning of Metal Nanorods on Transparent Substrates

Having developed an understanding of the anodized aluminum oxide material system, we now turn to the ways in which AAO can be used to realize the plasmonic structures of interest - self-assembled arrays of vertical metal nanorods on transparent materials.

Rather than anodizing highly pure Al foil samples (which are not transparent), thin mirror quality aluminum layers are deposited onto transparent materials (glass slides, ITO glass, etc.) via e-beam evaporation. Typical aluminum layer thicknesses are in the range of 250 nm to 1.5 μm. By anodizing through the full thickness of the aluminum layer (converting it to Al_2O_3), anodization current drops to zero as shown in Figure 6.9(a) and samples return to transparency (Figure 6.9(b)). For completeness, the important steps of AAO growth that are reflected in the current / time curve of Figure 6.9(a) are labeled. Additionally, AAO on glass can be lifted off / transferred via adhesive tape (Figure 6.10(a)) and AAO can be grown on flexible transparent layers such as polyethylene terephthalate (PET) plastic if a thin (~5 nm) titanium adhesion layer is evaporated onto the plastic before the aluminum (Figure 6.10(b)).

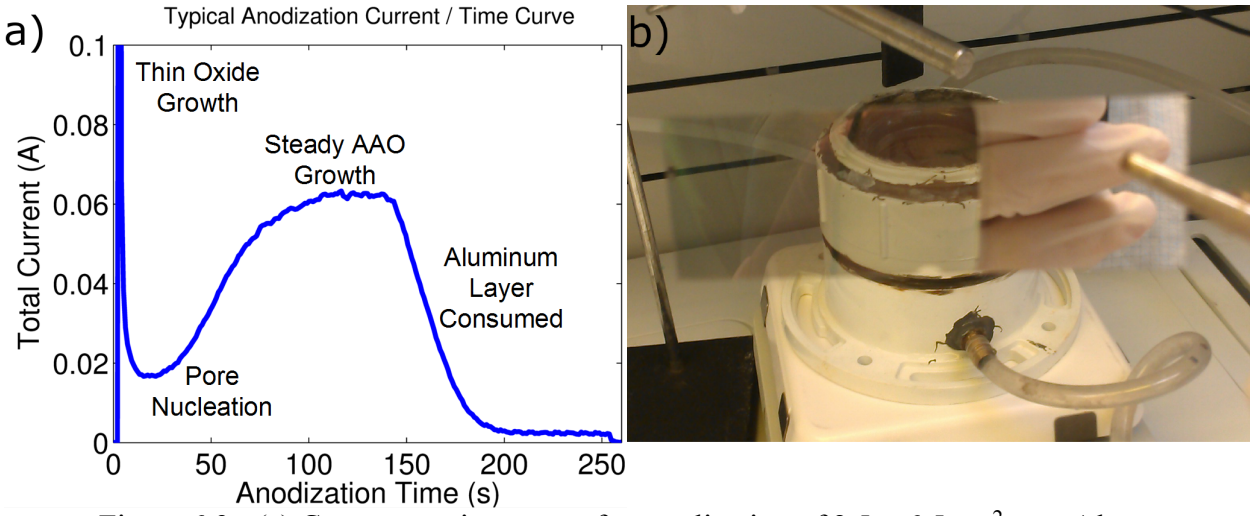

Figure 6.9 - (a) Current vs. time curve for anodization of 2.5 × 6.5 cm^2 area Al on glass at 60 V in 3 wt% oxalic acid. (b) AAO on glass slide, anodized until transparency. Some of the sample (right) is not anodized and remains reflective.

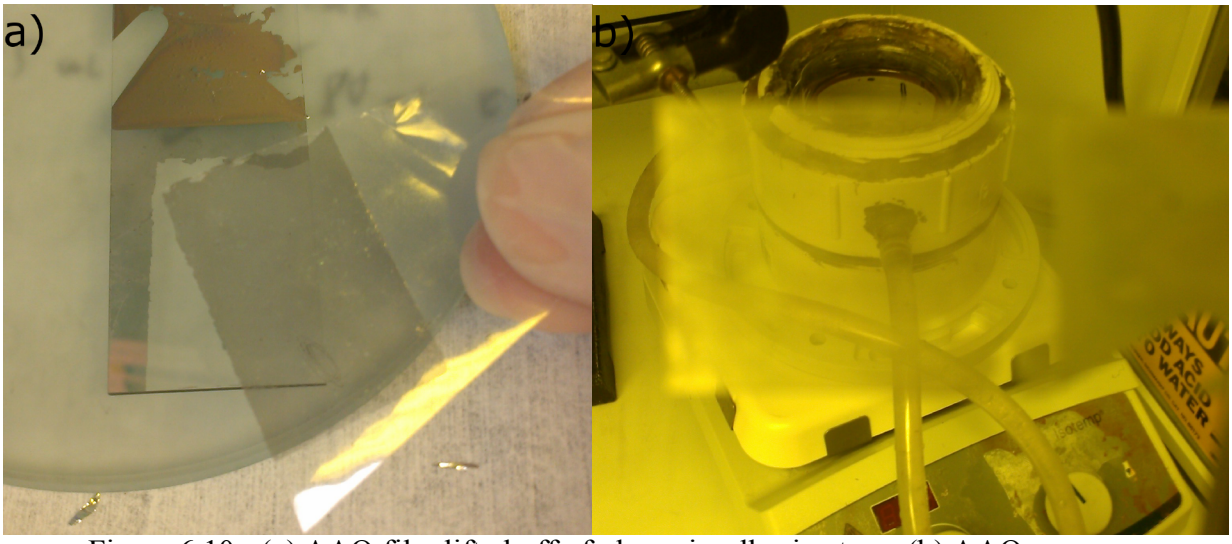

Figure 6.10 - (a) AAO film lifted off of glass via adhesive tape. (b) AAO grown on flexible PET plastic.

We note that large area thin film vacuum deposition is a mature technology in the glass industy (for display applications, for example) and continued research into the scalability of AAO growth has demonstrated though-layer anodization for significantly larger glass sample areas than considered in our work[115].

Using AAO nanopores on transparent substrates, two strategies can be considered to realize metal nanorods. First, a bottom-up approach (Figure 6.11(a)): AAO grown on a transparent conductive substrate is used as the cathode in a metal electroplating bath. Metal ions in solution can only plate at the conductive area at the bottom of the pores, resulting in metal nanorods in an AAO scaffold. A number of studies have used this approach to pattern self-assembled metal rods on various substrates, including transparent ITO[104, 105]. Critical to the success of this approach is the removal of barrier layers at the bottoms of the nanopores.

Second, one could consider a top-down approach (Figure 6.11(b)) by which metal is evaporated into the porous structure from the top. However, vacuum deposition cannot realize high aspect ratios (Figure 6.11(c)), and any metal deposited on the top of the AAO pattern would

need to be removed, a potentially challenging liftoff process. Thus we will first consider the bottom-up fabrication process.

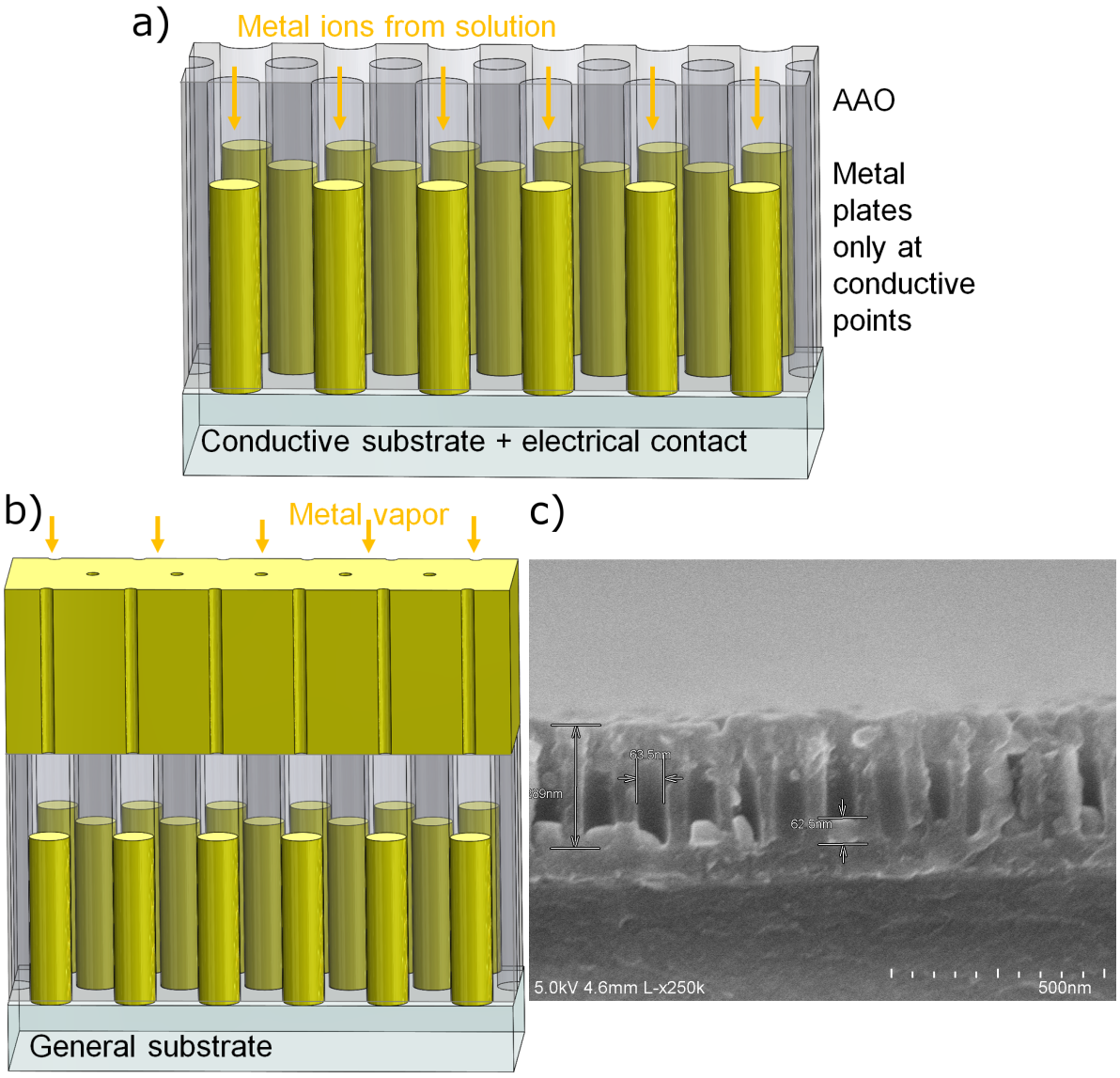

Figure 6.11 - (a) Bottom-up electroplating of metal rods. (b) Top-down evaporation of metal. (c) SEM cross section showing aluminum evaporated into an AAO template - this approach is unable to realize aspect ratios > 1.

Bottom-Up Electroplating of Metal Rods

The first important issue that must be considered when preparing an AAO template to serve as a mask for electroplating is the removal of barriers at the bottom of the pores to expose

the underlying conductive material. Barrier morphology is an important consideration for this application, and can be studied by imaging SEM cross sections of AAO grown on various materials.

While growing through an aluminum layer, barriers are U-shaped, as seen in Figures 6.1(c) and 6.3. When the full aluminum layer is consumed and growth terminates at another material, two barrier shapes are seen. First, terminating growth on an insulating layer (e.g. glass) or on an oxidizing material (such as a thin titanium adhesion layer), barriers tend to become squared-off as seen in Figure 6.12(a). In the case of an underlying insulator, the barrier material is aluminum oxide, and removing the barrier by isotropic wet etch in phosphoric acid will also result in significant attack of the rest of the AAO structure, widening the pores considerably[103-105]. In the case of an oxidizing material, the barriers may contain a mix of aluminum oxide and other oxide species that diffuse upward. This material change can make it possible to wet etch the barriers selectively to etching of AAO sidewalls - titanium oxide containing barriers, for example, appear more susceptible to phosphoric acid etch than aluminum oxide, minimizing the amount of pore widening that occurs during barrier removal (though phosphoric acid attack of the titanium adhesion layer makes it possible for the entire AAO film to become detached).

When AAO is grown on a non-oxidizing conductive material (such as gold), barrier morphology is significantly different[105, 106]. Barriers form as thin shells with void space below. Barriers can be removed more easily by isotropic wet etch as they are considerably thinner than the rest of the aluminum oxide layers in the structure.

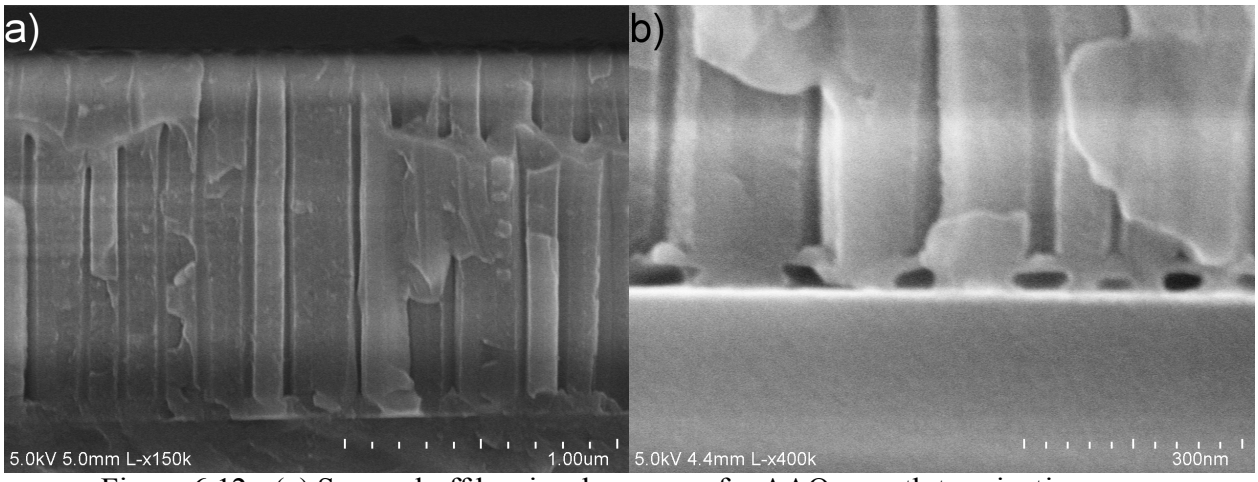

Figure 6.12 - (a) Squared off barrier shape seen for AAO growth terminating on glass or glass with a thin titanium coating. (b) Thin shell barriers seen for AAO growth terminating on a non-oxidizing conductor, here a thin (8 nm) gold layer.

For selective barrier removal, a change in barrier material and / or significant barrier thinning are desired, and can be engineered by choosing the layer stack beneath the anodized aluminum.

The second significant issue to be considered for AAO growth on a conductive substrate is the stability of the anodization process. Previously, we suggested avoiding any conductive material interfaces at the anode, as galvanic corrosion tends to proceed rapidly under anodization conditions. Indeed, attempts to anodize aluminum on top of transparent conductive ITO show corrosion and film delamination almost immediately. Thin e-beam evaporated gold films are an alternative choice of conductive backplane, as they remain semitransparent at thicknesses < 10 nm (as used in the PV stack of Chapter 3), though the gold / aluminum interface is also unstable during anodization - to limit the corrosion process, anodization current is limited to approximately the steady state pore growth value when AAO is grown directly on 8 nm gold.

Finally, we must consider how well the electroplating process proceeds on the sample. Samples on 2.5 × 7.5 cm glass slides (Fisher Scientific) were prepared with 8 nm gold (and a 3 nm chrome adhesion layer) as a semitransparent conductive backplane, then coated in 750 nm

aluminum. The aluminum was anodized through to form AAO, and the pore bottom barriers (Figure 6.12(b)) were removed with an isotropic wet etch in 5 wt% phosphoric acid at 50^{o} C for 1 - 2 minutes (this etch also slightly widened the nanopores). Copper rods were electroplated into the nanopores in a commercial plating solution (Microfab) with a copper foil anode using pulsed current deposition of current density 1 mA / cm^2 and a pulse train of 15 ms on / 5 ms off. The resulting sample is cleaved and imaged by SEM in Figure 6.13.

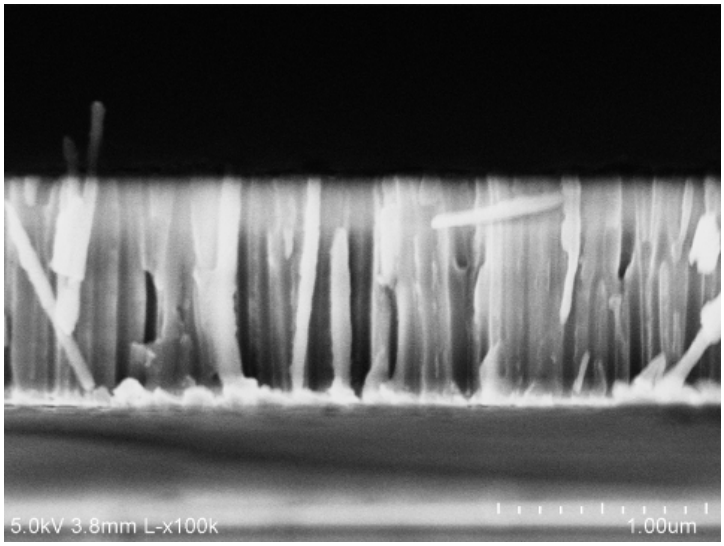

Figure 6.13 - Copper nanorods electroplated into AAO template with thin gold backplane.

Copper rods were achieved, though not all nanopores showed rod growth, and sample uniformity was poor. We believe the thin gold layer was not a sufficiently reliable conductor for the electroplating process, especially after being exposed to the anodization process which tends to cause delamination of the gold film (unless current is limited during anodization). Additionally, the visible transparency of 8 nm gold is on the order of 70%, significantly lower than we would like for window layer applications.

ITO is the other primary choice for a conductive backplane, providing higher transparency than gold (~90%) and good conductivity (~15 ohm / square), though it is also very unstable during the anodization process. Successful AAO growth on ITO is possible, however, if

a thin layer of tungsten is included between the two materials[104-106]. Tungsten anodizes very slowly (into tungsten oxide, WO_3), and is capable of protecting the underlying ITO film from the anodization process until all the aluminum has been consumed.

Commercial ITO of conductivity 15 ohm / square (Delta Technologies) was coated in 5 nm titanium (as an adhesion layer) and 5 nm tungsten using a DC sputtering system (Kurt J. Lesker Lab-18). 500 nm of aluminum were e-beam evaporated on top of the W layer (as evaporated aluminum was found to be higher quality than sputtered Al from the same tool), and the sample was anodized at 40 V in 3 wt% oxalic acid at 5° C. The current vs. time curve for the anodization is shown in Figure 6.14(a), and resembles that of an ideal anodization, showing the generation of barrier oxide at the onset of growth (rapid drop in current), pore nucleation (slow current rise), steady AAO growth (steady current), then a drop in current as the aluminum is all consumed. A few current spikes occur, associated with localized exposure and attack of the underlying ITO film, but most of the sample survives the process (Figure 6.14(b)). Current drops to a low saturation value at the end of the process, associated with slow conversion of the tungsten layer to WO_3.

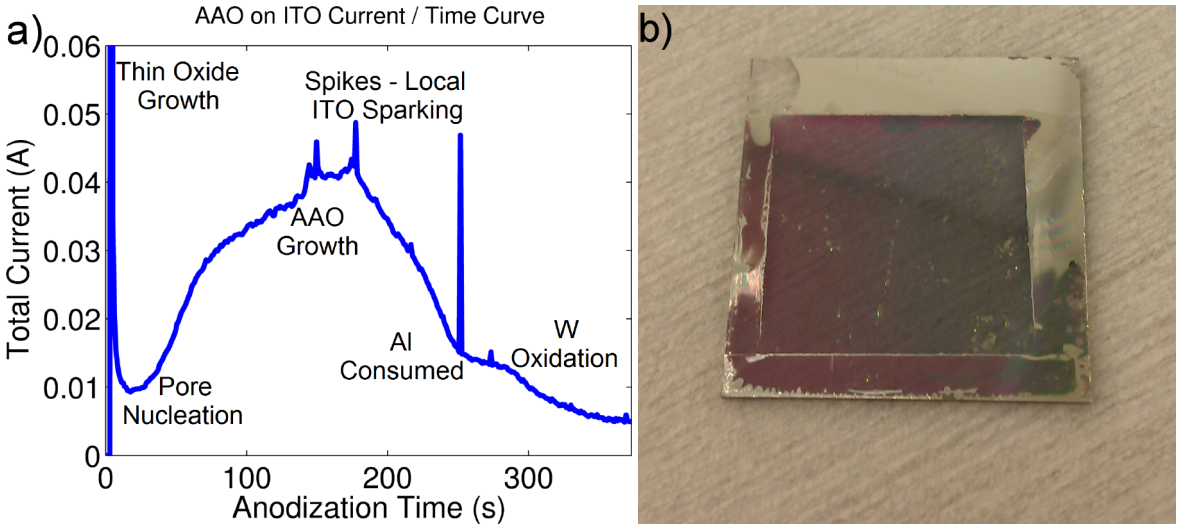

Figure 6.14 - (a) Current vs. time curve for anodization of Al on ITO with a W protective layer. (b) ITO with AAO in the middle region

Of particular interest, the barriers formed at the bottom of the AAO pores in this case are thin shells containing WO_3, which can be selectively wet etched using a neutral pH buffer etch without attacking any of the other materials on the sample[105]. This etching behavior can be derived by considering the dissolution reactions of Al_2O_3 and WO_3 and their equilibrium concentrations in aqueous systems as a function of pH[105, 117].

Aluminum oxide can dissolve into aqueous systems according to:

$$2Al_3^+ + 3H_2O <=> Al_2O_3 + 6H^+ \quad 6.7$$

and:

$$Al_2O_3 <=> 2AlO_2^- + 2H^+ \quad 6.8$$

The equilibrium concentration of ions in solutions can be found by consulting electrochemical handbooks according to[117]:

$$\log[Al^{3+}] = (\mu^o_{Al2O3} - 3\mu^o_{H2O})/(4.606RT) - 3pH = 8.55 - 3pH \quad 6.9$$

$$\log[AlO_2^-] = (\mu^o_{Al2O3} + \mu^o_{H2O})/(4.606RT) + pH = -11.76 + pH \quad 6.10$$

where μ^o is a chemical potential, R is the ideal gas constant, and T is temperature. Tungsten oxide dissolves according to[117]:

$$WO_3 + H_2O <=> WO_4^{2-} + 2H^+ \quad 6.11$$

with equilibrium ion concentration given by:

$$\log[WO_4^{2-}] = (\mu^o_{WO3} + \mu^o_{H2O})/(4.606RT) + 2pH = -14.05 + 2pH \quad 6.12$$

Plotting the equilibrium ion concentrations in solution (Figure 6.15) and noting that higher concentration indicates favorable conditions for dissolution of the solid material, it is evident that Al_2O_3 dissolves in both acidic and basic solutions, while WO_3 dissolves in neutral / basic solutions only. Thus a 1 molar pH 7.0 sodium phosphate buffer (Teknova) is used to

selectively remove WO_3 containing barrier layers without widening the AAO pores by etching 10 minutes at room temperature. as seen in the SEM cross section of Figure 6.15(b).

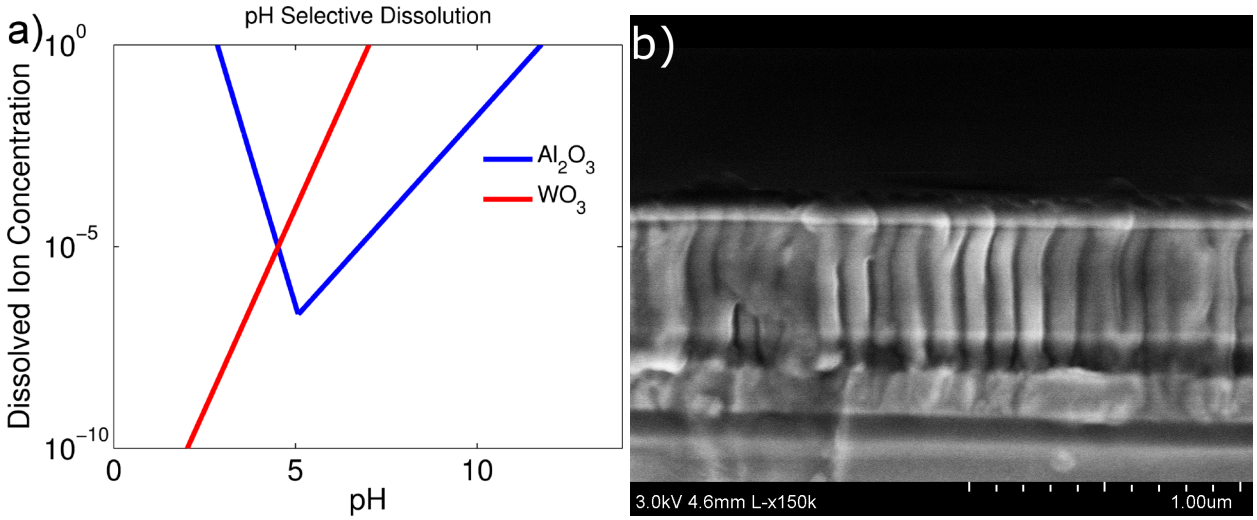

Figure 6.15 - (a) Equilibrium ion concentrations dictating the etching of Al_2O_3 and WO_3 in aqueous solutions as a function of pH. (b) AAO film on ITO with WO_3 barriers selectively removed via buffer etch.

Finally, we consider the pulsed current electroplating of copper into the AAO / ITO porous template to form metal nanorods on a transparent conductive substrate, under the same conditions described above for plating onto a gold backplane. Under SEM in Figure 6.16, we see from a top view of the sample that copper plates into large (>1 μm) aggregates in a few places on the sample rather than homogeneously filling the nanoporous template. Decreasing the current density for a more gentle plating process did not improve these results. We believe that ITO is a poor seed layer for the plating process, thus copper ions driven out of solution will tend to deposit on other areas with copper rather than onto ITO, limiting the number of places where copper deposition successfully begins. To date, we have been unable to realize successful metal rod plating on ITO with the facilities at Michigan, though other research groups have found success with this approach[104, 105].

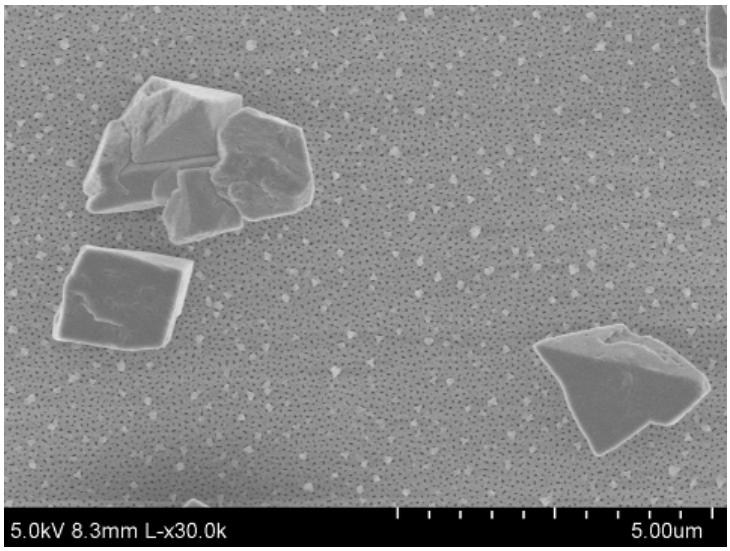

Figure 6.16 - Copper aggregates on top of AAO template formed during electroplating.

Overall, the bottom-up nanofabrication approach for patterning metal nanorods via an AAO scaffold has been unreliable, and significant compromises to the transparency of the sample have been required to ensure conductivity and the stability of layers during anodizing (as with thin gold, adding the protective tungsten and titanium adhesion layer reduces ITO transparency). Additionally, this strategy only allows patterning of materials that can be reliably electroplated. Aluminum, for example, is known to be very difficult to deposit in this way[117, 118]. Carrying out this process has, however, provided significant additional insight into engineering of the AAO growth process, including material compatibility and protection during anodizing and selective removal of barriers. These insights will be exploited in the next section.

Top-Down Etching of Metal Rods

While a simple e-beam evaporation of metal into AAO nanopores cannot be used to realize high aspect ratio structures, evaporating material onto (and into) a through-hole AAO lattice and then removing the AAO does provide a possible method for large area self-assembled patterning of an array of nanodots on a surface[103]. This patterning method is similar to the

nanosphere lithography process used to pattern silver nanoparticles in Chapter 3, though does not suffer from the inclusion of large area 'islands' where the nanosphere self-assembly is non-ideal[61, 62]. Taking advantage of this process, we outline an alternate large area fabrication strategy for arrays of metal nanorods, in which nanoparticle aspect ratios will be achieved via anisotropic reactive ion etching (RIE)[119-125] (rather than depending on the high aspect ratio nature of AAO templates).

The layer stack of Figure 6.17(a) is prepared by e-beam evaporation of 150 nm aluminum onto glass slides, PECVD deposition of 50 nm SiO_2 at 200° C, DC sputtering of 12 nm tungsten, and evaporation of 600 nm of aluminum. The sample is anodized in a 2 wt% phosphoric acid / 30% ethanol electrolyte at room temperature at a constant anodization current of ~3.8 mA / cm^2 to form self-assembled pseudo-ordered AAO nanopores of ~80 nm width and ~300 nm spacing (Figure 6.17(b)). Constant current anodization is chosen to ensure that the current density never reaches values sufficient to cause breakdown and burning. Anodization is allowed to proceed at constant current until aluminum is consumed and the voltage (allowed to vary until this point) increases to 200 V, at which point the power supply switches over to constant voltage mode, and current is allowed to drop to a steady value (~10% of the anodizing current) associated with slow oxidation of the tungsten interlayer. Current and voltage vs. time for a typical anodization with this process are shown in Figure 6.18(a) and a typical AAO pattern is shown in Figure 6.18(b). Thin tungsten and SiO_2 layers effectively protect the bottom Al layer from the anodization process - this layer remains metallic and reflective. The SiO_2 layer also protects the underlying Al from subsequent chemical processing steps. Additionally, we note that all of the materials included in this stack are entirely stable under anodization conditions, causing no problems with sample corrosion or delamination.

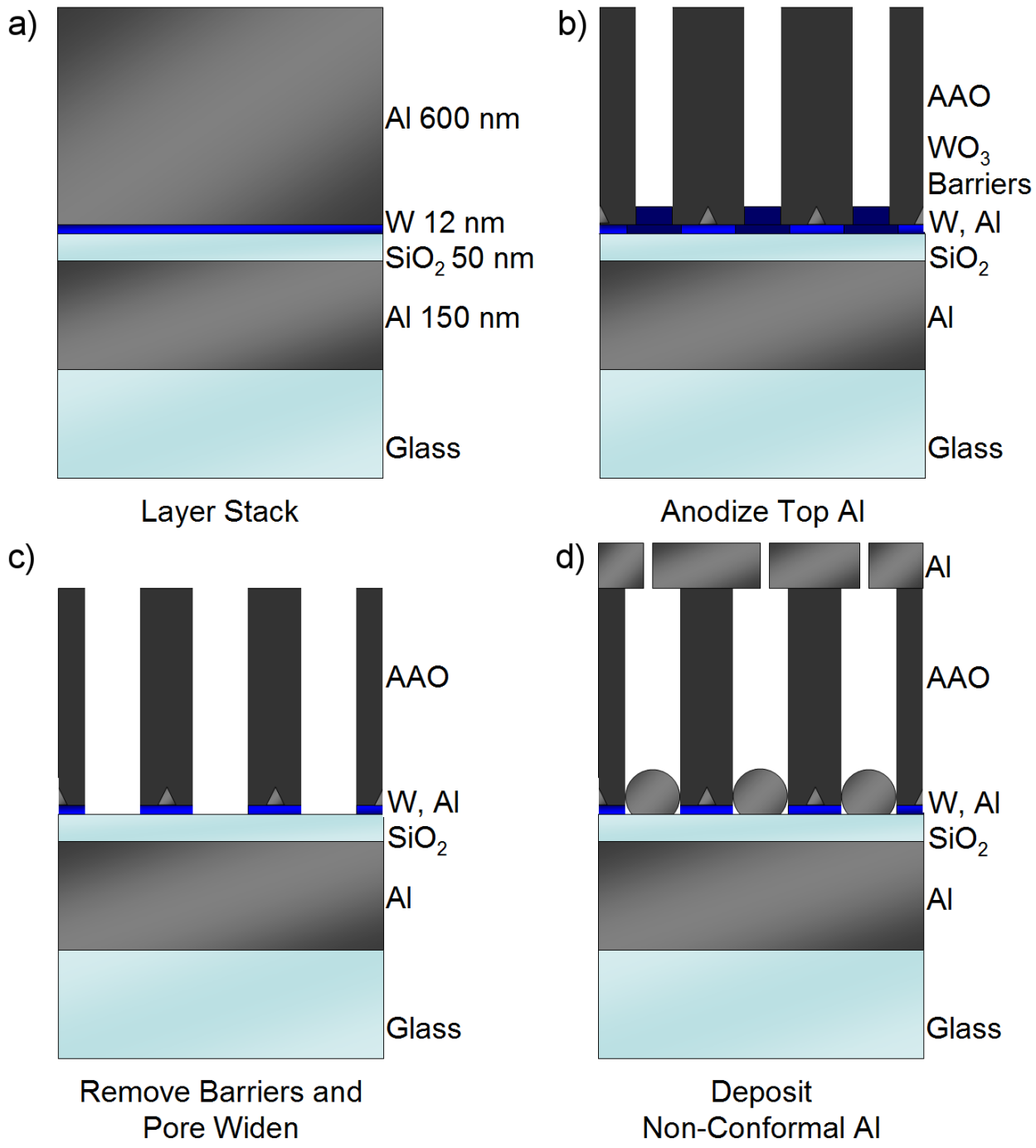

Figure 6.17 - Diagram of top down fabrication process. (a) Layer stack. (b) Anodization. (c) Barrier removal and pore widening. (d) E-beam deposition of aluminum

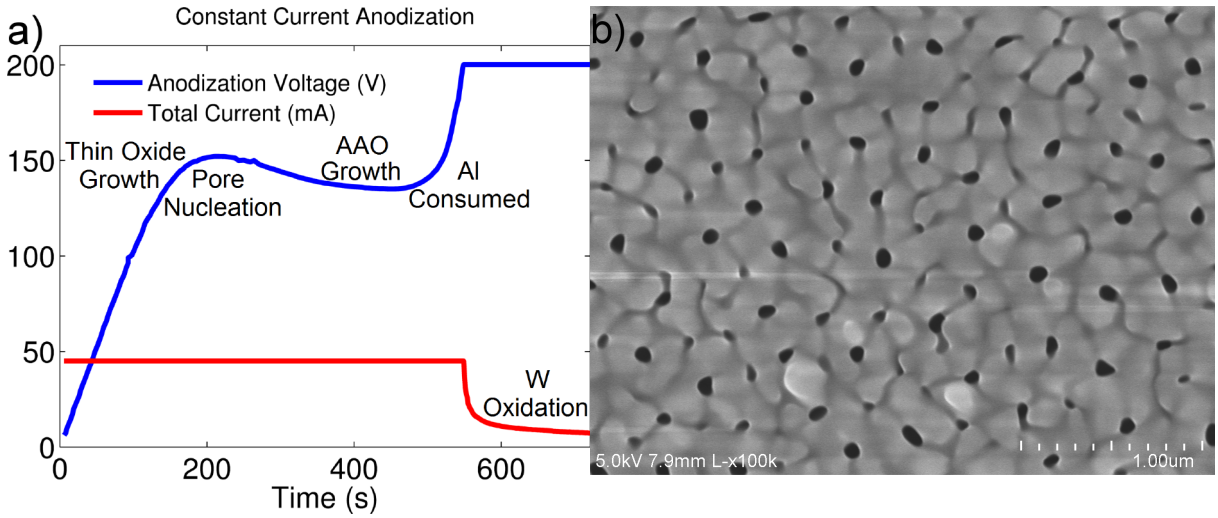

Figure 6.18 - (a) Current and voltage vs time for phosphoric acid anodization. (b) Typical pseudo-periodic AAO pattern

After anodization, AAO pore bottoms are opened in a 1 molar sodium phosphate buffer etch for 25 minutes at room temperature, exposing the PECVD SiO_2 interlayer. The AAO nanopores are widened in 5 wt% phosphoric acid at 50° C for 1 - 3 minutes to ensure good through-pore channels (Figure 6.17(c)). A third e-beam evaporation of aluminum is carried out, resulting in an array of pseudo-ordered Al nanodots being deposited at the bottom of the pores onto the PECVD oxide, and an Al coating on the top of the AAO layer (Figure 6.17(d)). Nanodot aspect ratios are limited to ~1, as the metal deposition on the top of the sample eventually blocks the AAO channels.

Next, all of the unwanted patterning layers above the PECVD oxide are lifted off. While it is possible to remove the AAO layer using a phosphoric acid wet etch, phosphoric acid also attacks evaporated aluminum[126], making it a poor choice for preserving the other layers in the stack. Also, the slow dissolution of AAO tends to allow films on top of the AAO to settle downward onto the patterned dots as seen in Figure 6.19 for the case of SiO2 dots evaporated into an AAO template which is subsequently removed - the top SiO2 layer remains on the sample.

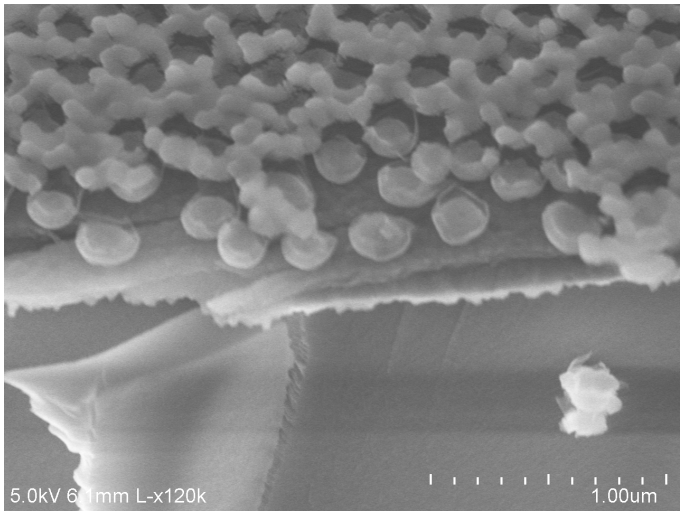

Figure 6.19 - SiO_2 dots deposited by e-beam evaporation into an AAO template followed by wet etch of AAO structure. SiO2 from the top of the AAO layer remains on top of the desired dot pattern.

For improved liftoff with this structure, we propose a mechanical process. Note that the tungsten layer in this stack which allows selective AAO barrier removal was deposited without an accompanying titanium adhesion layer. While adhesion is sufficient to hold the sample together during the anodizing process (and general processing such as rinsing with DI water / drying with N_2), the tungsten layer is unable to maintain adhesion if the top layers are lifted off mechanically with adhesive tape (Figure 6.20(a)). After liftoff, any remaining tungsten on the surface can be selectively removed by etching in 30% hydrogen peroxide (H_2O_2) at room temperature for 3 minutes[126].

The resulting surface after liftoff is imaged by SEM and shown in Figure 6.20(b). Al nanodots on oxide are seen, but additional aluminum residue is seen surrounding the dots. This is the portion of the original aluminum film which was furthest from the nanopores during anodizing, and was thus never converted to Al_2O_3 (the remaining aluminum 'points' diagrammed in Figure 6.17(b) and 6.17(c)). These residual aluminum layers are not well adhered to the AAO and thus are not removed during mechanical adhesive tape liftoff, then settle on the surface when the underlying tungsten is removed in H_2O_2.

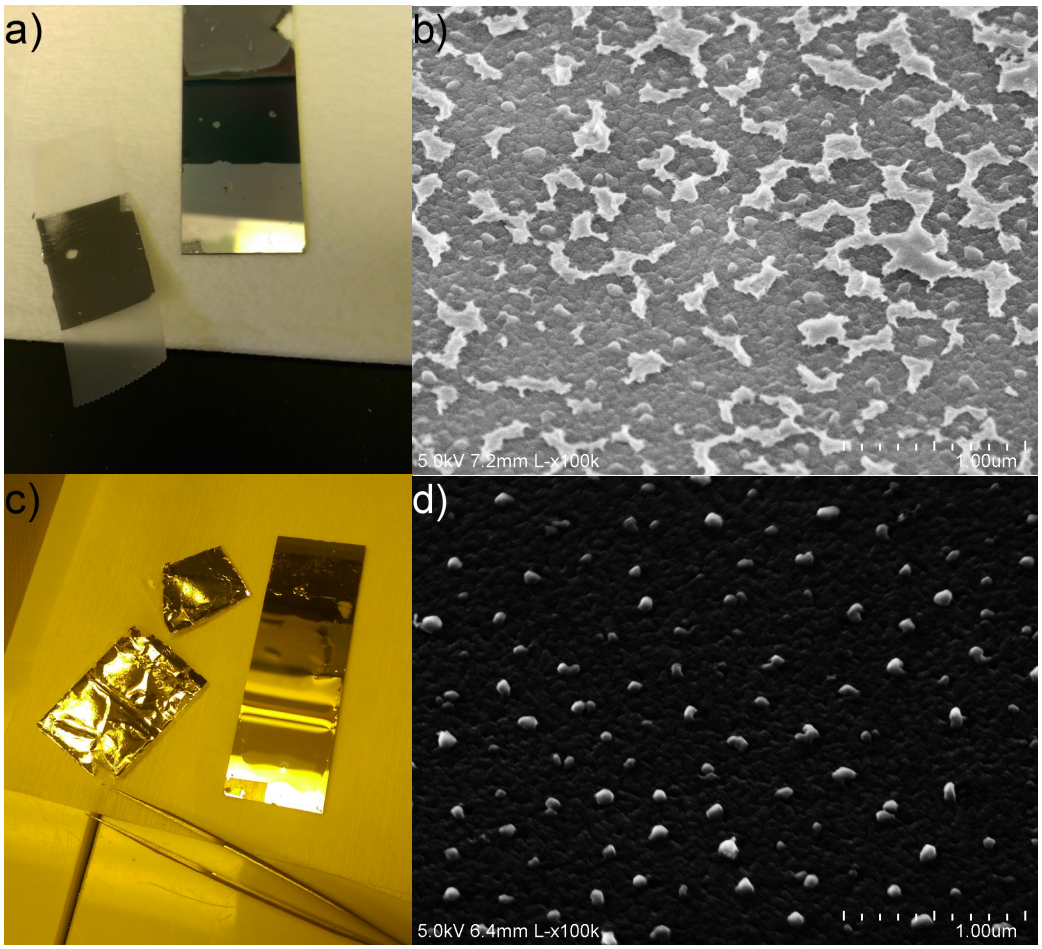

Figure 6.20 - (a) Mechanical liftoff of AAO from sample using adhesive tape. (b) SEM of patterned structure after mechanical liftoff and tungsten etch. (c) Liftoff of AAO via adhesive tape and hydrogen peroxide soak. (d) Al nanodots patterned on PECVD oxide layer.

To improve liftoff, adhesive tape is placed on the surface of samples and left in place during a 1 hour soak in 30% hydrogen peroxide. Tungsten is selectively removed from the sample and all of the unwanted layers (including portions of un-anodized aluminum) are disconnected from the PECVD oxide and remain with the adhesive tape (Figure 6.20(c)), leaving only a reliable pattern of Al nanodots as seen in Figure 6.20(d).

Once liftoff is complete (Figure 6.21(a)), the aluminum dot pattern is used as a hard mask and transferred to the underlying PECVD oxide via a reactive ion etch in a parallel plate plasma etcher (Plasmatherm 790). Oxide etching has excellent selectivity over aluminum, allowing the

underlying aluminum layer to be exposed, now masked by silicon dioxide dots with aluminum on top (Figure 6.21(b)). A final reactive RIE is carried out in an inductively coupled plasma etcher (Oxford Plasmalab 100) equipped with chlorine based gas chemistry[121-122] to remove the aluminum dots from the top surface and anisotropically etch through the bottom aluminum film using SiO_2 as the etch mask (Figure 6.21(c)). Reactive ion etch conditions for etching each material are reported below in Table 6.1. The aluminum etch is carried out in two steps - a 5 second etch is used to break through the native oxide coating on the Al, then power and pressure are reduced when etching bulk metal. Methane (CH_4) included with the chlorine gasses allows the formation of polymers that protect feature sidewalls for improved anisotropy[120]. The result is approximately vertical aluminum nanorods capped by SiO_2 dots as shown in Figure 6.22.

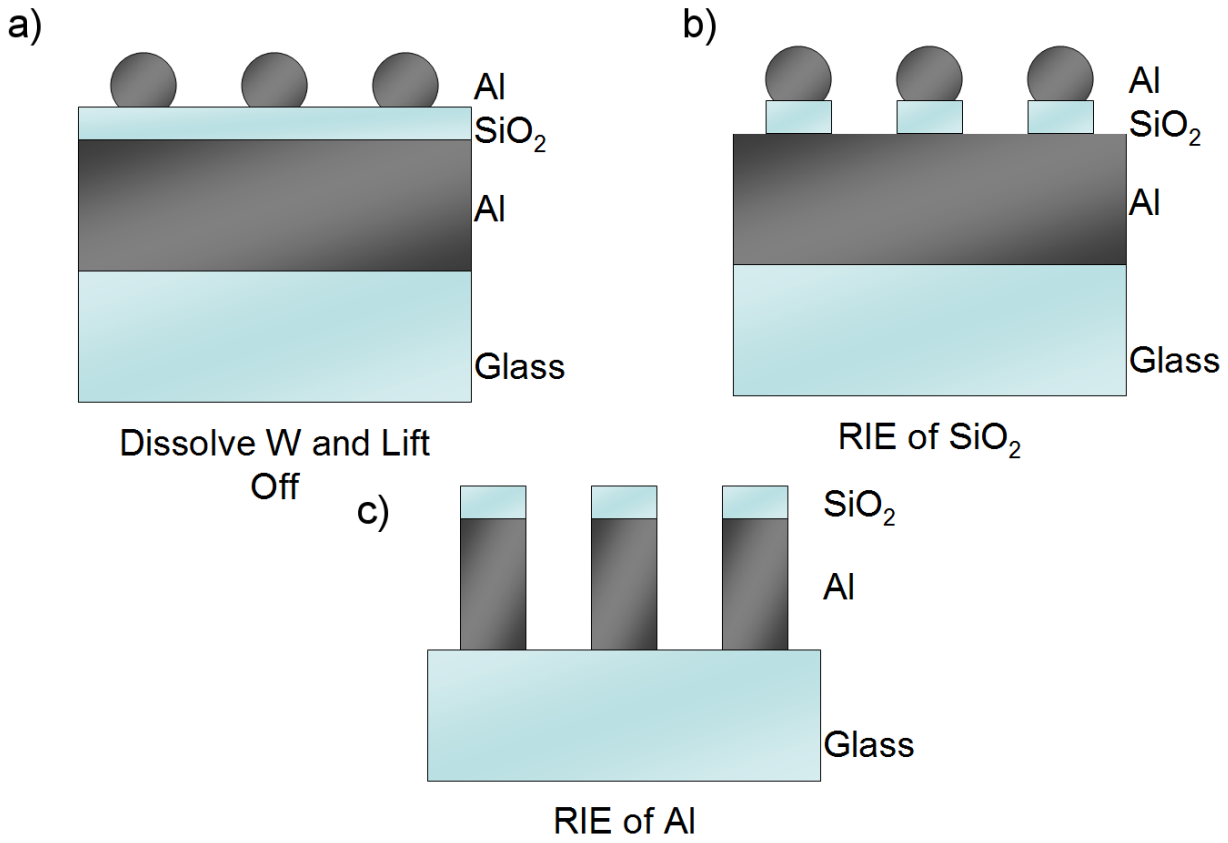

Figure 6.21 - Continued diagram of top-down fabrication process. (a) Sample after liftoff. (b) RIE of SiO_2 interlayer. (c) RIE of Al into nanorods.

	Step 1	Step 2	Step 3
Tool	Plasmatherm 790	Oxford Plasmalab 100	Oxford Plasmalab 100
Target Material	SiO_2	Native Al_2O_3	Al
Mask Material	Al	SiO2	SiO2
Chamber Pressure	20 mTorr	10 mTorr	3 mTorr
Gas 1 Flow	CF_4 - 15sccm	Cl_2 - 15sccm	Cl_2 - 15sccm
Gas 2 Flow	CHF_3 - 15sccm	BCl_3 - 30 sccm	BCl_3 - 30 sccm
Gas 3 Flow	-	CH_4 - 8 sccm	CH_4 - 8 sccm
Plate Temperature	-	50° C	50° C
RF Etch Power	150 W	100 W	100 W
ICP Power	-	300 W	100 W
Etch Time	300 s	5 s	20 s

Table 6.1 - Reactive ion etch parameters for etching SiO_2 dots and Al nanorods, including the removal of native oxide fomed on the Al layer. Gas flow parameters are reported in standard cubic centimeters per minute (sccm).

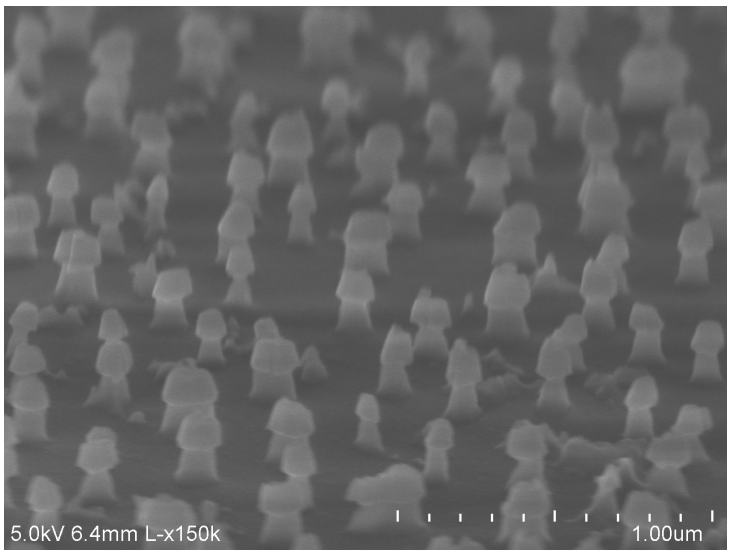

Figure 6.22 - Large area patterned aluminum nanorods with SiO_2 caps formed by RIE.

The top-down approach demonstrated here realizes large area pseudo-periodic nanorod arrays directly on glass for maximum transparency. Nanorod spacing can be controlled via anodization voltage, and nanorod diameter can be controlled by the amount of time the pores are isotropically widened after barrier removal. Rod height and aspect ratio can be determined by the thickness of the base aluminum layer. The SiO2 caps on the nanorods can be removed by a

subsequent RIE of SiO2 (which attacks PECVD oxide more readily than the commercial glass substrate), or left in place to increase the effective refractive index surrounding the nanorods, further redshifting LSP resonant properties. This fabrication approach can potentially be used with any metal for which reactive ion etching recipes exist[123-125], provided that the SiO_2 and tungsten interlayers are sufficient to protect the bottom layer from the anodizing conditions.

In ongoing work, we seek to further improve nanorod diameters from 80 - 120 nm (Figure 6.22) down to 30 - 50 nm and demonstrate different aspect ratios and nanorod spacings. Other parameters of this process including the RIE etch recipe (for improved vertical sidewalls and reduced mask undercutting) and nanorod uniformity remain to be optimized as well.

CHAPTER VII

Non-Metallic Nanostructures: High Aspect Ratio Dielectric Structure

Thus far, we have focused on the scattering properties of anisotropic (vertical) metal nanoparticles which demonstrate an angle selective optical response, and have proposed integrating an array of such particles with thin film semitransparent PVs to enable angle selective photovoltaic windows for building integrated solar energy harvesting. As described in Chapter 6, the large area fabrication of metal nanorod arrays can be realized via with self assembled anodized aluminum oxide (AAO) nanopatterning. However, both the bottom-up and top-down fabrication strategies involve a number of steps to be carried out and optimized, limiting the utility of the results thus far.

In this Chapter, we consider the scattering properties of AAO itself, a non-metallic anisotropic (and high aspect ratio) nanostructure. Unlike plasmonics, light scattering occurs only in transparent dielectric materials, reducing intrinsic optical losses. Additionally, light scattering in AAO is found to be non-resonant, increasing the bandwidth of light which can be captured.

AAO Scattering Properties

A simple diagram of the interaction of light with a high aspect ratio through-hole AAO template is shown in Figure 7.1(a)[41]. Normally incident photons (z direction) will pass through the nanopores or through the transparent oxide layer with minimal loss. Angled light, which propagates across the (x / y) lattice directions will probe the sub-λ structure, undergoing multiple

scattering off air / dielectric interfaces, corresponding to a more complicated optical mode in the structure and giving rise to a net backscattered wave[42]. In the case of highly periodic AAO, coherent scattering off the structure and interference effects determine bloch periodic and photonic crystal modes[73, 127-128], though even pseudo-periodic AAO can be expected to demonstrate similar behavior. Transmission and optical density in AAO has been well described in the literature by considering the structure as an array of infinite cylinders[129, 130] (bulk scattering component), plus surface scattering, and interference effects[129-133]. For interaction with visible light, x / y lattice features should be on the order of the visible wavelength (100's of nm) - features which are too small compared to λ will tend to present only an 'effective index' to the wave, thus scattering is also expected to fall off with increasing wavelength[133].

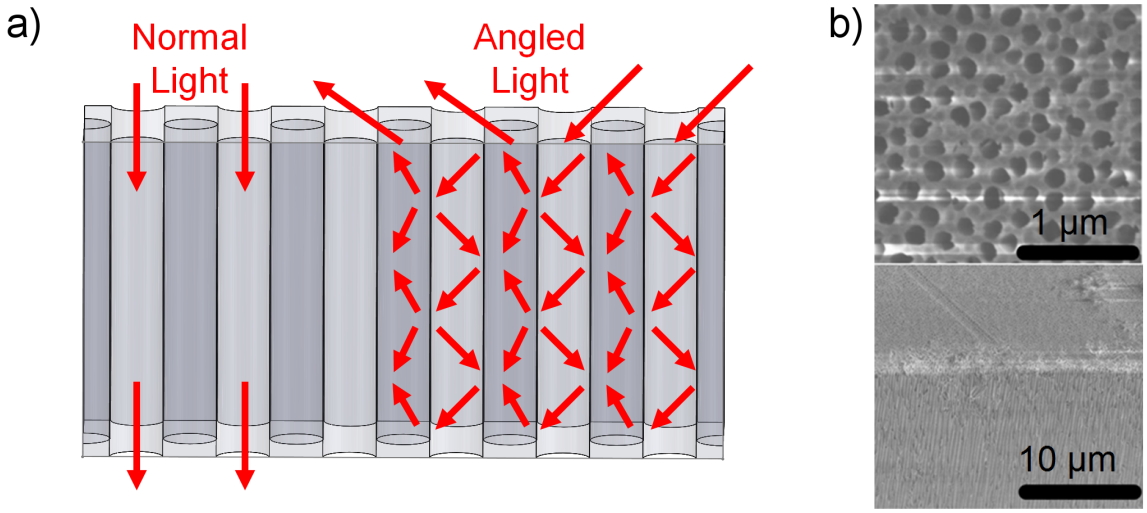

Figure 7.1 - (a) Interaction of AAO lattice with normally incident (transmitted) light and light at angled incidence which undergoes multiple scattering off the sub-λ structure. (b) SEM images of commercial AAO template from the side and top. Scale bars are 1µm.

Pseudo-periodic commercial AAO templates with 200 nm pore size, 300 nm pore spacing, and 60 µm thickness (Figure 7.1(b)) were purchased from Whatman Ltd. Similar AAO lattices have been realized in our lab via high voltage anodization in phosphoric acid, though achievable film thickness using the methodology of Chapter 6 is limited to ~1.5 µm (thickness of

evaporated Al on glass) due to sample polishing and burning issues[110-114]. As dielectric interfaces in AAO scatter more weakly than the metal nanoparticles considered previously, greater film thickness is required for significant modulation of light.

Optical properties of the AAO membrane alone are measured via lock-in techniques using a 200 W tungsten-halogen source (Hamatsu), a monochrometer (Princeton Instruments) and an integrating sphere (Sphere Optics). Direct (specular / line of sight) transmission though the AAO film is measured at various angles of incidence, as plotted in Figure 7.2(a). When angle of incidence is increased from 0º to 45º, transmission decreases across wavelengths 400 – 600 nm - transmission at 600 nm drops from 52% (0º) to 45% (15º), 15% (30º), and 2% (45º).

Integrated transmission and backscattering measurements are carried out as well (via integrating sphere), capturing the full angular range to which light is transmitted and backscattered. The integrated transmission intensity (Figure 7.2(b)) is observed to be higher than the direct transmission (Figure 7.2(a)), irrespective of incident angle - at 45º, for example, the 600 nm integrated transmission is 60% measured compared to less than 2% direct. Therefore, a significant proportion of transmitted light is scattered obliquely away from line of sight when propagated through the AAO at each angle. However, even the integrated transmission is reduced up to 24% between 400 and 700 nm wavelengths when the angle of incidence is increased from 0º (circles) to 45º (squares) - integrated transmission decreases from 85% (0º) to 61% (45º) at 600 nm.

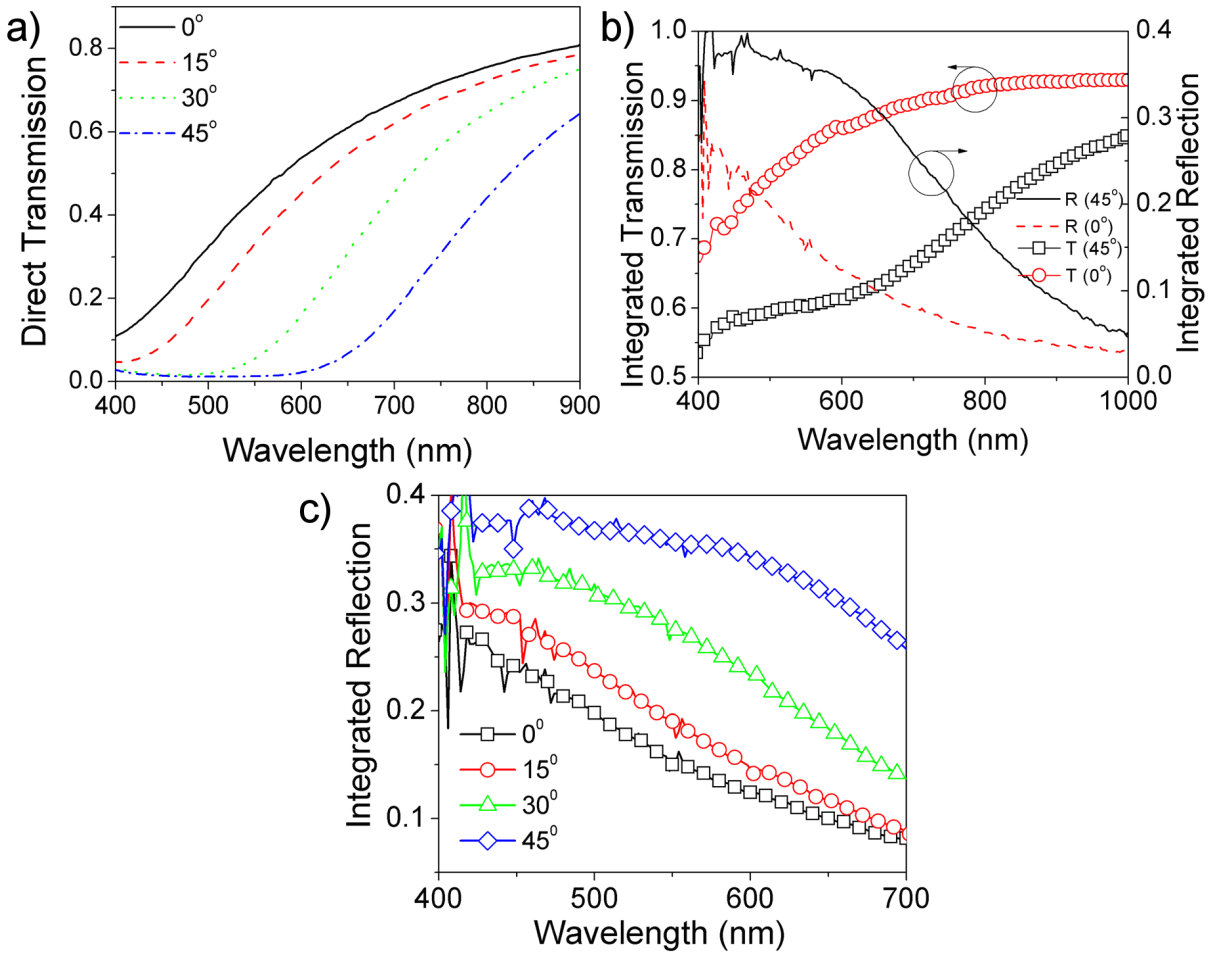

Figure 7.2 - (a) Direct (specular) transmission spectra through AAO vs. incident angle. (b) Integrated (all angles) transmission and reflection at 0º (red) and 45º (black) incidence. (c) Integrated backscatter from 0º to 45º incidence.

To account for the drop in transmission, integrated reflection (backscattering) by the AAO is measured from 0º to 45º as well (Figures 7.2(b), 7.2(c)), increasing up to 22% - at 600 nm, backscattering increases from 12% (0º) to 34% (45º). The increase in integrated backscattering with angle lines up with the decrease in integrated transmission, with no additional optical losses in the system. Backscattering is greater than 35% at 45º incidence on 400 - 650 nm, overlapping with the highest available (visible) power in the solar spectrum, allowing use of AAO as an angle selective backscattering layer for semitransparent PV.

Angle selective scattering of light by AAO can also be observed by naked eye, as shown in Figure 7.3 - the 60 μm AAO is translucent at normal incidence (Figure 7.3(a)) and becomes opaque (and remains colorless) when tilted at an angle (Figure 7.3(b)).

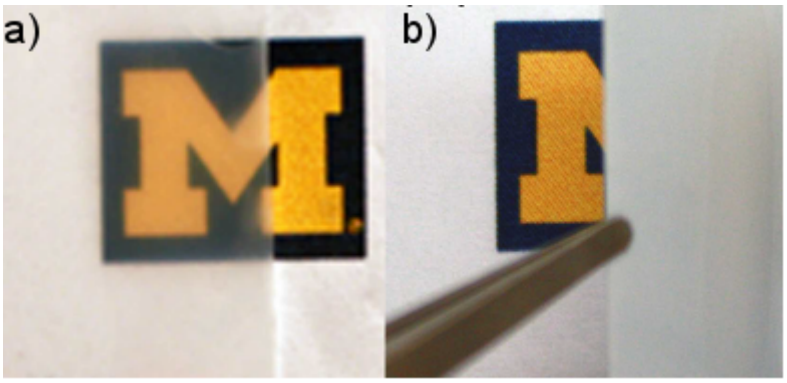

Figure 7.3 - AAO layer viewed at (a) normal incidence (translucent) and (b) angled incidence (opaque).

Angle Selective Semitransparent PV Performance

A P3HT:PCBM based inverted organic PV like that of Chapter 3 was fabricated on glass to test the AAO layer as an angle selective backreflector (Figure 7.4(a))[41]. The AAO template was soaked in DI water and placed flush against the back side of the glass. Filling the nanopores with water (visible refractive index $n = 1.33$) decreases the index contrast at each nanopore / Al_2O_3 interface, reducing the total scattering but significantly improving normal incidence transparency, and allowing adhesion to the glass via surface tension. Although DI water provided adequate adhesion and optical coupling between AAO and PV to illustrate the concept, use of a higher boiling point and low vapor pressure transparent solution (e.g., index matching oil) will be needed for robust and practical implementation. The device was illuminated through the thin gold front contact at varied angles of incidence. For 0^o –30^o, the illumination beam area was contained within the device area (1 cm^2). Figure 7.4(b) shows the change in the zero bias spectral

photocurrent at varied angles with (solid curves) and without (dashed curves) an AAO backreflector.

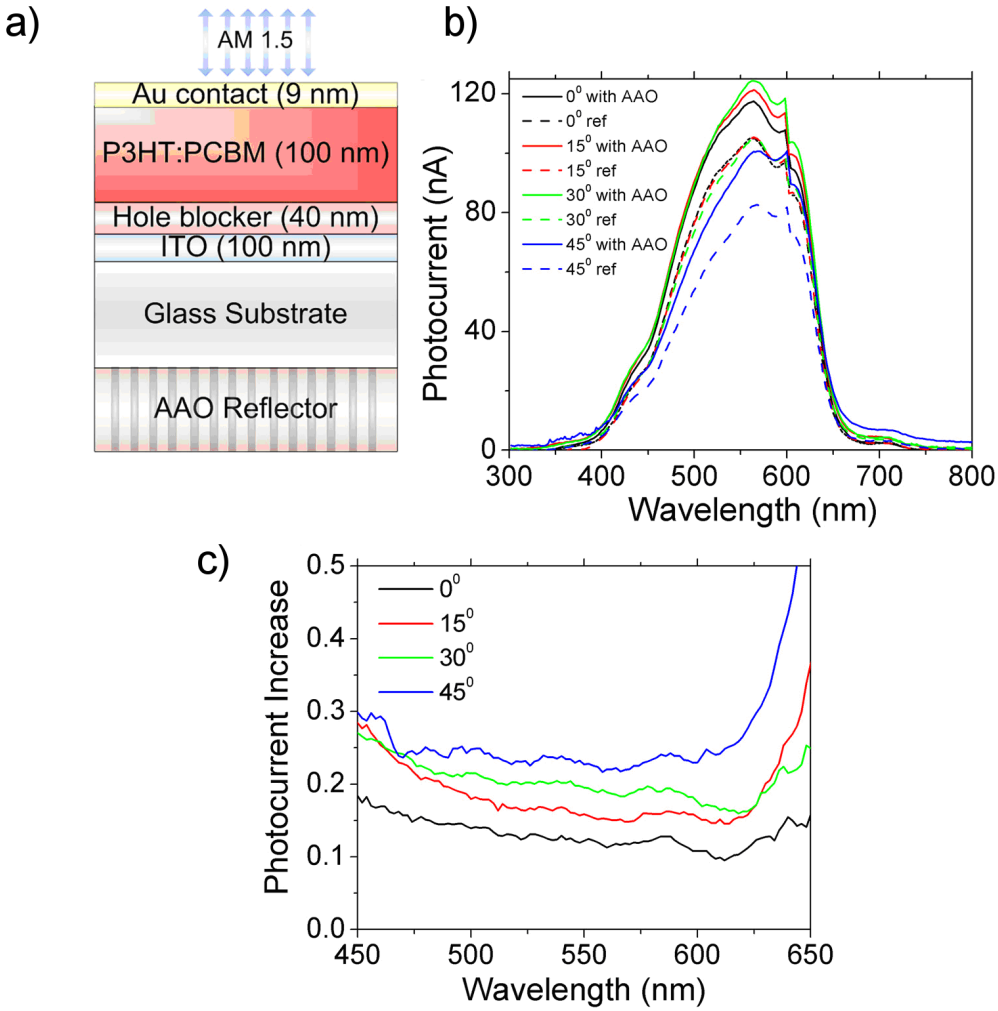

Figure 7.4 - (a) Semitransparent organic PV integrated with AAO reflector layer. (b) Zero bias photocurrent measured as a function of wavelength and incident angle with (solid) and without (dashed) the AAO backscattering layer. (c) Fractional increase in photocurrent vs. reference when AAO layer is added.

The first aspect to note is that the photocurrent of the PV with AAO backreflelector is higher than the control at all angles. (i.e., photocurrent at 564 nm is increased from 105 nA to 117 nA, 121 nA, and 124 nA at angles 0º, 15º, and 30º, respectively). Even at 45º, where the baseline photocurrent of the control drops due to the illumination area

exceeding the active device area, reducing incident optical power density, the AAO backreflector shows clearly higher photocurrent. The second aspect to note is that, unlike the control which does not show the change of photocurrent with angle, the AAO backreflector coupled device shows photocurrent increase with increasing angle. The overall increase in photocurrent with the AAO back scattering at different angle of incidence is presented in Figure 7.4(c). Photocurrent at 500 nm is increased by 10% at 0^o to 23% at 45^o. Furthermore, the photocurrent shows an improvement of close to 23% for the entire visible rage at 45^o. The angle dependent improvement in photocurrent follows closely the increase in backscattering observed in Figure 7.2(c).

Figure 7.5(a) shows the current / voltage characteristics of the organic PV under AM1.5 solar illumination at various angles of incidence, with (solid) and without (dashed) the AAO layer. The illumination is kept within the active device area such that baseline photocurrent of the control does not change with incident angle (aside from small variations due to the areal spreading of illumination with rotation). The AAO backscattering layer improves short circuit current (I_{sc}) at all angles as compared to the control. When angle is increased from 0 to 60^o, the AAO integrated PV shows a distinct increase in I_{sc}. Addition of the AAO reflector does not significantly change the cell's open circuit voltage (.22 V) or fill factor. Short circuit current enhancement of the AAO device as compared to the reference is plotted vs. angle in Figure 7.5(b). At elevation angles greater than 30^o, corresponding to the time averaged elevation angles of direct sunlight, photocurrent is increased by more than 20% up to a maximum of 30% at 60^o.

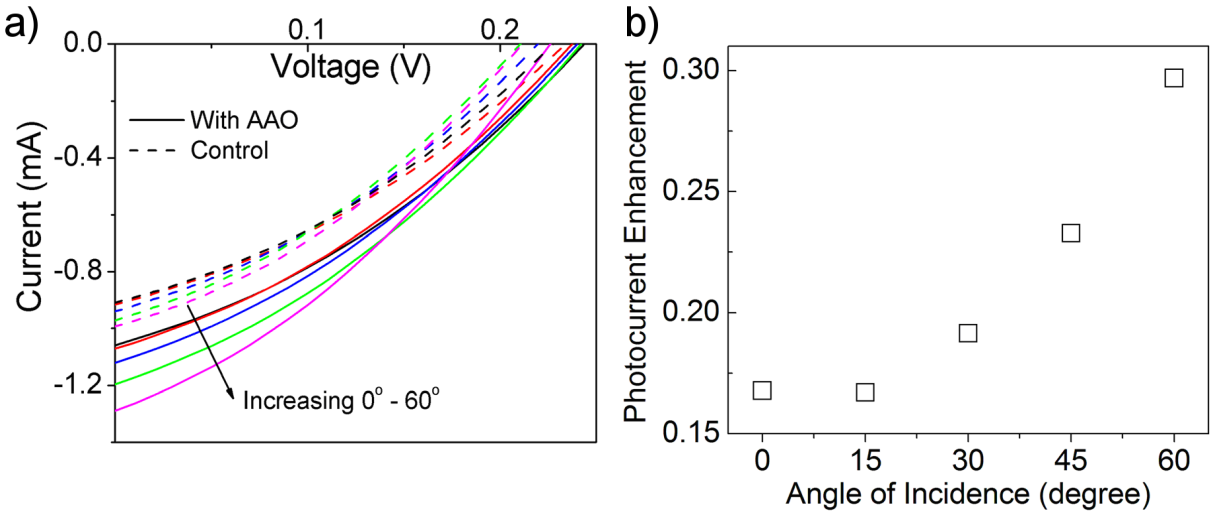

Figure 7.5 - (a) Current / voltage characteristics for semitransparent organic PV with (solid) and without (dashed) AAO layer., showing angle selective harvesting of light for the AAO case. (b) Enhancement in short circuit photocurrent vs. the reference device due to adding AAO layer as a function of incident angle.

Visibly, the PV device with AAO scattering layer is observed to be semitransparent at normal incidence (Figure 4.6(a)), only becoming opaque when viewed at an angle (Figure 4.6(b)). We note the purple color of the PV is due to the choice of P3HT:PCBM, and could be avoided by further (independent) optimization of the solar cell layers[33-35].

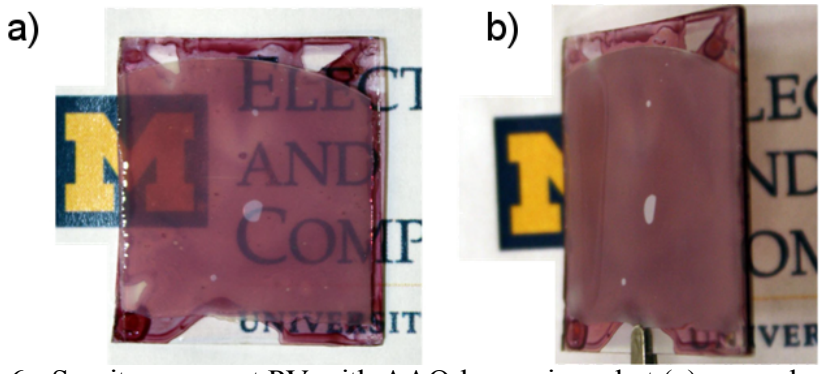

Figure 7.6 - Semitransparent PV with AAO layer viewed at (a) normal and (b) angled incidence.

Anisotropic high aspect ratio AAO nanostructures show significantly different scattering properties at normal vs. angled incidence, and can be integrated with semitransparent PV layers to realize an angle selective photovoltaic window. We have demonstrated up to 30%

improvement in photocurrent when harvesting light at an elevated angle (including direct sunlight) without significantly sacrificing transmission in the normal direction. Unlike the anisotropic metal nanostructures described in Chapter 4, AAO introduces no intrinsic losses to the system, light scattering is found to be broadband across the visible, and both polarizations of light can be scattered. Metal structures, however, have the advantage of superior tunability (via LSP resonance properties), and the stronger scattering by metal particles means a much smaller backscattering layer is required (~100 nm vs. 60 μm thickness for pseudo-random AAO).

CHAPTER VIII

Conclusions and Future Work

This dissertation has explored and demonstrated the potential for nanostructures to realize wavelength and angle selective management of light for new functionalities in photovoltaics and optical coatings. Emphasis is placed on metallic nanostructures which demonstrate a localized surface plasmon resonance and anisotropic structures which present different properties to incident light based on angle.

Summary

The motivation for this work and the essential optical physics of plasmon resonances are reviewed in Chapter 1. Analytical expressions[11, 12] are introduced and plotted to demonstrate LSP resonance tunability for silver, gold, and aluminum nanospheres of various sizes and paired with various surrounding materials.

In Chapter 2, we consider metallic nanoparticles paired with thin film photovoltaic absorbing materials and investigate the physical mechanisms by which light absorption is enhanced. A novel data analysis method is presented based on finite difference time domain (FDTD) optical simulations[59, 60], which allows broadband calculation of light absorption in arbitrary regions and decoupling of near field vs. scattering plasmonic properties. From these results, we propose metal nanoparticles as a wavelength selective backscattering layer to be

placed behind a thin film semitransparent PV, an example of which is described and demonstrated experimentally in Chapter 3[61].

Angle selectivity is added to our proposed metal nanoparticle backscattering layer in Chapter 4 by considering anisotropic metal particles[39, 40]. Analytical expressions for the polarizability of ellipsoids and numerical simulations of cylindrical particles are presented to demonstrate an angle and polarization dependant split in the LSP resonance which allows transmission of normally incident light and absorption / scattering of TM polarized angled light. Aluminum nanorods placed behind a thin film semitransparent PV can enable an angle selective photovoltaic window, in which transmitted and absorbed light are decoupled by angle, allowing a ~20% improvement in absorption of direct sunlight without sacrificing window transparency.

In Chapter 5, we consider a light management application outside of photovoltaics, in which we propose using the angle selective LSP resonance properties of metal nanorods to enable an adjustable transmissive system for smart glass[43-47] applications. Tunability is realized with an actuating micro-origami structure that controllably rotates nanorod orientation with respect to incident light. Choosing a variety of nanorods and balancing their extinction properties, color neutral 0 - 90+% modulation of the visible spectrum (400 - 725 nm) is described for the proposed device.

Chapter 6 describes current and ongoing work to nanofabricate arrays of metal nanorods by patterning with self-assembled electrochemically grown anodized aluminum oxide films[96-115]. The growth mechanisms of AAO are reviewed, and the challenges involved in working with this material system are described. Progress on two approaches is presented: bottom-up nanorod growth realized by electroplating metal into nanoporous AAO on a transparent conductive backplane[104-105], and top-down fabrication via reactive ion etching of metal. Promising early

results are shown with the top-down approach for realizing large area pseudo-periodic arrays of aluminum nanorods.

Finally, in Chapter 7, we consider the scattering properties of non-metallic AAO itself. As an anisotropic, high aspect ratio structure, an array of nanopores in dielectric also shows angle dependant light scattering, albeit via a different physical mechanism. An AAO membrane is used to experimentally demonstrate an angle selective photovoltaic like that described in Chapter 4, for which photocurrent under angled light is improved by 30% as compared to a reference device[41].

Future Work

Building on the results herein, future work will focus on further demonstration of large-area fabrication of metal nanorods on transparent substrates (via the top-down mechanism of Chapter 6) and angle dependant optical measurements of transmission, absorption, and scattering of light like those performed on AAO in Chapter 7. Various aluminum nanorod aspect ratios and nanorod spacings will be prepared and measured to correlate LSP resonant extinction properties with expectations from simulation and analytical expressions. Additional exploration of the nanofabrication process will be performed as well, toward realizing metal nanorods of additional materials (gold, silver) and on different substrates (e.g. paralyne).

Nanorod arrays can be integrated with thin film PV (like those of Chapters 3 and 7) as an additional proof of concept for the angle selective window device, though as noted in the analysis of Chapters 4, intrinsic optical losses and the modulation of TM light only limit the utility of this approach. The AAO scattering device of Chapter 7 is a more promising direction for future work on this application, including numerical modeling of the multi-scale scattering

properties[42] and further refinements of the AAO growth process at high voltage[110-114] to realize near-λ scale AAO structures in-house.

As the proposed actuating structure of Chapter 5 could represent a significant improvement in visible spectrum transmission modulation as compared to current approaches[43-47], significant future work will be devoted to this idea. Further analysis and fine tuning of the structure will be carried out via numerical simulation to account for non-ideal nanorod shape, interaction between adjacent metal rods in the lattice, and transmission and scattering properties of the actuating microstructure itself. In collaboration with other researchers[88], we will also seek to experimentally demonstrate such a device, including further exploration of the fabrication of corrugated structures and the addition of metal nanorods via our AAO approach or chemical synthesis methods[89-91].

APPENDIX A

Sample Command File for MEEP Electromagnetic Simulation

```
(define a 1e-6)                      ; basic unit (micron)
(define cc (/ (* 2 (* pi 3e+8)) a)) ; unit of frequency (w) in meep
(define h_bar 6.582119e-16)          ; planck's constant h bar in eV sec

(define-param wlength .5)            ; wavelength of pump in um
(define fcen (/ 1 wlength))          ; center frequency
(define-param df 3.3)                ; gaussian pulse width (in frequency)


;;;;; Polymer MATERIAL ;;;;;

(define POLY            ; n=1.8, broadband absorptoin coeff. alpha 5e4/cm
      (make medium
      (epsilon 3.2004)
      (D-conductivity (/ (* 2 pi fcen 0.7162) 3.2004) ))
)


;;;;; Glass MATERIAL ;;;;;

(define GLASS
      (make medium
      (epsilon 2.25) )  ; index 1.5
)

;;;;; Ag MATERIAL ;;;;;

(define wp_AG (/ (/ 9.01 h_bar) cc)); silver plasma freq, converted from eV
                                     ; to meep frequency units

(define omega1 (/ (/ .816 h_bar) cc) )    ; resonance freqs, in meep units
(define omega2 (/ (/ 4.481 h_bar) cc) )
(define omega3 (/ (/ 8.185 h_bar) cc) )
(define omega4 (/ (/ 9.083 h_bar) cc) )
(define omega5 (/ (/ 20.29 h_bar) cc) )

(define Ag              ; define each of the Lorentz-Drude polarization terms
      (make dielectric (epsilon 1.0)
      (polarizations
            (make polarizability
                  (omega 1e-20) (gamma (/ (/ .048 h_bar) cc) )
                  (sigma (* .845 wp_AG wp_AG 1e40) ) )
            (make polarizability
                  (omega omega1 ) (gamma (/ (/ 3.886 h_bar) cc) )
                  (sigma (/ (* .065 wp_AG wp_AG) (* omega1 omega1)) ) )
```

```
            (make polarizability
                  (omega omega2 ) (gamma (/ (/ .452 h_bar) cc) )
                  (sigma (/ (* .124 wp_AG wp_AG) (* omega2 omega2)) ) )
            (make polarizability
                  (omega omega3 ) (gamma (/ (/ .065 h_bar) cc) )
                  (sigma (/ (* .011 wp_AG wp_AG) (* omega3 omega3)) ) )
            (make polarizability
                  (omega omega4 ) (gamma (/ (/ .916 h_bar) cc) )
                  (sigma (/ (* .84 wp_AG wp_AG) (* omega4 omega4)) ) )
            (make polarizability
                  (omega omega5 ) (gamma (/ (/ 2.419 h_bar) cc) )
                  (sigma (/ (* 5.646 wp_AG wp_AG) (* omega5 omega5)) ) )
            )
      )
)


;;;;; GEOMETRY ;;;;;

(define-param poly_height .140)     ; thickness of polymer layer

(define-param dpml .100)            ; pml thickness

(define-param rad .025)             ; radii for nanoparticles

(define-param delta_z .025)         ; z shift of metal nanoparticle location

(define-param center-center .100)   ; MNP spacing

(define-param cell_height (* 1 poly_height) )   ; size of simulated region
                                                ; (inside PML) (microns)

(set! eps-averaging? false)

(set! geometry-lattice (make lattice
      (size center-center center-center (+ cell_height dpml dpml) ) ))


(set! geometry (list

      ; polymer everywhere:
      (make block (center 0 0 0)
            (size infinity infinity infinity) (material POLY) )

      ; metal nanosphere:
      (make sphere (center 0 0 (* -1 delta_z))
            (radius rad) (material Ag) )

))

; resolution - number of pixels per size unit a (per micron):
(set-param! resolution 600)


; perfectly matched layers in the z direction:
(set! pml-layers (list (make pml (thickness dpml) (direction Z))))
```

```
;;;;; OUTPUT SETUP ;;;;;

; planes at the input and output of the region:
(define output_block (volume (center 0 0 (* cell_height .48) )
      (size center-center center-center 0) ))

(define input_block (volume (center 0 0 (* cell_height -.48) )
      (size center-center center-center 0) ))

; volume containing arbitrary shaped metal particle:
(define mnp_block (volume (center 0 0 (* -1 delta_z) )
      (size (* 2.5 rad) (* 2.5 rad) (* 2.5 rad)) ))

; cross-section slice for visualization of geometry
(define x_section (volume (center 0 0 0 )
      (size center-center 0 (+ cell_height dpml dpml)) ))


;;;;; OPTICAL SOURCE ;;;;;

(define-param theta_source 0)
(define kx (* fcen (sin theta_source)))
(set! k-point (vector3 kx 0 0))
(set! ensure-periodicity true)

(define (my-amp-func p)
 (exp (* 0+2i pi kx (vector3-x p))))

(set! sources           ; gaussian in time and frequency
      (list
            (make source
      (src (make gaussian-src (frequency fcen) (fwidth df)))
      (component Ex) (center 0 0 (* -0.5 cell_height))
            (size center-center center-center 0)
      (amp-func my-amp-func))))


;;;;; RUNNING AND OUTPUT ;;;;;

(use-output-directory)

(run-until 20

; output dielectric constant profile in nanoparticle region:
(at-beginning (in-volume mnp_block output-epsilon))

; output dielectric constant in cross section view:
(at-end (in-volume x_section output-epsilon))

; output fields at every .1 time units:
 (to-appended "ex" (after-time 0 (at-every .1
      (in-volume mnp_block output-efield-x))))
(to-appended "ey" (after-time 0 (at-every .1
      (in-volume mnp_block output-efield-y))))
(to-appended "ez" (after-time 0 (at-every .1
      (in-volume mnp_block output-efield-z))))
```

```
 (to-appended "hx" (after-time 0 (at-every .1
      (in-volume mnp_block output-hfield-x))))
 (to-appended "hy" (after-time 0 (at-every .1
      (in-volume mnp_block output-hfield-y))))
 (to-appended "hz" (after-time 0 (at-every .1
      (in-volume mnp_block output-hfield-z))))

(to-appended "ex_in" (after-time 0 (at-every .1
      (in-volume input_block output-efield-x))))
 (to-appended "ey_in" (after-time 0 (at-every .1
      (in-volume input_block output-efield-y))))
(to-appended "ez_in" (after-time 0 (at-every .1
      (in-volume input_block output-efield-z))))

(to-appended "hx_in" (after-time 0 (at-every .1
      (in-volume input_block output-hfield-x))))
(to-appended "hy_in" (after-time 0 (at-every .1
      (in-volume input_block output-hfield-y))))
(to-appended "hz_in" (after-time 0 (at-every .1
      (in-volume input_block output-hfield-z))))

(to-appended "ex_out" (after-time 0 (at-every .1
      (in-volume output_block output-efield-x))))
(to-appended "ey_out" (after-time 0 (at-every .1
      (in-volume output_block output-efield-y))))
(to-appended "ez_out" (after-time 0 (at-every .1
      (in-volume output_block output-efield-z))))

(to-appended "hx_out" (after-time 0 (at-every .1
      (in-volume output_block output-hfield-x))))
(to-appended "hy_out" (after-time 0 (at-every .1
      (in-volume output_block output-hfield-y))))
(to-appended "hz_out" (after-time 0 (at-every .1
      (in-volume output_block output-hfield-z))))

)
```

APPENDIX B

MATLAB Program for Calculating Absorption in Arbitrary Regions

```
% load in volumetric dielectric constant data
eps_in = hd5open('eps-000000000.h5');

[kmax, jmax, imax]= size(eps_in); %pre-allocate
eps = zeros(imax,jmax,kmax);
for i=1:imax
    for j=1:jmax
        for k=1:kmax
            eps(i,j,k) = eps_in(k,j,i); %redefine arrays so x=i, y=j, z=k
        end
    end
end
clear eps_in

% load in volumetric field data
ex1 = hd5open('ex.h5');
ey1 = hd5open('ey.h5');
ez1 = hd5open('ez.h5');
hx1 = hd5open('hx.h5');
hy1 = hd5open('hy.h5');
hz1 = hd5open('hz.h5');

[tmax, kmax, jmax, imax]= size(ex1); % pre allocate
ex= zeros(kmax,jmax,imax,tmax);
ey=ex;
ez=ex;
hx=ex;
hy=ex;
hz=ex;
for t=1:tmax
    for i=1:imax
        for j=1:jmax
            for k=1:kmax
                % redefine arrays so x=i, y=j, z=k, time = t
                ex(i,j,k,t) = ex1(t,k,j,i);
                ey(i,j,k,t) = ey1(t,k,j,i);
                ez(i,j,k,t) = ez1(t,k,j,i);
                hx(i,j,k,t) = hx1(t,k,j,i);
                hy(i,j,k,t) = hy1(t,k,j,i);
                hz(i,j,k,t) = hz1(t,k,j,i);
            end
        end
    end
```

```
end

clear ex1;
clear ey1;
clear ez1;
clear hx1;
clear hy1;
clear hz1;

%%%%%%%%%%%%%%%% FLAGS %%%%%%%%%%%%%%%%
flags = zeros(imax,jmax,kmax);
nx = flags;
ny = flags;
nz = flags;

% identify and flag location of nanoparticle:
for i=1:imax
    for j=1:jmax
        for k=1:kmax
            if eps(i,j,k) < 5.29
                flags(i,j,k) = 1;
            end
        end
    end
end

% identify boundary types and define normal vectors through
% pixel boundary surfaces:
for i=1:imax
    for j=1:jmax
        for k=1:kmax
            if flags(i,j,k) == 1
                if flags(i-1,j,k) == 0
                    flags(i,j,k)= 2;
                    nx(i,j,k)=1;
                end
                if flags(i+1,j,k) == 0
                    flags(i,j,k) = 3;
                    nx(i,j,k) = -1;
                end
                if flags(i,j-1,k) == 0
                    flags(i,j,k)= 4;
                    ny(i,j,k)=1;
                end
                if flags(i,j+1,k) == 0
                    flags(i,j,k) = 5;
                    ny(i,j,k)=-1;
                end
                if flags(i,j,k-1) == 0
                    flags(i,j,k)= 6;
                    nz(i,j,k) = 1;
                end
                if flags(i,j,k+1) == 0
                    flags(i,j,k) = 7;
                    nz(i,j,k)=-1;
                end
```

```
if flags(i-1,j,k) == 0 && flags(i,j-1,k) == 0
    flags(i,j,k)= 8;
    nx(i,j,k) = 1;
    ny(i,j,k) = 1;
end
if flags(i-1,j,k) == 0 && flags(i,j+1,k)==0
    flags(i,j,k) = 9;
    nx(i,j,k) = 1;
    ny(i,j,k) = -1;
end
if flags(i-1,j,k) == 0 && flags(i,j,k-1) == 0
    flags(i,j,k)= 10;
    nx(i,j,k) = 1;
    nz(i,j,k) = 1;

end
if flags(i-1,j,k) == 0 && flags(i,j,k+1)==0
    flags(i,j,k) = 11;
    nx(i,j,k) = 1;
    nz(i,j,k) = -1;
end
if flags(i+1,j,k) == 0 && flags(i,j-1,k) == 0
    flags(i,j,k)= 12;
    nx(i,j,k) = -1;
    ny(i,j,k) = 1;
end
if flags(i+1,j,k) == 0 && flags(i,j+1,k) == 0
    flags(i,j,k)= 13;
    nx(i,j,k) = -1;
    ny(i,j,k) = -1;
end
if flags(i+1,j,k) == 0 && flags(i,j,k-1) == 0
    flags(i,j,k)= 14;
    nx(i,j,k) = -1;
    nz(i,j,k) = 1;
end
if flags(i+1,j,k) == 0 && flags(i,j,k+1) == 0
    flags(i,j,k)= 15;
    nx(i,j,k) = -1;
    nz(i,j,k) = -1;
end
if flags(i,j,k-1) == 0 && flags(i,j-1,k) == 0
    flags(i,j,k)= 16;
    ny(i,j,k) = 1;
    nz(i,j,k) = 1;
end
if flags(i,j,k-1) == 0 && flags(i,j+1,k) == 0
    flags(i,j,k)= 17;
    ny(i,j,k) = -1;
    nz(i,j,k) = 1;
end
if flags(i,j,k+1) == 0 && flags(i,j-1,k) == 0
    flags(i,j,k)= 18;
    ny(i,j,k) = 1;
    nz(i,j,k) = -1;
end
if flags(i,j,k+1) == 0 && flags(i,j+1,k) == 0
```

```
    flags(i,j,k)= 19;
    ny(i,j,k) = -1;
    nz(i,j,k) = -1;
end
if flags(i-1,j,k) == 0 && flags(i,j-1,k) == 0 ...
  && flags(i,j,k-1) == 0
    flags(i,j,k)= 20;
    nx(i,j,k) = 1;
    ny(i,j,k) = 1;
    nz(i,j,k) = 1;
end
if flags(i-1,j,k) == 0 && flags(i,j+1,k) == 0 ...
  && flags(i,j,k-1) == 0
    flags(i,j,k)= 21;
    nx(i,j,k) = 1;
    ny(i,j,k) = -1;
    nz(i,j,k) = 1;
end
if flags(i+1,j,k) == 0 && flags(i,j-1,k) == 0 ...
  && flags(i,j,k-1) == 0
    flags(i,j,k)= 22;
    nx(i,j,k) = -1;
    ny(i,j,k) = 1;
    nz(i,j,k) = 1;
end
if flags(i+1,j,k) == 0 && flags(i,j+1,k) == 0 ...
  && flags(i,j,k-1) == 0
    flags(i,j,k)= 23;
    nx(i,j,k) = -1;
    ny(i,j,k) = -1;
    nz(i,j,k) = 1;
end
if flags(i-1,j,k) == 0 && flags(i,j-1,k) == 0 ...
  && flags(i,j,k+1) == 0
    flags(i,j,k)= 24;
    nx(i,j,k) = 1;
    ny(i,j,k) = 1;
    nz(i,j,k) = -1;
end
if flags(i-1,j,k) == 0 && flags(i,j+1,k) == 0 ...
  && flags(i,j,k+1) == 0
    flags(i,j,k)= 25;
    nx(i,j,k) = 1;
    ny(i,j,k) = -1;
    nz(i,j,k) = -1;
end
if flags(i+1,j,k) == 0 && flags(i,j-1,k) == 0 ...
  && flags(i,j,k+1) == 0
    flags(i,j,k)= 26;
    nx(i,j,k) = -1;
    ny(i,j,k) = 1;
    nz(i,j,k) = -1;
end
if flags(i+1,j,k) == 0 && flags(i,j+1,k) == 0 ...
  && flags(i,j,k+1) == 0
    flags(i,j,k)= 27;
    nx(i,j,k) = -1;
```

```
                    ny(i,j,k) = -1;
                    nz(i,j,k) = -1;
                end
            end
        end
    end
end
fprintf('done with flags \n')

%%%%%%%%%%%%%%% END FLAGS %%%%%%%%%%%%%%%

% set up Fourier transforms:
Ewx = zeros(imax,jmax,kmax,tmax);    % pre allocate
Ewy = Ewx;
Ewz = Ewx;
Hwx = Ewx;
Hwy = Ewx;
Hwz = Ewx;

for i=1:imax
    for j=1:jmax
        for k=1:kmax
            if flags(i,j,k) > 1
                Ewx(i,j,k,:)=fft(ex(i,j,k,:));  % Fourier transforms
                Ewy(i,j,k,:)=fft(ey(i,j,k,:));  % these are 4D
                Ewz(i,j,k,:)=fft(ez(i,j,k,:));
                Hwx(i,j,k,:)=fft(hx(i,j,k,:));
                Hwy(i,j,k,:)=fft(hy(i,j,k,:));
                Hwz(i,j,k,:)=fft(hz(i,j,k,:));
            end
        end
    end
end
fprintf('done with transforms \n')

nx4= zeros(imax,jmax,kmax,tmax);    %4D normal vector arrays
ny4= zeros(imax,jmax,kmax,tmax);
nz4= zeros(imax,jmax,kmax,tmax);

for i=1:imax
    for j=1:jmax
        for k=1:kmax
            if flags(i,j,k) > 1
                nx4(i,j,k,:)=nx(i,j,k); % make normal vectors 4D
                ny4(i,j,k,:)=ny(i,j,k);
                nz4(i,j,k,:)=nz(i,j,k);
            end
        end
    end
end
fprintf('done with 4D normal vectors \n')

% column vector in the 4th dimimension, indexed by frequency:
SdotN=zeros(1,1,1,tmax);
```

```
for i=1:imax
    for j=1:jmax
        for k=1:kmax
            if flags(i,j,k) > 1 % sum S dot N at all points, at all freqs
               SdotN(1,1,1,:)= SdotN(1,1,1,:) + ...
                   real( dot( [nx4(i,j,k,:),ny4(i,j,k,:),nz4(i,j,k,:)], ...
                    cross([conj(Ewx(i,j,k,:)),conj(Ewy(i,j,k,:)),...
                    conj(Ewz(i,j,k,:))],...
                    [Hwx(i,j,k,:),Hwy(i,j,k,:),Hwz(i,j,k,:)]) ) );
            end
        end
    end
end

SdotNw = zeros(1,tmax);

for t=1:tmax
    SdotNw(t) = SdotN(1,1,1,t);  %turn into well behaved vector
end

SdotNw % this is the absorption by the particle as a function of frequency

%%%%%%%%%%%%%%%%%%%%%%%%%%%%%%%%%%%%%%%%%%%%%%%%%%%%%%%%%%%%%%%%%%%%%%%%%%%%

% load in planar field data:
ex_in1 = hd5open('ex_in.h5');
ey_in1 = hd5open('ey_in.h5');
ez_in1 = hd5open('ez_in.h5');
hx_in1 = hd5open('hx_in.h5');
hy_in1 = hd5open('hy_in.h5');
hz_in1 = hd5open('hz_in.h5');
[tmax, jmax, imax]= size(ex_in1);

ex_in = zeros(imax,jmax,tmax);  %preallocate
ey_in = ex_in;
ez_in = ex_in;
hx_in = ex_in;
hy_in = ex_in;
hz_in = ex_in;

for t=1:tmax
    for i=1:imax
        for j=1:jmax
                % redefine arrays so x=i, y=j, time = t
                ex_in(i,j,t) = ex_in1(t,j,i);
                ey_in(i,j,t) = ey_in1(t,j,i);
                ez_in(i,j,t) = ez_in1(t,j,i);
                hx_in(i,j,t) = hx_in1(t,j,i);
                hy_in(i,j,t) = hy_in1(t,j,i);
                hz_in(i,j,t) = hz_in1(t,j,i);
        end
    end
end

clear ex_in1;
```

```
clear ey_in1;
clear ez_in1;
clear hx_in1;
clear hy_in1;
clear hz_in1;

Ewx_in = zeros(imax,jmax,tmax);   % pre allocate
Ewy_in = Ewx_in;
Ewz_in = Ewx_in;
Hwx_in = Ewx_in;
Hwy_in = Ewx_in;
Hwz_in = Ewx_in;

for i=1:imax
    for j=1:jmax
                Ewx_in(i,j,:)=fft(ex_in(i,j,:));  %fourier transforms
                Ewy_in(i,j,:)=fft(ey_in(i,j,:));  % these are 3D
                Ewz_in(i,j,:)=fft(ez_in(i,j,:));
                Hwx_in(i,j,:)=fft(hx_in(i,j,:));
                Hwy_in(i,j,:)=fft(hy_in(i,j,:));
                Hwz_in(i,j,:)=fft(hz_in(i,j,:));
    end
end
fprintf('done with transforms \n')

% column vector in the 3rd dim, indexed by frequency
SdotN_in=zeros(1,1,tmax);

xcomp = SdotN_in; % components of the normal vector = (0,0,1) at all times
ycomp = xcomp;
zcomp = ones(1,1,tmax);

for i=1:imax
    for j=1:jmax
        SdotN_in(1,1,:)= SdotN_in(1,1,:) ...
            + real( dot( [xcomp ycomp zcomp], ...
            cross([conj(Ewx_in(i,j,:)),conj(Ewy_in(i,j,:)),...
            conj(Ewz_in(i,j,:))], ...
            [Hwx_in(i,j,:),Hwy_in(i,j,:),Hwz_in(i,j,:)]) ) );
    end
end

SdotNw_in=zeros(1,tmax);
for t=1:tmax
    SdotNw_in(t) = SdotN_in(1,1,t);  %turn into well behaved vector
end

SdotNw_in



ex_out1 = hd5open('ex_out.h5');
ey_out1 = hd5open('ey_out.h5');
ez_out1 = hd5open('ez_out.h5');
hx_out1 = hd5open('hx_out.h5');
```

```
hy_out1 = hd5open('hy_out.h5');
hz_out1 = hd5open('hz_out.h5');
[tmax, jmax, imax]= size(ex_out1);

ex_out = zeros(imax,jmax,tmax);  %preallocate
ey_out = ex_out;
ez_out = ex_out;
hx_out = ex_out;
hy_out = ex_out;
hz_out = ex_out;

for t=1:tmax
    for i=1:imax
        for j=1:jmax
                %redefine arrays so x=i, y=j, time = t
                ex_out(i,j,t) = ex_out1(t,j,i);
                ey_out(i,j,t) = ey_out1(t,j,i);
                ez_out(i,j,t) = ez_out1(t,j,i);
                hx_out(i,j,t) = hx_out1(t,j,i);
                hy_out(i,j,t) = hy_out1(t,j,i);
                hz_out(i,j,t) = hz_out1(t,j,i);
        end
    end
end

clear ex_out1;
clear ey_out1;
clear ez_out1;
clear hx_out1;
clear hy_out1;
clear hz_out1;

Ewx_out = zeros(imax,jmax,tmax);    % pre allocate
Ewy_out = Ewx_out;
Ewz_out = Ewx_out;
Hwx_out = Ewx_out;
Hwy_out = Ewx_out;
Hwz_out = Ewx_out;

for i=1:imax
    for j=1:jmax
                Ewx_out(i,j,:)=fft(ex_out(i,j,:));  %fourier transforms
                Ewy_out(i,j,:)=fft(ey_out(i,j,:));  % these are 3D
                Ewz_out(i,j,:)=fft(ez_out(i,j,:));
                Hwx_out(i,j,:)=fft(hx_out(i,j,:));
                Hwy_out(i,j,:)=fft(hy_out(i,j,:));
                Hwz_out(i,j,:)=fft(hz_out(i,j,:));
    end
end
fprintf('done with transforms \n')

% column vector in the 3rd dim, indexed by frequency
SdotN_out=zeros(1,1,tmax);

xcomp = SdotN_out; % components of the normal vector = (0,0,1) at all times
```

```
ycomp = xcomp;
zcomp = ones(1,1,tmax);

for i=1:imax
    for j=1:jmax
        SdotN_out(1,1,:)= SdotN_out(1,1,:) ...
            + real( dot( [xcomp ycomp zcomp], ...
            cross([conj(Ewx_out(i,j,:)),conj(Ewy_out(i,j,:)),...
            conj(Ewz_out(i,j,:))], ...
            [Hwx_out(i,j,:),Hwy_out(i,j,:),Hwz_out(i,j,:)]) ) );
    end
end

SdotNw_out=zeros(1,tmax);
for t=1:tmax
    SdotNw_out(t) = SdotN_out(1,1,t);  %turn into well behaved vector
end

SdotNw_out


% net power values from analysis:
IN = SdotNw_in;
LOSS = SdotNw;
OUT = SdotNw_out;
```

APPENDIX C

FDTD Simulation of Absorption in Textured Amorphous Silicon Layer with Metal Nanoparticles

In Chapter 2, we introduced a novel method for analyzing broad spectrum absorption properties via FDTD simulation. As a final demonstration of the analysis method (and for the sake of completeness), we consider here a situation that is more complex than the case discussed in Chapter 2 in two respects: First, the nanostructured solar cell geometry is more complicated. This presents little difficulty, as our analysis is designed around the ability to treat arbitrary geometries. Second, the absorption properties of the PV material are no longer set to be constant across frequency. In this case, we consider an active region of amorphous silicon (a-Si), using tabulated dielectric constant data[50]. This material presents a challenge, as the Lorentz-Drude model of dispersion that is typically implemented in FDTD simulations tends to provide a poor fit for band-tail absorption in semiconductors[134]. We address this by creating two independent Lorentz models for the dielectric constant data – one that is valid below 612 nm (above 2 eV), and one that is valid in the band tail states above 612 nm (below 2 eV), as shown in Figure C.1(a). Two separate simulations are run using the different models to generate the corresponding segments of the absorption spectrum. While we must compromise on the broad band nature of the analysis to maintain accuracy, we do not need to resort to running a large number of single frequency simulations.

A nanostructured solar cell region is simulated, containing a 40 nm metal sphere placed on an Alumina (Al_2O_3) substrate and encapsulated by a 25 nm a-Si absorbing region. This region is capped by a conformal 50 nm Indium Tin Oxide (ITO) transparent electrode, as shown in the inset of Figure C.1(b). The a-Si and metal absorption spectra for this geometry are shown in Figure C.1(b), considering both silver (Ag) and aluminum (Al) particles, with the LSP resonance of the silver particle leading to improved a-Si absorption at 840 nm in the band-tail region, similar to demonstrations in the literature[22].

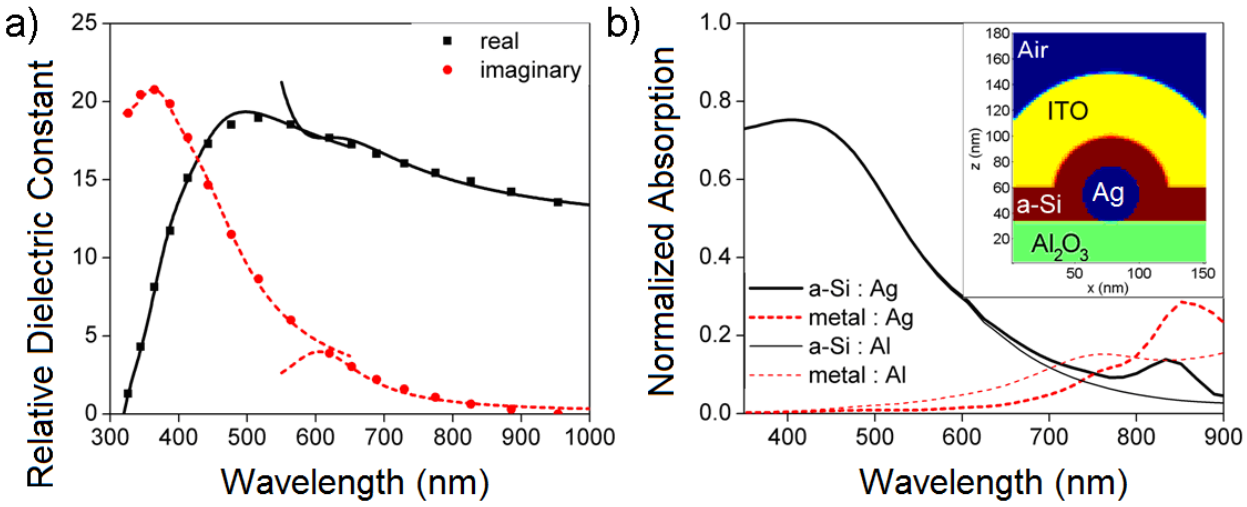

Figure C.1 (a) Tabulated values (points)[50] and Lorentz-Drude models (lines) for the complex dielectric constant of amorphous silicon. Note separate models are used above and below 612 nm. (b) Broad spectrum absorption properties for the inset geometry, with either silver or aluminum (off resonance) nanoparticles.

BIBLIOGRAPHY

[1] A. Goetzberger, C. Hebling, "Photovoltaic materials, past, present, future," Solar Energy Materials and Solar Cells **62**, 1 (2000).

[2] T.M. Razykov, C. S. Ferekides, D. Morel, E. Stefanakos, H.S. Ullal, H.M. Upadhyaya, "Solar photovoltaic electricity: current status and future prospects," Solar Energy **85**, 1580 (2011).

[3] A. Shah, P. Torres, R. Tscharner, N. Wyrsch, H. Keppner, "Photovoltaic technology: the case for thin-film solar cells," Science **30**, 692 (1999).

[4] M. A. Green, "Thin-film solar cells: review of materials, technologies and commercial status," Journal of Materials in Science: Materials in Electronics **18**, 15 (2007).

[5] K. L. Chopra, P. D. Paulson, V. Dutta, "Thin-film solar cells: an overview," Progress in Photovoltaics: Research and Applications **12**, 69 (2004).

[6] B. O'Regan, M. Grätzel, "A low-cost, high-efficiency solar cell based on dye-sensitized colloidal TiO_2 films," Nature **353**, 737 (1991).

[7] H. Hoppe, N. S. Sariciftci, "Organic solar cells: an overview," Journal of Materials Reserach **19**, 1924 (2004).

[8] P. Peumans, A.Yakimov, S. R. Forrest, "Small molecular weight organic thin-film photodetectors and solar cells," Journal of Applied Physics **93**, 3692 (2003).

[9] A. Pivrikas, N. S. Sariciftci, G. Juska, R. Osterbacka, "A review of charge transport and recombination in polymer/fullerene organic solar cells," Progress in Photovoltaics: Research and Applications **15**, 677 (2007).

[10] S. R. Forrest, "The limits to organic photovoltaic cell efficiency," Materials Research Society Bulletin **30**, 28 (2005).

[11] S. A. Maier, *Plasmonics: Fundamentals and Applications*, Springer, New York (2007).

[12] C. F. Bohren, D. R. Huffman, *Absorption and Scattering of Light by Small Particles*, Wiley, New York (1983).

[13] S. A. Maier, H. A. Atwater, "Plasmonics: localization and guiding of electromagnetic energy in metal/dielectric structures," Journal of Applied Physics **98**, 011101 (2005).

[14] J. Z. Zhang, C. Noguez, "Plasmonic optical properties and applications of metal nanostructures," Plasmonics **3**, 127 (2008).

[15] H. A. Atwater, A. Polman, "Plasmonics for improved photovoltaic devices," Nature Materials **9**, 205 (2010).

[16] S. Fahr, C. Rockstuhl, F. Lederer, "Metallic nanoparticles as intermediate reflectors in tandem solar cells," Applied Physics Letters **95**, 121105 (2009).

[17] D. Duche, P. Torchio L. Escoubas, F. Monestier, J.-J. Simon, F. Flory, and G. Mathian, "Improving light absorption in organic solar cells by plasmonic contribution", Solar Energy Materials and Solar Cells **93**, 1377 (2009).

[18] J. Wang, F. Tsai, J. Huang, C. Chen, N. Li, Y. Kiang, and C.C. Yang, "Enhancing InGaN-based solar cell efficiency through localized surface plasmon interaction by embedding Ag nanoparticles in the absorbing layer," Optics Express **18**, 2682 (2010).

[19] A. J. Morfa, K. L. Rowlen, T. H. Reilly, M. J. Romero, J. Van de Lagemaat, "Plasmon-enhanced solar energy conversion in organic bulk heterojunction photovoltaics," Applied Physics Letters **92**, 013504 (2008).

[20] S. H. Lim, W. Mar, P. Matheu, D. Derkacs, E.T. Yu, "Photocurrent spectroscopy of optical absorption enhancement in silicon photodiodes via scattering from surface plasmon polaritons in gold nanoparticles," Journal of Applied Physics **101**, 104309 (2007).

[21] R. A. Pala, J. White, E. Barnard, J. Liu, M. L. Brongersma, "Design of plasmonic thin-film solar cells with broadband absorption enhancements," Advanced Materials **21**, 3504 (2009).

[22] V. E. Ferry, M. A. Verschuuren, H. B. T. Li, R. E. I. Schropp, H. A. Atwater, A. Polman, "Improved red-response in thin film a-Si:H solar cells with soft-imprinted plasmonic back reflectors," Applied Physics Letters **95**, 183503 (2009).

[23] F. J. Beck, A. Polman, K. R. Catchpole, "Tunable light trapping for solar cells using localized surface plasmons," Journal of Applied Physics **105**, 114310 (2009).

[24] K. R. Catchpole, A. Polman, "Design principles for particle plasmon enhanced solar cells," Applied Physics Letters **93**, 191113 (2008).

[25] M.-G. Kang, T. Xu, H. J. Park , X. Luo, L. J. Guo, "Efficiency enhancement of organic solar cells using transparent plasmonic ag nanowire electrodes," Advanced Materials **22**, 4378 (2010).

[26] J. N. Munday, H. A. Atwater, "Large integrated absorption enhancement in plasmonic solar cells by combining metallic gratings and antireflection coatings," Nano Letters **11**, 2011.

[27] D. Derkacs, S. H. Lim, P. Matheu, W. Mar, and E. T. Yu, "Improved performance of amorphous silicon solar cells via scattering from surface plasmon polaritons in nearby metallic nanoparticles," Applied Physics Letters **89**, 093103 (2006).

[28] J. Benemann, O. Chehab and E. Schaar-Gabriel, "Building-integrated PV modules," Solar Energy Materials and Solar Cells **67**, 345 (2001).

[29] G. Quesada, D. Rousse, Y. Dutil, M. Badache, S. Hallé, "A comprehensive review of solar facades. Transparent and translucent solar facades," Renewable and Sustainable Energy Reviews 16, 2643 (2012).

[30] R. R. Lunt and V. Bulovic, "Transparent, near-infrared organic photovoltaic solar cells for window and energy-scavenging applications," Applied Physics Letters **98**, 113305 (2011).

[31] Y. Zhao, G. A. Meek, B.G. Levine, R. R. Lunt, "Near-infrared harvesting transparent luminescent solar concentrators," Advanced Optical Materials **2**, 606 (2014).

[32] D. H. W. Li, T.N.T. Lam, W. W. H. Chan and A. H. L. Mak, "Energy and cost analysis of semi-transparent photovoltaic in office buildings", Applied Energy **86**, 722 (2009).

[33] R. F. Bailey-Salzman, B. P. Rand, and S. R. Forrest, "Semitransparent organic photovoltaic cells," Applied Physics Letters **88**, 233502 (2006).

[34] C.-C. Chueh, S.-C. Chien, H.-L. Yip, J. F. Salinas, C.-Z. Li, K.-S.Chen, F.-C. Chen, W.-C. Chen A. K.-Y. Jen, "Toward high-performance semi-transparent polymer solar cells: optimization of ultra-thin light absorbing layer and transparent cathode architecture," Advanced Energy Materials **3**, 417 (2013).

[35] J. Y. Lee, K.-T. Lee, S. Seo, L. J. Guo, "Decorative power generating panels creating angle insensitive transmissive colors," Nature Scientific Reports **4**, 4192 (2014).

[36] M. Yamaguchi, T. Takamoto, K. Araki, N. Ekins-Daukes, "Multi-junction III-V solar cells: current status and future potential," Solar Energy **79**, 78 (2005).

[37] M. A. Green, "Third generation photovoltaics: ultra-high conversion efficiency at low cost," Progress in Photovoltaics **9**, 123 (2001).

[38] M. K. Siddiki, J. Li, D. Galipeau, Q. Qiao, "A review of polymer multijunction cells," Energy and Environmental Science **7**, 867 (2010).

[39] B. Roberts, D. M. N. M. Dissanayake, P.-C. Ku "Angular selective semi-transparent photovoltaics," Optics Express **20**, A265 (2012).

[40] B. Roberts, M. Boyd, P.-C. Ku, "Optical design of selectively scattering nanostructures for angle sensitive semi-transparent photovoltaics," 38th IEEE Photovoltaics Specialists Conference (PVSC), 000087 (2012).

[41] D. M. N. M. Dissanayake, B. Roberts, P.-C. Ku, "Angular selective backreflector for semitransparent photovoltaics," Applied Physics Letters **101**, 063302 (2012).

[42] B. Roberts, Q. Chen, P.-C. Ku, "Optical scattering by anodized aluminum oxide for light management in thin film photovoltaics," Proceedings of SPIE **8981**, Physics, Simulation, and Photonic Engineering of Photovoltaic Devices III, 89811F (2014).

[43] J.Marchwiński, "Architectural evaluation of switchable glazing technologies as sun protection measure," Energy Procedia **57**, 1677 (2014).

[44] M. Casini, "Smart windows for energy efficiency of buildings," Proceedings of the Second International Conference on Advances in Civil, Structural, and Enviro nmental Engineering, 273 (2014).

[45] V. Viereck, Q. Li, A. Jäkel, H. Hillmer, "Large-area applications of optical MEMS: micromirror arrays guide daylight, optimize indoor illumination," Photonik International **2**, 48 (2009).

[46] R. J. Mortimer, "Electrochromic materials," Chemical Society Reviews **26**, 147 (1997).

[47] J. Livage, D. Ganguli, "Sol-gel electrochromic coatings and devices: a review," Solar Energy Materials and Solar Cells **68**, 365 (2001).

[48] J. D. Jackson, *Classical Electrodynamics,* Wiley, New York, (1999).

[49] P. B. Johnson, R. W. Christy, "Optical constants of the noble metals," Physical Review B **6**, 4370 (1972).

[50] E. D. Palik, *Handbook of Optical Constants of Solids*, Academic Press, New York (1991).

[51] A. D. Rakic, A. B. Djurišic, J. M. Elazar, M. L. Majewski, "Optical properties of metallic films for vertical-cavity optoelectronic devices," Applied Optics **37**, 5271 (1998).

[52] M. W. Knight, N. S. King, L.Liu, H. O. Everitt, P. Nordlander, N. J. Halas, "Aluminum for plasmonics," ACS Nano **8**, 834 (2014)

[53] A. Moscatelli, "Plasmonics: the aluminum rush," Nature Nanotechnology **7**, 778 (2012).

[54] A. E. Siegman, *Lasers*, University Science Books, Sausalito, CA (1986).

[55] S. L. Chuang, *Physics of Photonic Devices (2nd ed.)*, Wiley, Hoboken, NJ (2009).

[56] G. Mie, "Beiträge zur optik trüber medien, speziell kolloidaler metallösungen". Annalen der Physik **330**, 377 (1908).

[57] J. A. Stratton, *Electromagnetic Theory*, McGraw-Hill, New York (1941).

[58] A. Taflove, S. C. Hagness, *Computational Electrodynamics: The Finite-Difference Time-Domain Method*, Artech, Norwood, MA (2000).

[59] B. Roberts, P.-C. Ku, "Broadband characteristics of surface plasmon enhanced solar cells," 35th IEEE Photovoltaics Specialists Conference (PVSC), 002952 (2010).

[60] A. F. Oskooi, D. Roundy, M. Ibanescu, P. Bermel, J. D. Joannopoulos, and S. G. Johnson, "MEEP: a flexible free-software package for electromagnetic simulations by the FDTD method," Computer

[61] D. M. N. M. Dissanayake, B. Roberts, P.-C. Ku, "Plasmonic backscattering enhanced inverted photovoltaics," Applied Physics Letters **99**, 113306 (2011).

[62] P. Colson, C. Henrist, R. Cloots, "Nanosphere lithography, a powerful method for the controlled manufacturing of nanomaterials," Journal of Nanomaterials **2013**, 948510 (2013).

[63] J. C. Hulteen, D. A. Treichel, M. T. Smith, M. L. Duval, T. R. Jensen, R. P. Van Duyne, "Nanosphere lithography: size-tunable silver nanoparticle and surface cluster arrays" Journal of Physical Chemistry B **103**, 3854 (1999).

[64] T.R. Jensen, G. C. Schatz, R. P. Van Duyne, "Nanosphere lithography: surface plasmon resonance spectrum of a periodic array of silver nanoparticles by ultraviolet-visible extinction spectroscopy and electrodynamic modeling," Journal of Physical Chemistry B **103**, 2394 (1999).

[65] T.R. Jensen, M. L. Duval, K. L. Kelly, A. A. Lazarides, G. C. Schatz, R. P. Van Duyne, "Nanosphere lithography: effect of the external dielectric medium on the surface plasmon resonance spectrum of a periodic array of silver nanoparticles," Journal of Physical Chemistry B **103**, 9846 (1999).

[66] C. Chou, W. Kwan, Z. Hong, L. Chen, Y. Yang, "A metal-oxide interconnection layer for polymer tandem solar cells with an inverted architecture," Advanced Materials **23**, 1282 (2011).

[67] W. Shockley, H. J. Queisser, "Detailed balance limit of efficiency of p-n junction solar cells," Journal of Applied Physics **32**, 510 (1961).

[68] G. F. Burkhard, E. T. Hoke, M. McGehee, "Accounting for interference, scattering, and electrode absorption to make accurate internal quantum efficiency measurements in organic and other thin solar cells," Advanced Materials **22**, 3293 (2010).

[69] J. Hong, W. Huang, T. Makino, "On the transfer matrix method for distributed-feedback waveguide devices," Journal of Lightwave Technology **10**, 1860 (1992)

[70] L. A. Pettersson, L. S. Roman, O. Inganas, "Modeling photocurrent action spectra of photovoltaic devices based on organic thin films," Journal of Applied Physics **86**, 487 (1999).

[71] M. Young, C. J. Traverse, R. Pandey, M. C. Barr, R. R. Lunt, "Angle dependence of transparent photovoltaics in conventional and optically inverted configurations," Applied Physics Letters **103**, 133304 (2013).

[72] A. Yariv, P. Yeh, *Optical Waves in Crystals: Propagation and Control of Laser Radiation*, Wiley, Hoboken, NJ (1984).

[73] J. D. Joannopoulos, S. G. Johnson, J. N. Winn, R. D. Meade, *Photonic Crystals: Molding the Flow of Light (2nd ed.)*, Princeton University Press, Princeton, NJ (2008).

[74] R. Walraven "Calculating the position of the sun," Solar Energy **20**, 393 (1978).

[75] J. Venermo, A. Sihvola, "Dielectric polarizability of circular cylinder," Journal of Electrostatics **63**, 101 (2005).

[76] COMSOL Multiphysics® Version 4.2 (2011). COMSOL, Inc., Burlington, MA, USA.

[77] S. Yushanov, J. S. Crompton, K. C. Koppenhofer, "Mie scattering of electromagnetic waves," Proceedings of the 2013 COMSOL Conference (2013).

[78] C. Elachi "Waves in active and passive periodic structures: a review," Proceedings of the IEEE **64**, 1666 (1976).

[79] R. L. Field, "Solar energy window," United States of America as represented by the Secretary of the Navy, assignee, US Patent 4137098 A (1977).

[80] C. W. Gillard, "Solar cell window fitting," Lockheed Missiles & Space Company Inc, assignee, US Patent 5221363 (1993).

[81] C. M. Andres, J. Zhu, T. Shyu, C. Flynn, N. A. Kotov "Shape morphing nanocomposite origami," Langmuir **30**, 5378 (2014).

[82] Y. Liu, J. Park, R. J. Lang, A. Emami-Neyestanak, S. Pellegrino, M. S. Humayun, Y.-C. Tai, "Paraylyne origami structure for introcular implantation," Transducers & Eurosensors XXVII, 1549 (2013).

[83] A. Vorob'ev, P.Vaccaro, K. Kubota, S. Saravanan, T. Aida, "Array of micromachined components fabricated using "micro-origami" method," Japanese Journal of Applied Physics **42**, 4024.

[84] G. T. Pickett, "Self-folding origami membranes," Europhysics Letters **78**, 48003 (2007).

[85] C. Yu, H. Jiang, "Forming wrinkled stiff films on polymeric substrates at room temperature for stretchable interconnects applications," Thin Solid Films **519**, 818 (2010).

[86] K. Weiu, Y. Zhao, "Fast and versitile fabrication of PDMS nanowrinkling structures," 16th International Conference on Miniaturized Systems for Chemisty and Life Sciences, 665 (2012).

[87] C. Hanske, M. Tebbe, C. Kuttner, V. Bieber, V. V. Tsukruk, M. Chanana, T. A. F. König, A. Fery, "Strongly coupled plasmonic modes on macroscopic areas via template-assisted colloidal self-assembly," Nano Letters **14**, 6863 (2014).

[88] T. Shyu and N. A. Kotov, Department of Chemical Engineering, University of Michigan, unpublished work (2015).

[89] X. Huang, S. Neretina, M. A. El-Sayed, "Gold nanorods: from synthesis and properties to biological and biomedical applications," Advanced Materials **21**, 4880 (2009).

[90] A. Gole, C. J. Murphy, "Seed-mediated synthesis of gold nanorods: role of the size and nature of the seed," Chemistry of Materials **16**, 3633 (2004).

[91] J. He, Y. Wang, Y. Feng, X. Qi, Z. Zheng, Q. Liu, W. S. Teo, C. L. Gan, H. Zhang, H. Chen, "Forest of gold nanowires: a new type of nanocrystal growth," ACS Nano **7**, 2733 (2013).

[92] A. M. Österholm, D. E. Shen, J. A. Kerszulis, R. H. Bulloch, M. Kuepfert, A. L. Dyer, J. R. Reynolds, "Four shades of brown: tuning of electrochromic polymer blends toward high-contrast eyewear," ACS Applied Materials and Interfaces **7**, 1413 (2015).

[93] B. Smits, "An RGB to spectrum conversion for reflectances," Journal of Graphics Tools **4**, 11 (1999).

[94] N. S. King, Y. Li, C. Ayala-Orozco, T. Brannan, P. Nordlander, N. J. Halas, "angle- and spectral-dependent light scattering from plasmonic nanocups," ACS Nano **5**, 7254 (2011).

[95] B. Lamprecht, G. Schider, R. T. Lechner, H. Ditlbacher, J. R. Krenn, A. Leitner, F. R. Aussenegg, "Metal nanoparticle gratings: influence of dipolar particle interaction on plasmon resonance," Physical Review Letters **84**, 4721 (2000).

[96] A. M. Md Jani, D. Losic, N. H. Voelcker, "Nanoporous anodic aluminum oxide: advances in surface engineering and emerging applications," Progress in Materials Science **58**, 636 (2013)

[97] G. E. J. Poinern, N. Ali, D. Fawcett, "Progress in nano-engineered anodic aluminum oxide membrane development," Materials **2011**, 487 (2011).

[98] A. Belwalkar, E. Grasing, W. Van Geertruyden, Z. Huang, W. Z. Misiolek, "Effect of processing parameters on pore structure and thickness of anodic aluminum oxide (AAO) tubular membranes," Journal of Membrane Science **319**, 192 (2008).

[99] S. Ono, M. Saito, H. Asoh, "Self-ordering of anodic porous alumina formed in organic acid electrolytes," Electrochimica Acta **51**, 827 (2005).

[100] A. L. Friedman, D. Brittain, L .Menon, "Roles of pH and acid type in the anodic growth of porous alumina," Journal of Chemical Physics **127**, 154717 (2007).

[101] H. Masuda, K. Fukuda, "Ordered metal nanohole arrays made by a two-step replication of honeycomb structures of anodic alumina," Science **268**, 1466 (1995).

[102] F. Li, L. Zhang, R. M. Metzger, "On the growth of highly ordered pores in anodized aluminum oxide," Chemistry of Materials **10**, 2470 (1998)

[103] C. Y. Han, G. A. Willing, Z. Xiao, H. H. Wang, "Control of the anodic aluminum oxide barrier layer opening process by wet chemical etching," Langmuir **23**, 1564 (2003).

[104] K. P. Musselman, G. J. Mulholland, A. P. Robinson, L. Schmidt-Mende, J. L. MacManus-Driscoll, "Low-temperature synthesis of large-area, free-standing nanorod arrays on ITO/glass and other conducting substrates," Advanced Materials **20**, 4470 (2008).

[105] J. Oh, C. V. Thompson, "Selective barrier perforation in porous alumina anodized on substrates" Advanced Materials **20**, 1368 (2008).

[106] J. Oh, Y. C. Shin, C. V. Thompson, "A tungsten interlayer process for fabrication of through-pore AAO scaffolds on gold substrates," Journal of the Electrochemical Society **158**, K11 (2011).

[107] Kornelius Nielsch, Jinsub Choi, Kathrin Schwirn, Ralf B. Wehrspohn, Ulrich Gösele, "Self-ordering regimes of porous alumina: the 10% porisity rule," Nano Letters **2**, 677 (2002).

[108] W. Na, Z. Wen-Di, X. Ji-Peng, M. Bin, Z. Zong-Zhi, J. Qing-Yuan, E. Bunte, J. Hüpkes, H. P. Bochem, "Fabrication of anodic aluminum oxide templates with small interpore distances," Chinese Physics Letters **27**, 066801 (2010).

[109] K. M. Alam, A. P. Singh, S. C. Bodepudi, S. Pramanik, "Fabrication of hexagonally ordered nanopores in anodic alumina: an alternative pretreatment," Surface Science **605**, 441 (2011).

[110] W. Chen, J.S. Wu, X.-H. Xia, "Porous anodic alumina with continuously manipulated pore/cell size," ACS Nano **2**, 959 (2008)

[111] C. Sun, J. Luo, L. Wu, J. Zhang, "Self-ordered anodic alumina with continuously tunable pore intervals from 410 to 530 nm," Applied Materials and Interfaces **2**, 1299 (2010).

[112] J. Martin, C. V. Manzano, M. Martin-González, "In-depth study of self-ordered porous alumina in the 140-400 nm pore diameter range," Microporous and Mesoporous Materials **151**, 311 (2012).

[113] Y. Li, M. Zheng, L. Ma, W. Shen, "Fabrication of highly ordered nanoporous alumina films by stable high-field anodization," Nanotechnology **17**, 5101 (2006).

[114] L. Yi, L. Zhiyuan, C. Shuoshu, H. Xing, H. Xinhua, "Novel AAO films and hollow nanostructures fabricated by ultra-high voltage hard anodization," Chemical Communications **46**, 309 (2010).

[115] C.-J. Yang, S.-W. Liang, P.-W. Wu, C. Chen, J.-M. Shieh, "Fabrication of anodic aluminum oxide film on large-area glass substrate," Electrochemical and Solid State Letters **10**, C69 (2007).

[116] R. T. Foley, "Localized corrosion of aluminum alloys - a review," Corrosion **42**, 277 (1986).

[117] M. Pourbaix, *Atlas of Electrochemical Equilibria in Aqueous Solutions (2nd ed.)*, National Association of Corrosion Engineers, Houston, TX (1974).

[118] M. B. Pomfret, D. J. Brown, A. Epshteyn, A. P. Purdy, J. C. Owrutsky, "Electrochemical template deposition of aluminum nanorods using ionic liquids," Chemistry of Materials **20**, 5945 (2008).

[119] V. M. Donnelly, A. Kornblit, "Plasma etching: yesterday, today, and tomorrow," Journal of Vacuum Science Technology A **31**, 050825 (2013).

[120] J. W. Lutze, A. H. Perera, J. P. Krusius, "Anisotropic reactive ion etching of aluminum using Cl_2, BCl_3, and CH_4 gases," Journal of the Electrochemical Society **137**, 249 (1990).

[121] V. Gruev, "Fabrication of a dual-layer aluminum nanowires polarization filter array," Optics Express **19**, 24361 (2011).

[122] S. Gao, R. Njuguna, V. Gruev, "Fabrication and evaluation of pixelated nano-wire grid polarizer," Proceedings of SPIE Vol. **8873**, Polarization Science and Remote Sensing VI, 88730L (2013).

[123] R. M. Ranade, S. S. Ang, W. D. Brown, "Reactive ion etching of thin gold films," Journal of the Electrochemical Society **140**, 3676 (1993).

[124] F. T. Aldridge, "High speed anisotropic reactive ion etching of gold films," Journal of the Electrochemical Society **142**, 1563 (1995).

[125] P. Nguyen., Y. Zeng, T. L. Alford, "Reactive ion etch of patterned and blanked silver thin films in Cl_2 / O_2 and O_2 glow discharges," Journal of Vacuum Science and Technology B **17**, 2204 (1999).

[126] K. R. Williams, K. Gupta, M. Wasilik, "Etch rates for micromachining processing - part II," Journal of Microelectromechanical Systems **12**, 761 (2003).

[127] G. Gomard, O. El Daif, E. Drouard , X. Meng, A. Kaminski , A. Fave, M. Lemiti , E. Garcia-Caurel , P. R. Cabarrocas , C. Seassal, "Design and fabrication of photonic crystal thin film photovoltaic cells," Proceedings of SPIE **7725**, Photonics for Solar Energy Systems III, 77250M (2010)

[128] G. Gomard, R. Peretti, E. Drouard, X. Meng, C. Seassal, "Photonic crystals and optical mode engineering for thin film photovoltaics," Optics Express **21**, A515 (2013).

[129] J. R. Wait, "Scattering of a plane wave from a circular dielectric cylinder at obique incidence," Canadian Journal of Physics **33**, 189 (1955).

[130] B. H. Henin, A. Z. Elsherbeni, and M. A. Sharkawy, "Oblique incidence plane wave scattering from an array of circular cylinders," Progress in Electromagnetics Research **68**, 261 (2007).

[131] T. P. Woodman, "Light scattering in porous anodic aluminium oxide films: I. Colour effects," Thin Solid Films **9**, 195 (1972).

[132] T. P. Woodman, "Light scattering in porous anodic aluminium oxide films: II. Polarization effects," Thin Solid Films **9**, 389 (1972).

[133] K. Huang, Y. Li, Z. Wu, C. Li, H. Lai, and J. Kang, "Asymmetric light reflectance effect in AAO on glass," Optics Express **19**, 1301 (2011).

[134] H. G. Tompkins, E. A. Irene, *Handbook of Ellipsometry*, William Andrew, Norwich NY (2005).